Improving Position Estimation in Double-Sided Strip (DSS) High-Purity Germanium HPGe Detectors for Gamma-ray Imaging

By

Rose Schmitt Perea

Dissertation
Submitted to the Faculty of the
Graduate School of Vanderbilt University
in partial fulfillment of the requirements
for the degree of

DOCTOR OF PHILOSOPHY
in
Physics

September 30, 2019

Nashville, Tennessee

Approved:
Todd E. Peterson, Ph.D.

Keivan G. Stassun, Ph.D.

Arnold Burger, Ph.D.

Tomas Yankeelov, Ph.D.

DEDICATION

This dissertation is dedicated to my husband,
who has suffered all of our married years so
far with me in graduate school. You have been
my rock and biggest pillar of support.
I love you.

My Dad and step-mom Lydia for
always being proud of me and believing in me.

And lastly, to my Uncle Joe, I
know you would be proud. We miss you.

ACKNOWLEDGEMENT

First I would like to thank my advisor, Dr. Todd E. Peterson. For your patience, wisdom, and kindness. You have allowed me to make mistakes and helped me grow from them. Most of all, I know I can always reach out to you for advice and support. I will miss ”making your head hurt” on Friday afternoons and hearing your bad dad jokes.

To my committee who helped me in all the stages of this journey, from my qualifier, to trouble-shooting my code and especially on this last push to make sure I was done and out the door. Dr. Kevian G. Stassun, Dr. Kelly Holley-Bockelmann, Dr. Arnold Burger, and Dr. Thomas Yankeelov, to each one of you, thank you.

A special thanks to Dr. Lars Furenlid and Dr. Adam Anderson for spending extra time with me to look over my data and to de-bug my code.

To the lab group who spent their time listening to my practice talks, helping me with lab work, and offering their insights and criticisms: Desmond Campbell, Dr. Noor Tantawy, and Dr. Sepi Shokouhi. Thank you.

I could not have made it this far if it wasn’t for the Fisk-Vanderbilt Masters-to-PhD Bridge program. This program was a second family to me and was literally always behind my back supporting me. Specifically Dr. Dina Stroud, Alyce Dobyns, and Dr. Lauren Pallandino-Campbell.

I am also grateful to have had various funding sources for this research: NIH/NIBIB R01 EB13677, R44 EB15889, 5T32EB014841, and F31 EB022422-02.

TABLE OF CONTENTS

Page

LIST OF TABLES

Table Page

LIST OF FIGURES

Chapter 1

Introduction

Imaging in biomedical and astrophysics fields may seem vastly different, but, when imaging gamma-ray sources, many aspects are similar. Both require imaging systems with high energy resolution, both must constrain the angles of acceptance from the radiative source (this may be done with collimators in medical imaging and with coded apertures in astrophysics, for example), and both require choice of an image reconstruction algorithm that results in an image with high spatial resolution and contrast [1].

In this dissertation, I will discuss my work on improving the event positioning in a high-purity germanium (HPGe) detector, currently used for gamma-ray imaging in a biomedical application, and discuss how my findings are applicable to similar detectors in both the biomedical and astrophysics fields. The order of this dissertation is as follows: types of radiation decay that lead to the production of gamma-rays, astrophysical sources and biomedical applications, and a discussion on two of the more common types of gamma-ray detectors: scintillators and semiconductors (and how to choose between them). I then describe our particular detector, how it works, limitations, and how we improved on those limitations with an advanced signal processing technique called Maximum Likelihood Estimation (MLE). Lastly, I present my results and finish with a discussion on how ML can be used to improve image quality.

1.1 Gamma-Ray Sources and Types of Gamma-Ray Interactions

1.1.1 Types of Radioactive Decays Resulting in Gamma-ray Emission

There are many forms of radioactive decay, such as: neutron, spontaneous fission, alpha, beta, and gamma. Of these the last three (alpha, beta, and gamma) are the most common [2]. Alpha decay occurs when unstable, heavy nuclei release an alpha particle (also known as a ^4He nucleus). Beta decay occurs in nuclei where either the proton/neutron or neutron/proton ratio is high. In the case of a high proton/neutron ratio, this results in a β^+ decay: a release of a neutron, neutrino and the β^+ particle (a positron). In the other case, a β^- decay results in a release of a proton, anti-neutrino and an electron. [2]

Gamma decay occurs in multiple ways, one is after beta-decay; where the daughter nucleus is left in an excited state and transitions to a stable state via the release of a gamma-ray. Other ways are after interactions with other materials or gases causing different processes to occur for example, annihilation radiation; is where a positron released from a beta$^+$ decay quickly annihilates with a nearby electron (creating two 511 keV photons). Another example is in nuclear reactions which will also leave a nucleus in an excited state, releasing a gamma-ray upon de-excitation.

In the case of astrophysics, gamma-rays can also be created in a variety of ways, either via decay methods or astrophysical processes. For example, fusion in stars that are similar in mass to our Sun release the extra energy of that fusion of hydrogen to helium in the form of gamma-rays. Stars with higher masses than our Sun will fuse elements with higher atomic masses (up to iron).

”Inverse Compton scattering” is an example of a process that results in the creation of gamma-rays. Normal Compton scattering is when a photon undergoes an inelastic collision with an electron of an atom, transferring some of its energy to that electron (what happens afterwards is discussed in more detail in the next section). Inverse Compton scattering is similar, except that it is electrons scattering off of photons, giving enough energy to the photon to boost them into the gamma-ray regime. Examples of where this can occur are: bow shocks (such as supernova material colliding with its expelled but stationary gaseous shells), nebulae (in a similar process to supernovae but with stellar winds), cyclotrons and synchrotrons (both of which are processes where particles are accelerated through magnetic fields and collide with surrounding material), and jets [3]. Many sources contain one or more of these processes, including but not limited to, novae, pulsars, and active galactic nuclei. Additionally, both Compton scattering and nuclear interactions of high energy particles bombarding planetary surfaces can result in gamma-rays.

1.1.2 Interaction of Gamma-Rays in Matter

Gamma-rays can interact in matter via: gamma-nuclear interactions, coherent scatter [4], photoelectric absorption, Compton scattering, pair production, and secondary electron/positron interactions produced from the last three. Of these interactions, photoelectric, Compton, and pair production are the most important for gamma-ray detection measurements [5]. Photoelectric absorption is the most useful of the three as this is when all of the photon's energy is deposited in the material. The probability of one of these three interactions occurring depends on the energy of the incoming gamma-ray, the Z (atomic) number and the ρ (density) of the material. Low-energy gamma-rays (about 10 eV - 100 eV) tend to interact primarily via photoelectric absorption, about 100 eV - 100 MeV is mostly Compton dominated, and above that is pair production dominated (see figure 2.20 in [5]). Although a material may be dominated by a particular interaction, it is likely that all interactions do occur; with the exception of pair production as that requires a minimum of 1.022 MeV photon energy. The Z number dependence for these interactions can be approximated as: Z^n (where n is 4 or 5) for photoelectric, Z for Compton, and Z^2 for pair production [5]. Figure 1.1 shows how the probabilities of these interactions depend on photon energy as a function of the attenuation coefficient of the material (the volume a particle can travel through a material before undergoing any interaction).

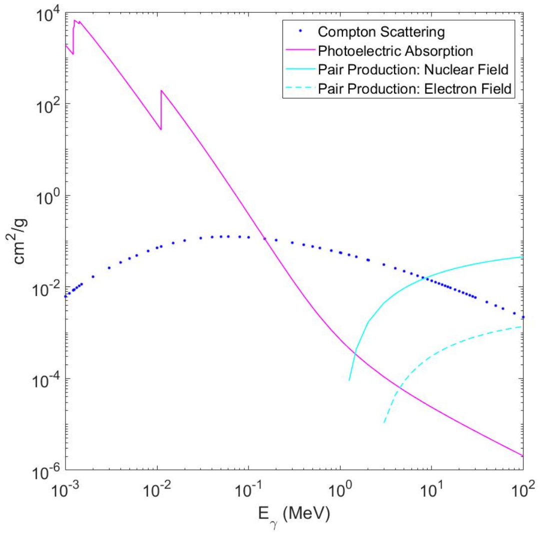

Figure 1.1: Energy Dependence of Gamma-ray Interactions in Ge. Plot shows the energy dependence of various gamma-ray interactions in Ge: Compton scatter, photoelectric absorption, and pair production. Data provided by XCOM: Photon Cross Section Database [6].

The attenuation coefficient can be found through Beer's Law [5, 7, 8]:

$$I = I_o * e^{-\left(\frac{\mu}{\rho}\right) * \frac{\rho}{t}} \tag{1.1}$$

where I is the attenuated intensity of the radiation source, after passing through an absorber material of a density, ρ, and a thickness t. I_o is the attenuated intensity of the radiation source. μ is the mass attenuation coefficient (variable on the y-axis in Figure 1.1. Detection of high energy gamma-rays therefor depends on both the density and the thickness of the absorber.

Both photoelectric absorption and Compton scattering interactions of gamma-rays are usually interactions between the gamma-ray photon and shell electrons of the atom, see Figure 1.2. Compton scattering may also occur with free electrons in the material, however, this is usually not the case when it comes to the specific materials described later in this chapter.

When an incoming gamma-ray collides with a shell electron, it can either give all or part of it's energy to the electron via a momentum transfer. In the case of photoelectric absorption, the gamma-ray energy has to be equal to or greater than the binding energy of the electron. After the interaction, the electron (termed a photoelectron) is freed from that shell with a kinetic energy equal to the difference: $E_{electron} = E_{photon} - E_{binding\ energy}$ [4, 5]. The vacancy created by the ejected photoelectron (typically in the K or L shell) is then filled either by: a rearrangement of electrons in the outer shells, an electron capture from free electrons in the medium, or the release of an Auger electron. In the first case, the rearrangement of electrons from the outer shells causes the emission of characteristic x-rays. These x-ray photons will have an energy equal to the energy difference between the two shells [5]. Electron capture will also result in an x-ray, with an energy equal to the difference: $E_{x-ray} = E_{free\ electron} - E_{binding\ energy}$. Alternatively, the atom can just transfer the extra energy of that vacancy to an outer shell electron causing that electron (termed an Auger electron) to be ejected [5]. This filling of the shell vacancy from the outer shells and causing these various results is called a cascade process [9].

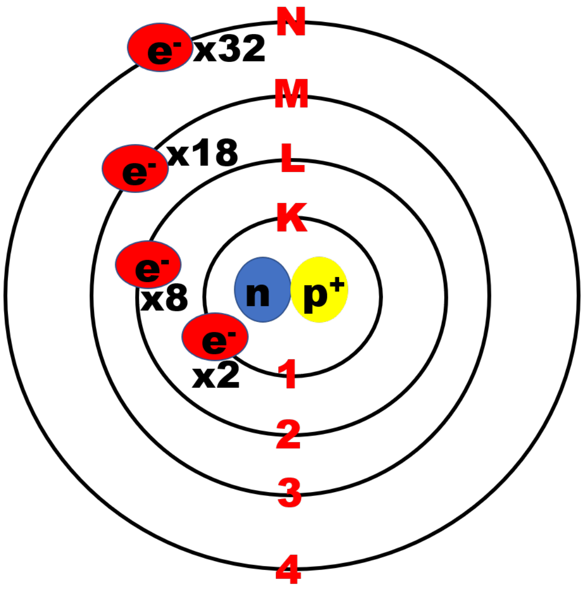

Figure 1.2: Schematic Depicting the Atomic Structure. n and (p^+) circles represent the atomic nucleus. Shells are labelled K,L,M, and N and also by shell number. The number of electrons that each shell can hold is also depicted and goes as $2k^2$ where k is the shell number.

Compton scattering is where the gamma-ray collides with the electron in an inelastic collision, transferring some of its energy to the electron (termed a recoil electron). The energy of the gamma-ray photon in this case is much greater than the binding energy of the electron, thus it cannot be absorbed. The amount of energy that is transferred depends on the scattering angle of the incident gamma-ray. The energies of the scattered photon and the recoil electron can be found through Compton's equation [5, 10]:

$$h\nu^{'} = \frac{h\nu}{1+\left(\frac{h\nu}{m_o c^2}\right)(1-\cos\theta)} = \frac{E_o}{1+\left(\frac{E_o}{0.511}\right)(1-\cos\theta)} \; ; \tag{1.2}$$

$$E_{re} = h\nu - h\nu^{'}$$

where h$\nu^{'}$ represents the scattered photon energy, hν represents the incident photon energy, and E_{re} is the recoil electron energy. The gamma-ray then continues in the direction it was deflected in, where it can either under go other scattering events, become photo-absorbed, or travel out of the medium entirely. Note that since the Compton scatter is usually with an outer shell electron, the cascade process described earlier from the photoelectric absorption does not occur.

Figure 1.3 shows a general gamma-ray energy spectrum of a detector depicting both the photopeak and the ”Compton plateau” and ”Compton Edge”. The photopeak results from the photon depositing all of its energy in the material. The Compton plateau represents the continuum of energies that Compton scatters may deposit (from $\theta = 0$ to $\theta = \pi$, see equation 1.15). The Compton edge is the result of $\theta = \pi$, which means it is approximately in the same place in the energy spectrum for all materials. The gap in between the Compton edge and the photopeak is a result of Compton scattered phoyons that travel out of the material. Additionally shown are the backscatter peak and the full width at half maximum (FWHM). The backscatter peak is a result of photons Compton scattering within surrounding materials and then traveling out of that material and into the detector (lead shielding for example). Lastly, the FWHM is used as a figure of merit (FOM) to determine the energy resolution of the detector. This is determined by fitting the photopeak to a Gaussian curve to obtain the width, and multiplying the width by 2.35 [5].

The fit is usually performed using a photopeak of ^{137}Cs, or an energy representative of gammas that the actual experiment will be measuring. The FWHM represents how far apart photopeaks in the energy spectrum must be in order to not overlap each other. The lower/smaller the FWHM value is, the closer the peaks can be and the detector in this case is said to have a high energy resolution [5].

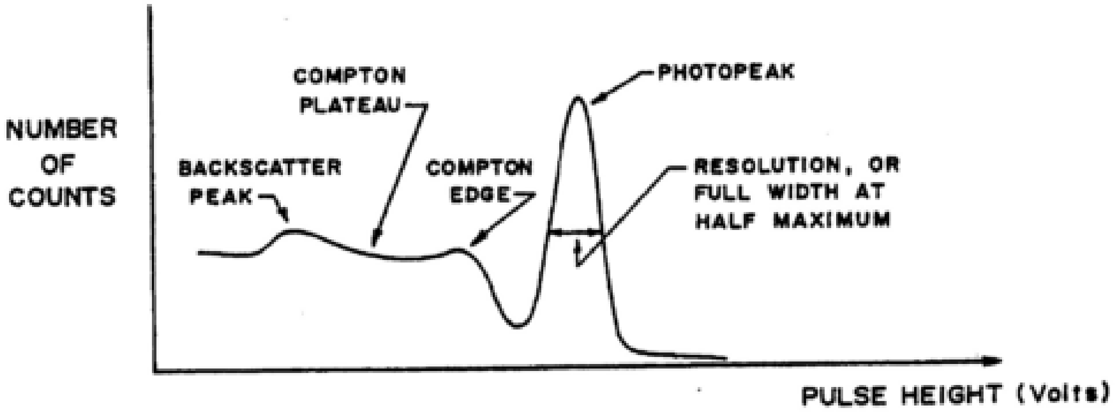

Figure 1.3: Schematic Representing a Typical Gamma-ray Spectrum. Figure shows general features of a gamma-ray energy spectrum: Photopeak, Compton Edge and Plateau, and backscatter peak. Also depicted in the photopeak is the FWHM. Source: [11].

Pair production is an interaction that occurs in the Coulomb field of the nucleus or an electron and requires that the energy of the incoming gamma-ray is at least 1.022 MeV (twice the rest energy of an electron). The gamma-ray is absorbed by the nucleus and an electron-positron pair is formed [5]. Similar to beta^{+} decay, the positron will quickly annihilate with a surrounding electron, creating two annihilation photons of 511 KeV each. The electron will also continue on, ionizing more electrons until it no longer has kinetic energy. The response in the energy spectrum in the presence of pair production is the addition of a " double escape peak" at $2m_oC^2$ less than the photopeak (not shown in Figure 1.3).

Another aspect of radiation interaction in materials in general is secondary interactions. The photoelectron, characteristic x-rays, Auger electrons, recoil electrons and scattered photons can either all go on and continue to ionize more electrons or result in some type of energy loss (charge trapping or phonon production are some examples). How the secondary interactions occur depends on the energy of the secondary photon/particle, the temperature and type of the material (see [12]). This will be discussed further in the next section when discussing different materials.

1.2 Scintillators vs. Semiconductors

There are a variety of radiation detectors that can be used for radiation measurements: gas chambers, scintillators (inorganic and organic, ceramic, glass, and plastic), and semiconductors (some examples are silicon, cadmium zinc telluride, and germanium). The focus of this section is on inorganic scintillators and semiconductors. Both gamma-ray astronomy and SPECT imaging have used both detector types. Although SPECT imaging has traditionally used the inorganic scintillator, NaI(Tl), and only recently has seen the use of semiconductors (cadmium zinc telluride, CZT, and high-purity germanium, HPGe). See: [13, 14, 15, 16, 17, 18] for examples.

Generally, materials are defined by their metallic properties; a material is either a conductor, semiconductor or an insulator. The difference between these three depends on the material's conductivity. The atomic lattice of the material is what determines the discrete bands of energy that electrons are able to exist in. The lower band is called the valence band and represents the bound electrons in the atomic shells. The upper band is the conduction band which represents the electrons that are ”free” to move about in the crystal. For metals, the highest energy band is partially empty, allowing for electrons to move about with only small amounts of energy needed. For insulators and semiconductors however, there exists an area in between the valence and conduction band called the forbidden band where electrons cannot exist (in pure crystals at least). When a photon with enough kinetic energy frees a bound electron, this electron is moved from the valence/ground state to the conduction/excited state. The amount of energy that it takes to complete this jump is called the bandgap energy, E_{gap}. For insulators $E_{gap} > 5$ eV and for semiconductors $E_{gap} \approx 1$ eV. The smaller the energy gap, the more metallic the material is. See pgs. 235 and 366 in [5] and references within for further information on band structure.

1.2.1 Description of how Inorganic Scintillators Work

In scintillators, an electron that has enough energy can move from the valence band (the vacancy in the valence band is called a ”hole”) to the conduction band. When it de-excites back to the valence band, it will do so by emitting what is called a scintillation photon. Pure crystals do not perform this process efficiently for two reasons, one is that the scintillation photon has a high chance of being re-absorbed, second is that the scintillation photon is at a wavelength that is too high for the visible range [5]. Thus, inorganic scintillators are made up of three compounds, the second compound provides additional energy levels within the forbidden gap and allows the scintillation photons to be emitted at lower energies. To shift the scintillation photon to wavelengths that are not re-absorbed, a third material is added, called a dopant. As an example, in NaI(Tl), sodium is the pure crystal in which the primary interaction takes place, iodide is the scintillation compound while thallium is the dopant ([5]). Lastly, the scintillation photon is detected by a light detector that is paired with the crystal such as a photomultiplier tube (PMT) or a silicon photomultiper (SiPM).

Figure 1.4 below shows a schematic of a scintillator detector. An incoming gamma-ray will interact within the crystal, knocking out a bound electron which goes on to ionize other electrons and creates many more electron-hole pairs. Instead of the electron moving to the conduction band, it is more correct to picture the electron-hole pair traveling (loosely) together until reaching an energy level/activator site provided by the scintillating compound. These are also called ’recombination centers’, because it is a location where the electron ’combines’ with it’s hole (i.e., de-excites) releasing a scintillation photon ([5]), see Figure 1.5. This photon is then seen by the light detector, which is a PMT in Figure 1.4. The window of the PMT is paired to the crystal using either optical grease or a light guide, and consists of a glass surface with a photocathode of a particular thickness behind it, or deposited on the back of the glass surface. When a scintillation photon comes in contact with the cathode, the interaction results in a release of an electron. Similar to the interaction in the crystal, the scintillation photon is absorped by a shell electron in the photocathode material which is then given enough energy to be freed. That electron (still termed a photoelectron), if it contains enough kinetic energy, will migrate to the surface of the material and escape into the vacuum chamber of the PMT tube. The amount of energy that the electron needs to escape the surface barrier is determined by the materials work function, W:

$$W = -e\phi - E_{Fermi\ level} \tag{1.3}$$

where -e is the electron charge, ϕ is the electric potential, and $E_{Fermi\ Level}$ is the chemical potential of the electron in the photocathode material. The electron needs to have kinetic energy greater than W to escape (+ enough energy to travel to the surface). [5]

The photoelectron is then accelerated via the electric field to each dynode stage. The dynode is another material similar to the photocathode in that it also releases electrons, but as a result of interactions with other electrons rather than photons. The dynode is typically chosen such that the result of the collision is many more electrons; as this occurs at each dynode stage, not only are more electrons created, but their kinetic energy increases as well as the dynodes are held at a voltage of several hundred volts; ultimately multiplying the signal output of the initial photoelectron at the photocathode. [5]

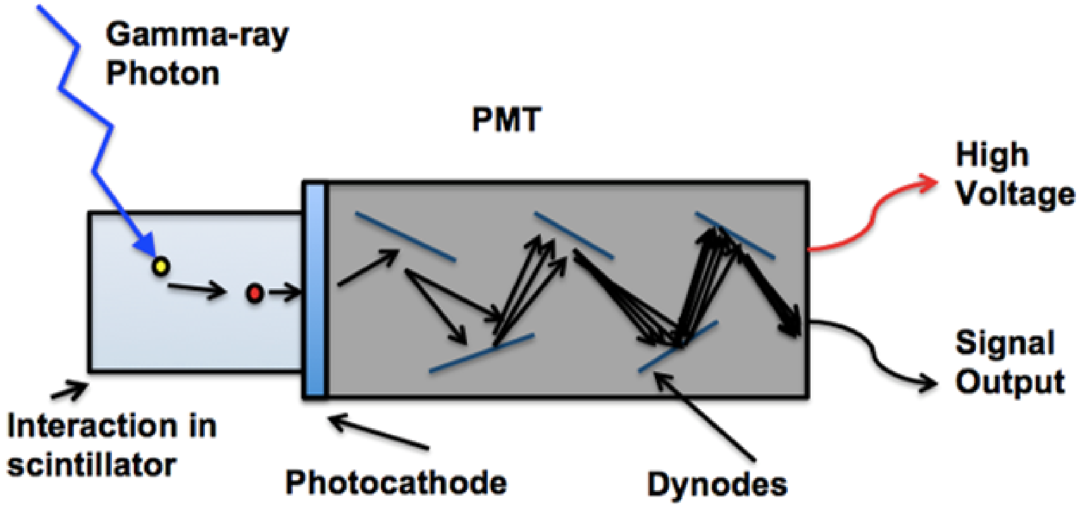

Figure 1.4: Schematic of a Scintillator. See text for description.

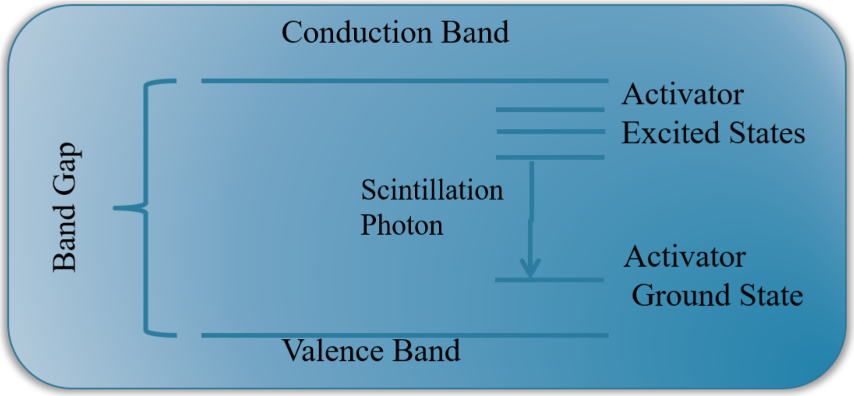

Figure 1.5: Schematic of the Scintillation Photon Process. See text for description.

The amount of light received by the light detector is called the ”light yield” of a scintillator detector, and is defined as the number of scintillation photons produced per incident photon energy. Light yield is one of the parameters considered in choosing a particular scintillator. A high light yield is desired for higher energy resolution. As far as electron-hole production, a high light yield is desired for better statistics as well because the scintillation process itself is inefficient. Of all the scintillation photons produced, only a small fraction is seen by the light detector. Only about 10% of the incident photon’s kinetic energy results in a detection at the light detector [15]. This is due to the competing processes that can occur in addition or in place of the recombination process, such as: phonon processes, phosphorescence, and quenching [5, 9, 15]. If it were not for these competing processes, it would be possible for scintillators to have energy resolution comparable to that of semiconductors [9].

Some commonly used scintillators and their properties for SPECT imaging can be found in Table 1.1 below.

Table 1.1: Commonly Used Scintillators in SPECT Imaging. Data from [19] unless otherwise noted.
*Z_{eff} can be approximated by adding all the atomic numbers in the compound and dividing by the number of elements in that compound.

Material	Density (g/cm)	Light Yield (ph/keV)	Energy Resolution (% FWHM at 140 keV)	Z_{Eff}*
Sodium Iodide (Thallium): NaI(Tl)	3.67	38	10.8 [20]	48
Cesium Iodide (Thallium): CsI(Tl)	4.51	65	8-9 [21]	63
Lanthanum Bromide (Cerium): ($LaBr_3(Ce^{3+})$)	5.30	61	6 [22, 23]	50
Lanthanum Chloride (Cerium): ($LaCl_3(Ce^{3+})$)	3.86	49	7.5 [23]	44
Yuttrium Orthoaluminate (Cerium): $YAlO_3(Ce^{3+})$	5.50	21	25 [24]	29.5

1.2.2 Description of how Semiconductors Work

Semiconductors, unlike scintillators, have no extra conversion process (i.e., from electron-hole pairs to scintillation photons) as the electron-hole pairs can be measured directly. As seen in Figure 1.6, the gamma-ray interacts in a semiconductor (Figure 1.6 is specifically for a detector with strip electrodes, but the process is the same for any electrode configuration) in the same way as it does in the scintillator in creating many electron-hole pairs. These pairs create what is called a charge cloud, however, by applying a bias voltage across the crystal, the electrons and holes will migrate to their respective electrodes ([5]). As they migrate, the electron and holes will induce a charge on the electrodes that can be integrated over time ([25]) to produce a measurable signal. This process is explained in detail in section 1.4.1. Other electrode configurations are planar, Frish-grid, or pixel ([26]) and are also discussed in section 1.4.1. Table 1.2 lists the commonly used semiconductors for SPECT imaging.

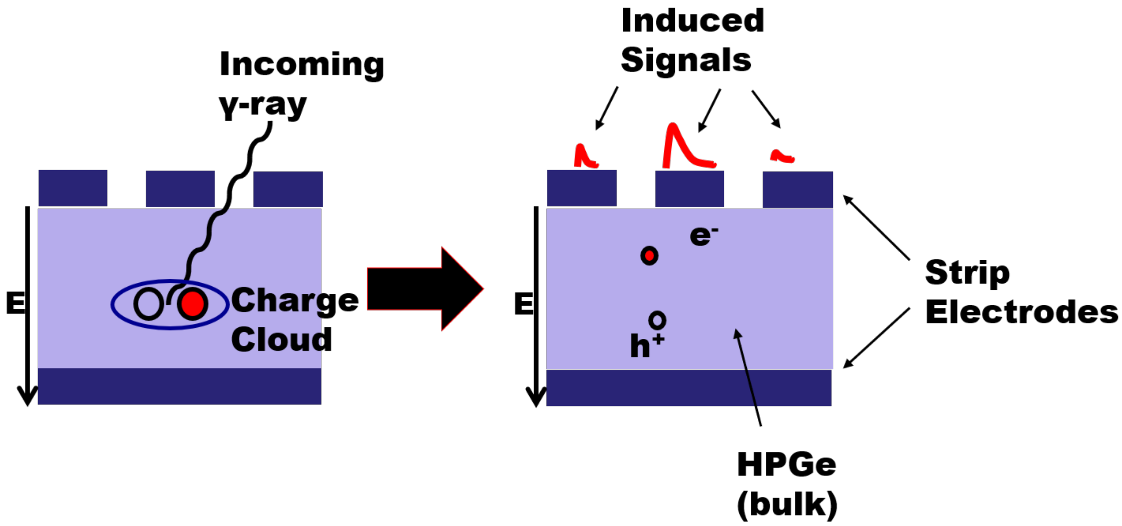

Figure 1.6: Schematic of Signal Production in a Double-Sided, Striped, High-Purity Germanium Detector. E is the electric field (arrow designates direction), red circle designates the electrons (e^{-}), and the open circle designates the ”holes” (h^{+}) each representing their respective charge clouds (but shown as one circle for simplicity.)

Table 1.2: Commonly Used Semiconductors for SPECT Imaging.
*Z$_{eff}$ can be approximated by adding all the atomic numbers in the compound and dividing by the number of elements in that compound. Data from [13].

Material	Density (g/cm)	$\mu_e\tau$ / $\mu_h\tau$ (cm^2/V)	Energy Resolution (% at 140 keV)	Energy/ e-h pair (eV)	Z$_{Eff}$
Silicon (Si)	2.33	0.42/0.22	N/A see [27]	3.61	14
Cadmium Zinc Telluride (CZT)	5.82	3×10^{-3} / 5×10^{-5}	2-5 [28, 29]	5	45
Cadmium Telluride (CdTe)	5.85	3×10^{-3} / 5×10^{-4}	6.6 - 8 [30, 31]	4.43	49
High-Purity Germanium (HPGe)	5.32	0.72/ 0.84	< 1 [14, 32, 33]	2.98	32

1.2.3 Fano Factor

It's important to mention that any type of detector will experience fluctuations in its response that will affect the centroid and width of the photopeak. These fluctuations are due to variations in power supplies and/or operating conditions, random and statistical noise within the detector system, and random noise from the measurement of the radiation decay itself. This last fluctuation is the limiting factor in the energy resolution of these detectors. [5]

The formation of electron-hole pairs can be assumed as a Poisson process, however, if this is the only source of fluctuation and the mean value of the distribution of counts is equal to or greater than 25 or 30 [5], then the response of the detector can be assumed to be Gaussian [5, 15]. Under this assumption, for a total of N detections, the variance of the total number of pairs is just $\sqrt{N}$, and the Gaussian parameters are described as the following [5], for a linear detector:

$$H_o = KN;\ \sigma = K\sqrt{N};\ FWHM = 2.35\sigma = 2.35K\sqrt{N} \tag{1.4}$$

where H_o is the amplitude of the photopeak, K is a proportionality constant, and σ is the Gaussian width. The limiting resolution due to Poisson statistics is [5]:

$$R_{Poisson} = \frac{FWHM}{H_o} = \frac{2.35}{\sqrt{N}} \tag{1.5}$$

In scintillators, the energy resolution tends to be poor compared to semiconductors due to mostly phonon generation and other radiative and non-radiative processes [9, 15, 34]). The conversion processes that take place after the initial gamma-ray interaction involve secondary interactions that can divide the photon energy into smaller energy deposits in various ways [5, 9, 15, 34]. Examples are phonon generation, cascade processes, delta rays, and Landau fluctuations. The last two involve secondary electrons and depends on the number density of the electron-hole pairs created along the ”ionization path” [9]. Delta rays are a result of knock-off electrons (from the secondary electron) which themselves continue on and lose energy via collisions. Landau fluctuations are a result of the difference in the number density of the electron-hole pairs at the beginning and the end of the ionization path. All these processes, collectively described as the ”non-proportionality” of the scintillator [5, 9, 15, 34], can occur in a variety of ways, with the smaller energy deposits also being variable.

Semiconductors on the other hand do not have a conversion process for the electron-hole pairs, which can be measured directly (see 1.4.1). Although phonon loss and trapping in some semiconductors do occur, for example, Ge experiences phonon excitation at temperatures greater than 200 K [12] while Cadmium Zinc Telluride (CZT) is known to experience trapping of charge carriers dependent on bias voltage and depth [35, 36, 37]. Both can be minimized, Ge is operated at 70-80 K, while the electrode configuration and signal processing methods discussed in section 1.4.1 are used for CZT. Thus, because a large number of charge carriers (electrons and holes) with very little loss to competing processes (if this does occur, it is unlikely that these processes will subdivide the initial photon energy differently) the resolution for semiconductors is actually better than the Poisson resolution. This is sometimes referred to as ”sub-Poisson” [15] resolution. To quantify this a value called the ”Fano Factor” is used [5, 15]:

$$F = \frac{Observed\ variance\ in\ N}{Expected\ Poisson\ variance} \tag{1.6}$$

This quantity is approximately 0.07 to 0.15 for Si and Ge. For scintillators it is assumed to be about 1 (but is not precisely known since electron-hole pairs cannot be measured directly).

Using the Fano factor, equation 1.5 becomes [5]:

$$R = 2.35\sqrt{\frac{F}{N}} \tag{1.7}$$

The difference in the Fano factors between scintillators and semiconductors is that for the scintillators,

.

1.3 Applications: High Energy Astrophysics and Nuclear Medical Imaging

1.3.1 High Energy Astrophysics

As mentioned earlier, gamma-rays can be produced via different mechanisms (de-excitation, beta-decays, annihilation, etc., see section 1.1.1). These processes are considered to be non-thermal radiation; they are not produced from movements of particles. However,these non-thermal processes tend to be dominated by thermal processes in lower energy regimes. At high gamma-ray energies (from 10^2 MeV to TeV energies), this is no longer the case, making them a good source for observing and studying non-thermal processes ([38]). Such topics (among many others) as the extra-galactic background, cosmic nucelo-synthesis, and pulsars are of interest because of their underlying physical processes ([39, 40]). From observing gamma-rays from these different astrophysical phenomena we can obtain information on the history of the universe, the composition of heavier elements and where they are located, improve our understanding of ”extreme particle accelerators” (such as, active galactic nuclei (AGNs), cyclotron and synchrotron processes, jet formations, etc.) along with the decay of atomic nuclei and particles, particle annihilation, and the interaction of these non-thermal particles with photons and matter). [38, 41]

The Cosmic Background (CB) is isotropic, homogeneous (on large scales) and consists of photons that span a range of ages ([42]). These photons are radiation that comes from outside our solar system and Milky-Way Galaxy. Thus, the CB has information on the history of our universe, with each energy regime portraying different information about all the processes within it ([42]). These energy regimes are: radio, microwave, infrared, optical, ultraviolet, and x- and gamma-rays. Figure 1.7 shows the radiation intensity (the amount of photon energy/square area, called the radiant flux) received per unit solid angle (the area that the stellar object covers on the telescope/detector using the angle that the object extends to the telescope/detector, called a steriadian, ”sr”) as a function of frequency. This figure represents the energy distribution of photons in the universe emitted from sources over cosmic history [42]

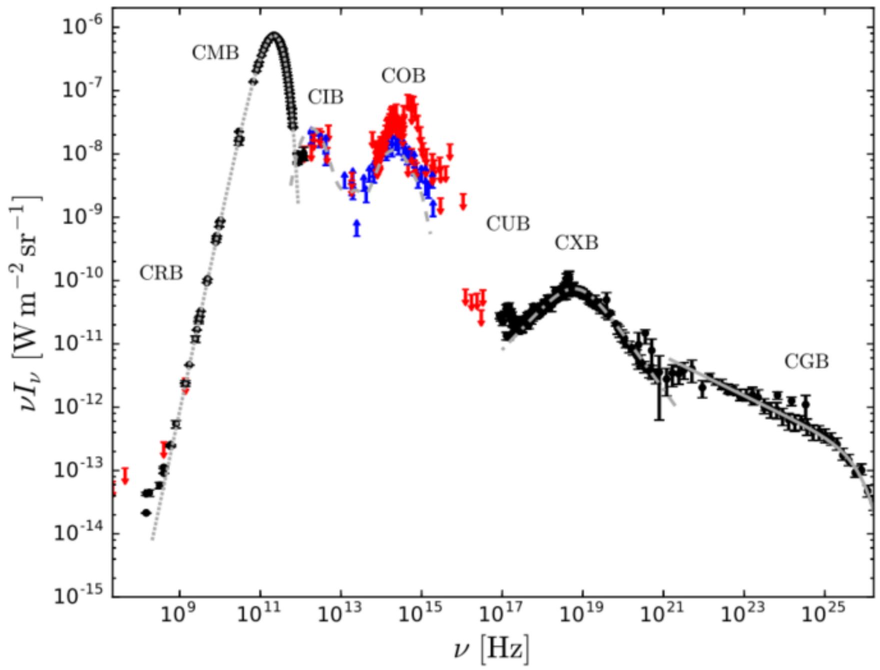

Figure 1.7: Full Spectrum of the Cosmic Background Radiation. Back dots with error bars represent detections, red and blue arrows represent upper and lower limits respectively. Gray lines represent models of the different sections. Source [42].

In the gamma-ray regime, it is the quasars/blazars and supernovae that contribute the most to the cosmic gamma-ray background (CGB) ([42]). These gamma-rays then contain information on the history of the most energetic processes within our universe. Extra-galactic gamma-rays were first detected in the 1960's ([43]). Now, with the second catalog of FERMI data ([44]), 4,547 gamma-ray sources have been found, with 518 identified (via a positioning method). Of those 518, positional counterparts (mostly blazars) have been found, while 77 remain unidentified ([44]). Figure 1.8 shows these sources from the FERMI 5-year map where diffuse extra-galactic cosmic background, pulsar and supernova remnants, and blazers are shown [45].

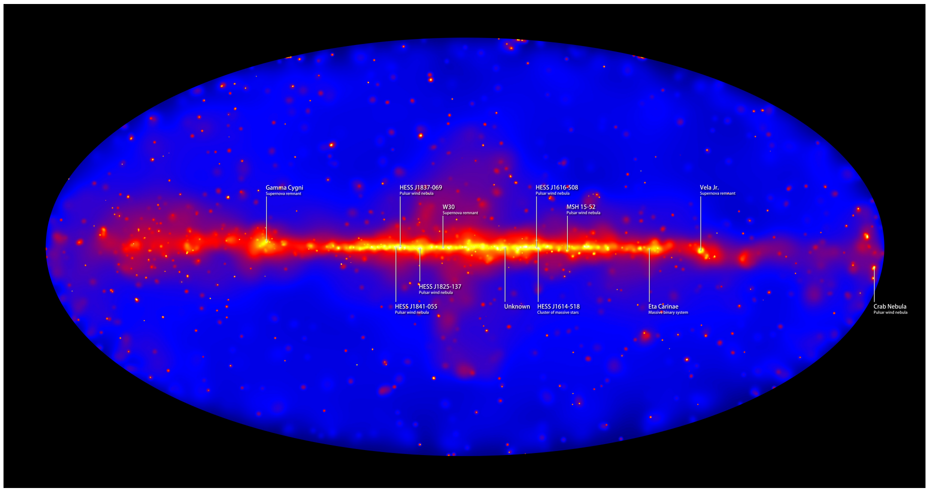

Figure 1.8: The Entire Sky in Energies from 50 GeV to 2 TeV. The diffuse glow that fills the sky is the extra-galatic cosmic-ray background. The glowing line in the middle of the map is our Milky Way galaxy. Discrete gamma-ray sources (seen as smaller dots) include pulsar wind nebulae and supernova remnants, and blazars. Labels show the highest-energy sources, emitting gamma rays exceeding 1 TeV. Source [45]

Another reason that gamma-rays are of particular interest is the ability to use them to map unstable nuclei throughout the Milky Way. Knowing what these nuclei are, their abundances, and their locations can give us insight into stellar interiors. It is expected that unstable nuclei created in supernovae that have not decayed within the source and get ejected into the interstellar medium, can be observed via their characteristic gamma-ray spectrum ([46]). For ^{26}Al, the total amount in the galaxy matches the amount that we would expect to see from supernovae (with 1 supernovae every 100 years) ([46]). This would also require the isotope to have a long half-life. That of ^{26}Al is around one Myr; which is low on the time scales of star cluster formation/lifetime, but not for supernovae (tens of kyrs) ([46]); meaning that for supernovae, ^{26}Al stays around after the source is gone. In order to investigate other nuclei however, longer observations are needed; for example, currently ^{60}Fe has a lower count rate compared to ^{26}Al than expected [46]. Figure 1.9 shows the ^{26}Al radiative flux as a function of energy for various locations along the galactic plane. This is from the European Space Agency's (ESA) spectrometer, SPI, on the INTEGRAL (**Inte**rnational **G**amma **R**ay **A**strophysics **L**aboratory) satellite. SPI uses

19 HPGe detectors shielded by another gamma-ray detector, called bismuth germanium oxide (BGO). Other locations in the sky or galactic plane have not been measured as the ^{26}Al flux is too low.

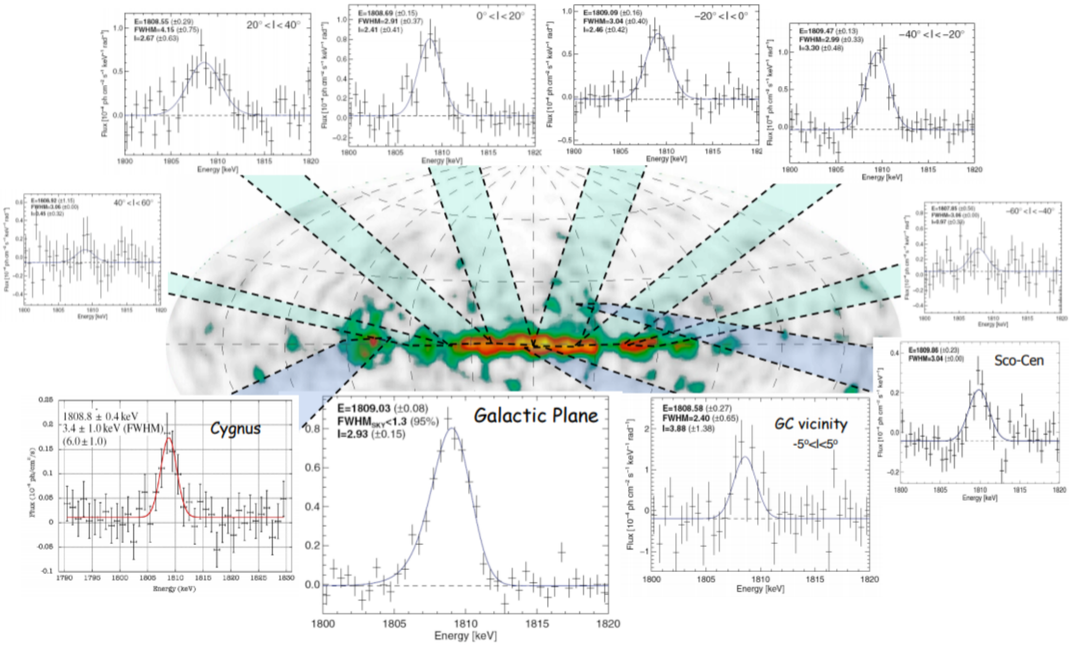

Figure 1.9: Energy Spectra of the ^{26}Al Line taken from Various Regions Along the Plane of the Milky Way. Data was obtained from the SPI instrument on the INTEGRAL mission (currently ongoing). Source: [47].

The last astrophysical phenomenon discussed here will be pulsars, particularly ”the Crab”, as it is one of the closest and most well studied (at 2kpc away and 1.3*10^{38} ergs^{-1} [48]). The Crab consist of a stellar nebula and pulsar, and is considered to be a ”Pulsar Wind Nebula (PWN)”. PWN’s are the result of the pulsar wind interacting with the nebula, leaving a bubble of shocked relativistic particles [49]. It is a complex system, especially when phenomena from the pulsar interact with the nebula. Figure 1.10 shows a schematic for a sample PWN from Gaensler and Slane, 2006 [49]. In the figure, (from outer to inner) is the swept up interstellar material, the hot/cold boundary separated by the reverse shock, and the central pulsar and nebula. The insert further shows the pulsar wind shock.

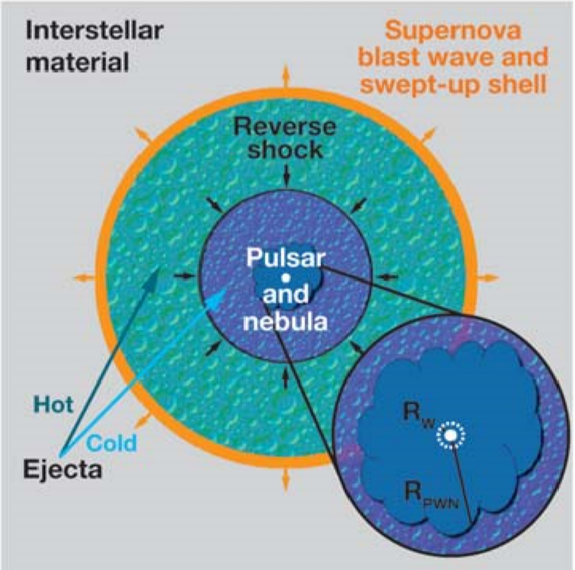

Figure 1.10: Schematic of a Pulsar Wind Nebula. Source [49].

One interesting aspect of the Crab is that it can be observed across all wavelengths. Gamma-rays in these systems come from the pulsar itself, seen in the ”jets” of radiation coming from both sides of the pulsar, although the Crab has only one jet from our point of view. These jets come about from the process of the pulsar spin. As it spins, the pulsar loses angular momentum over time, however, only about 1% of the angular momentum energy is released in electromagnetic (dipole) radiation [48]. The resulting magnetic field and magnetic moment come from the changing rotation speed of the pulsar. As the magnetic moment precesses, a torque is created making a ”current sheet” [48]. The wind from the pulsar travels through this magnetic field clashing with the material from the nebula and causes the wind termination shock, which in turn accelerates the electrons/positrons to relativistic speeds, creating the synchrotron/jet structure [49]. Depending on how the magnetic moment is aligned, the gamma-rays will be polarized. Thus, measuring the degree of this polarization would give information on the synchrotron and the magnetic moment. Other information that we can get from knowing the degree of the polarization in pulsars and other systems are [50]: information on the geometry of the system, differences in models of blazars (leptonic or hadronic), and Lorentz invariance violation.

In reality, gamma-ray polarization measurements are difficult to do. There are fewer photons at such high energies and they can only be seen outside of the Earth's atmosphere; meaning that we can only observe gamma-rays with satellites, sound rockets or high altitude balloon missions. Radiative flux from the Crab is 10^{-8} to 10^{-12} ergs cm^{-2} s^{-1} at energies of 1 MeV to 10^4 GeV. Meaning that at this energy range, the number of gamma-ray photons is $\approx 10^3$ to $\leqslant 1$ per detector area per second [48]. Additionally, the sensitivity of the measurement depends on the type of interaction the polarized photon has within the detector [50, 51] and the detector response to that interaction. For Compton scattered events, in order to "see" the polarization, the Compton scatter must occur 90° to the electric field vector of the gamma-ray photon [51]. This limits Compton cameras to seeing polarized gamma-rays of energies to only a few MeV as the angle of the scattered photon decreases with energy (see derivation in Ilie, 2019 [51]). The left schematic in Figure 1.11 shows the orientation of what a polarized Compton event would look like with the incident gamma-ray entering normal to a surface.

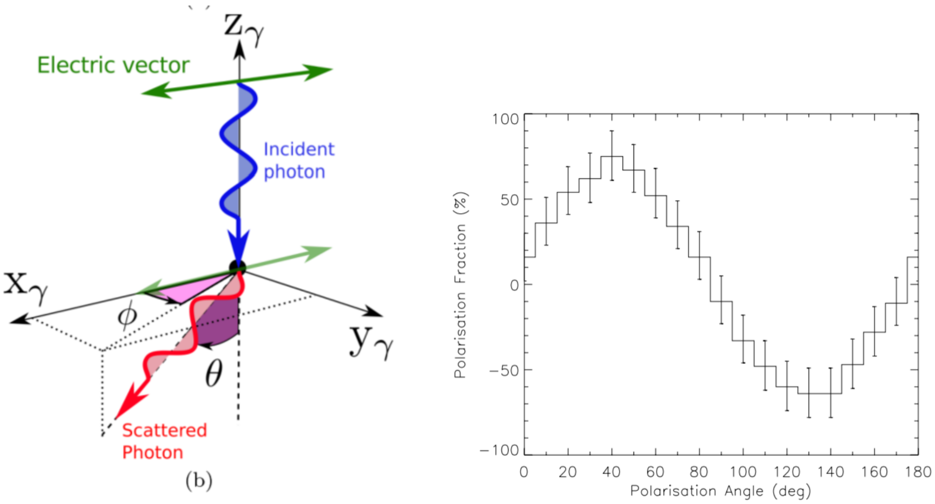

Figure 1.11: Compton Polarization Schematic and Data. Left: schematic shows the relevant angles of a polarized gamma-ray Compton scattering within a medium. The Z-axis is in the direction of the photon while the X-axis is the direction of the polarization. From source [52]. Right: Modulation curve for the 230 to 850 keV energy band of the SPI instrument on INTEGRAL while looking at Cygnus-X. Source [53].

ϕ is the azimuthal direction of the scattered photon with respect to the direction of polarization. θ is the angle between the incident photon and the scattered photon. This information is used to determine the ”modulation curve” of the detected photons. First a histogram of the azimuthal angles that are formed between the scattered photon and a reference angle is made. Then that data is fit to the following:

$$M(\phi) = A + B\, cos^2(\phi - \phi_o) \tag{1.8}$$

where **A**, **B**, and $\boldsymbol{\phi_o}$ are free parameters. This is the equation for the modulation curve, and is supposed to retain the same angle dependence as the scattered photon. If there is a dependency, the this curve is flat, if the curve is not flat as in the right plot of Figure 1.11, then the photons are partially polarized.

In a pair-production event the polarization is ”seen” based on the orientation of the electron-positron pair [51]; this type of polarization has never been measured outside of a laboratory setting due to the small cross-section of the interaction (and the low flux of gamma-rays at this energy).

An example of a current detector system for polarization measurements is the **CO**mpton **S**pectrometer and **I**mager (COSI, formally known as the Nuclear Compton Telescope). This instrument consists of 12 DSS HPGe detectors, with 37 strips on each side (2mm pitch with 0.25mm gaps). This instrument will be referred to throughout the dissertation so as to make comparisons of our positioning methods and system performance.

1.3.2 Single Photon Emission Computed Tomography (SPECT) Imaging

SPECT is a nuclear imaging technique that involves the injection of a small amount of a radio-tracer. This radio-tracer will accumulate in the target of interest (a tumor site for example) and emit gamma-rays in all directions. A gamma-ray detector system then takes a collection of planar images of the object, person, or small animal, at many angles. The projection images are then mathematically reconstructed offline into a three-dimensional image. The gamma-ray detector is paired with a collimator to restrict the angular acceptance of the incident gamma-rays. This is done to increase the accuracy of estimating the location of the photon.

Small-animal SPECT has been important in the development of radio-tracers and radiopharmaceuticals that can be used in diagnostic and therapy applications. Small-animal models allow for the study of disease processes that cannot be done in human trials. Through these models, we can study the onset of a disease and its progression, possible drug treatments, and effects of radiation treatment on tumors with specific cancer targeted molecules ([54]). While there are great differences between clinical and pre-clinical SPECT (e.g., field of view, scatter and attenuation correction, efficiency and radiation dose [15, 55]), both types of detector systems require high energy and spatial resolution for an accurate reconstructed image of the radio-tracer distribution. Spatial resolution is the minimum distance between two distinct points as seen by the imaging detector. This is essentially the FWHM multiplied by the pixel (or sub-pixel) size of the detector. The sensitivity of the imaging system is the product of the efficiency of the collimator and the intrinsic detection efficiency. Since the collimator is what allows the photons into the detector, the sensitivity is dependant on the type of collimator used and its: thickness, hole diameter, opening angle, and the material used to make it. Different types of collimators will be discussed in section 1.4.2.

In addition to the spatial resolution, for any imaging detector system, the image quality also depends on contrast and noise (both random and structural). While this work focuses on improving the spatial resolution, these topics are not completely independent of each other; there is always a trade-off between spatial resolution ($\mathbf{R_{total}}$) and sensitivity (**S**) ([13, 54, 56]) of the pinhole:

$$R_{total} = \sqrt{d^2\left(1 + \frac{1}{M}\right)^2 + \frac{R_{det}^2}{M^2}} \tag{1.9}$$

$$S = \frac{d^2}{16h^2} cos^3(\theta) \tag{1.10}$$

where **d** is the pinhole diameter, **M** is the magnification, $\mathbf{R_{det}}$ is the detector's intrinsic spatial resolution (the detector's spatial resolution without the collimator), **h** is the distance from the object to the pinhole, and θ is the angle the photon's path makes from the object to the pinhole ([13]) (see Figure 1.3.2). The pinhole diameter can be decreased to obtain higher spatial resolution, but that will also decrease the sensitivity.

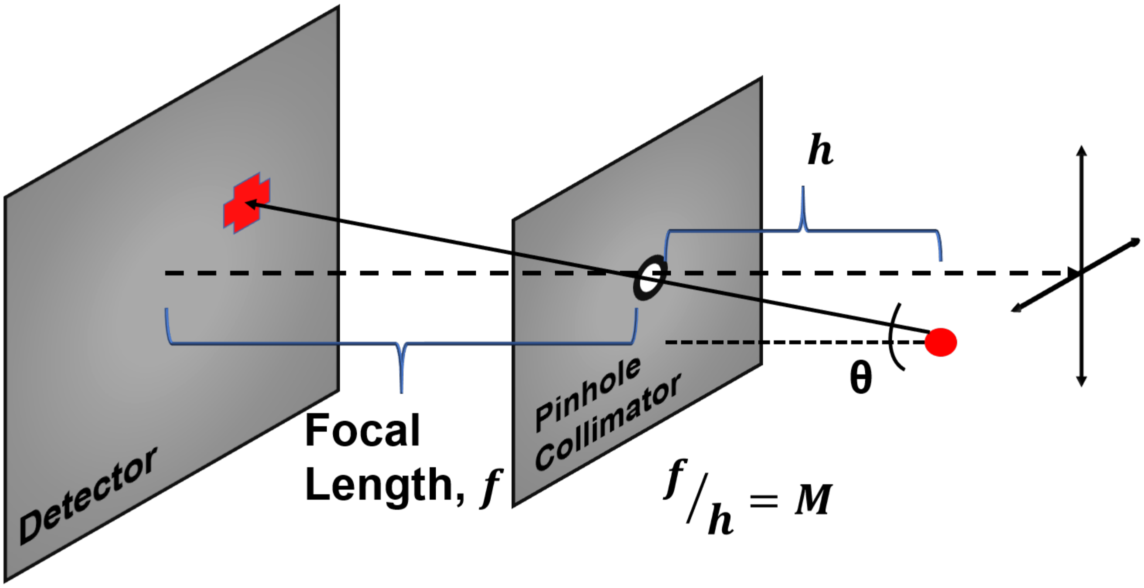

Figure 1.12: Schematic of a Typical pinhole Configuration. Adapted from [14].

Energy resolution also affects the image quality. Equation 1.6 is the lowest energy resolution a detector can theoretically obtain; experimentally, the energy resolution is the $\frac{FWHM}{Photon\ energy}$. Energy resolution is affected by the widening of the photopeak due to noise and events that do not fully deposit their energy into the detector. This widens the photopeak and the FWHM which in turn worsens the spatial resolution by decreasing the contrast.

The crystal that is typically used for the detector material in SPECT imaging has been NaI(Tl). This detector system design is called the ”Anger Camera,” after it’s original inventor, Hal Anger [57]. NaI(Tl), a scintillator, has been favored because it is easy to grow, can be grown into large sizes (good for full body imaging in some clinical applications) [19]. However, as seen in section 1.1.2 and in Table 1.1, NaI(Tl) has poor energy resolution at 140 keV (a widely used radionuclide, Tc-99m, emits at 140 keV). While other scintillators have been developed and used, limitations such as difficulties in crystal growth and lower light yield have limited their use as an alternative for SPECT imaging ([19]).

Semiconductors however, produce approximately 10 times the number of charge carriers per MeV deposited due to their lower ionization energy ([5]). Two semiconductors of particular interest in SPECT imaging are cadmium zinc telluride (CZT) or cadmium telluride (CdTe), and germanium (Ge). Some limitations do occur with semiconductors, such as poor charge collection at the electrodes and charge trapping. While CZT and CdTe suffer from charge trapping, Ge does not. This is discussed further in the next section.

Ge also has better intrinsic energy resolution, which allows for the ability to place a narrower constraint of photons accepted based on a narrower energy window (140 ± 1 keV vs. ± 5 keV for example). This provides for the possibility of multi-isotope imaging ([14]) and better scatter rejection ([58]). Scatter rejection in this context is being able to reject events that have scattered within the imaging object before entering the detector.

Hesitation in using Ge in the past was in large part, due to the fact that the material needed to be cooled to 77 K to prevent the creation of charge carriers without a radiation photon interaction (typically called dark current). This is due to the small band gap of the material (see Table 1.2). Now, it is possible to cool the material mechanically (instead of using a nitrogen dewar), making these detector systems more portable ([14]).

The next section goes into further detail about design components of the detector systems, including the strip electrode design for our HPGe detector system.

1.4 Detector Design

In designing an imaging system,the scientific objective and environment of the measurement need to be kept in mind as decisions on key detector and system properties will need to be made. First, three key properties are: detection efficiency and energy and spatial resolution [13]. Additionally, other properties like: count-rate capability, mechanical robustness and cost may also need to be considered. In respect to these properties, this section describes the signal generation in semiconductors and how different electrode and collimator designs affect the detector response.

1.4.1 Electrode Design

In section 1.1.2, the interaction of a gamma-ray photon in a semiconductor material was described, and it was stated that the migration of the electron-hole pairs is what induces the signal on the electrode. The next step is to measure this signal and tie it (1) back to the energy of the interacting gamma-ray and (2) the location of interaction within the detector material. From knowing the location of the interaction in the detector space we can then figure out where the gamma-ray originated from in the object space, this involves image reconstruction which will be discussed further on in this section.

The process of the charge carrier migration can be described as an electrostatic problem with two parallel conducting plates which can be solved using: method of images, Green's functions, or the "Shockley-Ramo Theorem" [25, 26, 59, 60]. The latter method is a simpler form of the second method and was demonstrated independently in the late 1930's by W. Shockley [25] and S. Ramo [59].

The Shockley-Ramo theorem states that the charge induced on an electrode due to a moving charge can be described as:

$$I = E_o(\vec{r})\ q\ v \tag{1.11}$$

where **I** is the instantaneous current on the electrode with the charge at a particular location. $\mathbf{E_o}(\tilde{\mathbf{r}})$ is the "weighting" electric field at that location, the field that would exist at this position with the specified electrode set at unit potential and all others set to zero and no charges present [25, 26, 59, 61] **q** is the electric charge, and **v** is the instantaneous drift velocity [25, 26, 59, 60].

This equation is derived from solving Poisson's equation using Green's function with Dirichlet (potential at a surface, but no charge within the volume) boundary conditions [26]. The novelty in the Shockley-Ramo theorem was that it reduced the number of computations needed to find **I**. Previously, the process would have involved calculating $\mathbf{E}(\tilde{\mathbf{r}})$ at each position, then integrating that to get the induced charge over the surface containing the electrode [26]; instead, the electrode in question is set to a potential of 1 while all other electrodes are set to zero. This allows for a much simpler calculation of the induced charge via finding the potential, a.k.a the weighting potential for this system (with one electrode set to potential of 1). The weighting potential is not a potential in the normal sense, but rather a representation of how much the induced charged changes as the point charge moves [5, 26, 60].

The drift velocity from equation 1.11 depends on the mobility (μ), and the applied electric field [61]:

$$\vec{v} = \mu \cdot \vec{E} \tag{1.12}$$

In some materials, such as CZT, the mobilities of the electrons and hole are different. This can potentially be an issue when there are impurities and defects in the crystal that causes trapping of the slower charge carrier. The "$\mu\tau$ product" is a parameter that describes how long a charge carrier can travel before it is trapped. τ is the lifetime of the carrier, or how long it exists before it recombines with another electron/hole. Lastly, the charge induced over a time period (t = 0 to t = t') is found from both the actual potential and the weighting potential via [61, 62]:

$$q_{induced} = q \int_0^{t'} dt \int_\Omega \mu \cdot n(\vec{r},t) \cdot \nabla\phi \cdot \nabla\phi_o \, d^3r \tag{1.13}$$

where Ω defines all the points in the detector volume and $n(\vec{r},t)$ is the charge carrier concentration, $\nabla\phi$ is the electric field, and $\nabla\phi_o$ is the weighting field. Note that equation 1.13 is written for a single type of charge carrier, but electrons and holes both need to be accounted for (except in instances where only one charge carrier is important, like in single polarity charge sensing discussed below). Many solutions to finding $q_{induced}$ have been done to various electrode geometries such as [60],[26]: planar, coplanar, Frisch Grid, pixel and strip electrodes.

Regardless of the electrode geometry, the signal must still be measured. Referring to figure 1.6, the voltage amplitude of the signal arises from the induced signal as discussed above. In general, this signal is increased by an instrument called a pre-amplifier (pre-amp) and then sent to be read out either by a digital or analog analyzer. There are quite a few different types of pre-amps and timing methods for measuring the signal, a good list of these can be found in Knoll, 2010 [5].

In a planar configuration, for example, where two sides of the crystal are made to be the electrode contacts, the maximum amplitude of this voltage is [5]:

$$V_{max} = \frac{Q}{C} \tag{1.14}$$

where Q is the total charge induced and C is the capacitance of the detector, amplifier, and connecting cables. Assuming that there is no trapping of electrons within the detector [5, 26] and if C is constant (in cases where it is not, charge sensitive amplifiers are used), then the amplitude of the signal is proportional to the total charge induced on the strip [5]. This simplification also assumes that the velocities of the electrons and holes are similar. In silicon and germanium detectors, for example, the hole mobility is within a factor of 2 to 3 of the electron mobility [5]. If trapping does occur, the pulse amplitude is reduced if the charge carrier is not un-trapped in the signal collection time. If a charge carrier is trapped and then untrapped, the leading edge of the pulse is slowed which affects the time needed to collect the signal. Overall, trapping leads to a low energy tail in the energy spectra of the semiconductor (no Compton scatter plateau) [5]. Equation 1.14 essentially works for any planar/bar type of detector, what changes is the calculation for the induced charge, Q, which is based on the electrode geometry.

For CZT, hole migration is much slower than electron migration (see 1.2) and due to crystal impurities and defects CZT is also prone to hole trapping; Frisch and coplanar grids were the first electrode designs used to reduce the effect that this had on the pulse amplitude. Both Frish [5] [26] and Coplanar [26] configurations are designed to be sensitive to only one type of charge carrier, a.k.a, ”single polarity charge sensing” [63] . Frisch grids were originally designed for gas/liquid detectors to be sensitive to the movement of only electrons by using a gridded electrode within the detector volume. The grid, along with the anode and cathode electrodes, are biased in such a way that only electrons pass through [63]. The induction that would have occurred from the migration of the ions are effectively shielded so that the signal arises from only the migration of electrons between the Frisch grid and the anode. It was not realized how to implement this idea for a semiconductor until the early 2000’s [64]. What followed were electrode and algorithm designs for what is now known as ”virtual” Frisch grids [65, 66, 67]. The concept is similar to the gas detector design, with the difference being that the Frisch ”grid” is just another electrode placed either at the cathode side (or any other side excluding the anode) of the crystal [64, 66, 67]. See Figure 1.13 for an example.

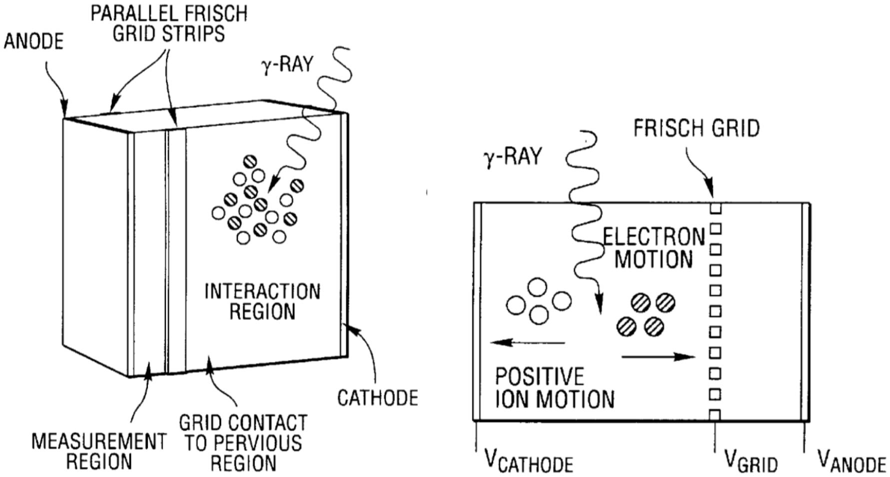

Figure 1.13: Schematics of a Semiconductor with Frisch Grid Electrode Design. Note, the Frisch grid depicted here is on the surface of the semiconductor. Source: [64].

Coplanar grids were developed before virtual Frisch grids in the mid-90’s [63]. This design consists of strip electrodes that are connected in an alternate manner so that they make an ”interdigital” grid [63] (see Figure 1.14) on the anode side of the crystal while the cathode collects the holes. The two grids are biased slightly differently so that the electrons migrate to only one of the grids, the ”collecting grid”, the other grid is called the ”steering grid”. This is to prevent the signals from having unintended different polarities, and reduced amplitudes from charge sharing [63].

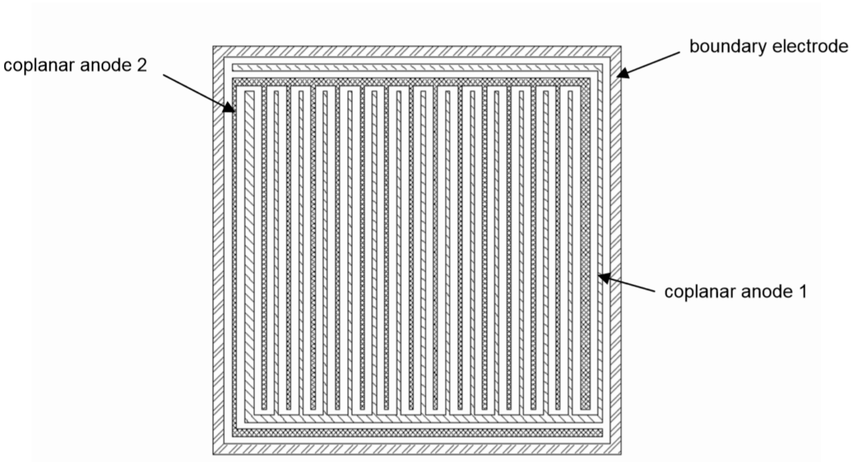

Figure 1.14: Schematic of a Coplanar Electrode Design. Source [68].

Both Frisch and coplanar designs can give depth of interaction information by the ratios of the anode to the cathode signal [63, 69], but lateral positioning is not possible. Pixel and strip electrode configurations (see Figure 1.15) however, can offer three-dimensional information. For pixelated detectors this is done either with multiple crystal elements configured in a two-dimensional plane, or a single crystal with multiple pixels. In a strip configuration, two-dimensional positioning is obtained through strips placed in orthogonal directions on the anode and cathode sides [13, 26], while depth of interaction is determined from the difference in the rise time of the anode and cathode signals.

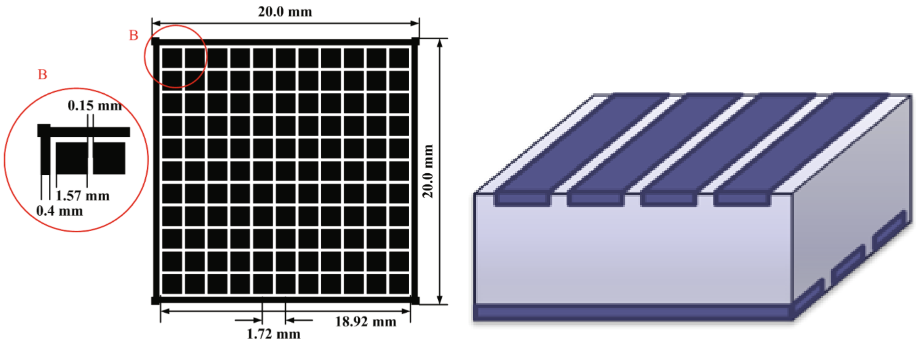

Figure 1.15: Schematic of a Pixel (Source [70]) and Strip Electrode Design.

For both pixel and strip configurations, the aspect ratio (the diameter of the pixel or width of the strip to the crystal thickness) has an effect on the signal generated within it [60, 69]. Barrett, H.H. et al. [69] showed that the signal rise in their calculated waveforms was dependant on the diameter/width of the electrode, for smaller electrodes the rise was slower, meaning that the induced signal would not generate until the charge carriers are near the vicinity of the electrode (see Figure 1.16). This is known as the ”small pixel effect”. Furthermore, Barrett described that crystals that suffer from low hole mobilities could benefit from this as long as the hole drift length was longer than the detector thickness. Eskin, J.D. et al. [60] similarly showed this effect for a variety of aspect ratios, concluding that one could essentially gain single polarity sensing, at the risk of introducing charge sharing effects between the electrodes. Thus, there is a limit to how small a pixel/strip can be before it is no longer beneficial. Eskin, J.D., et al., [60] found this ratio to be 0.25 (simulated) for pixelated CZT.

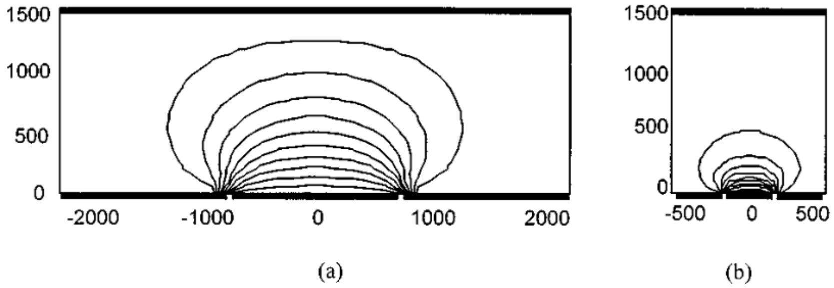

Figure 1.16: Cross Sectional View of Weighting Potential. (a) For large pixel (1:1 diameter/detector thickness) and (b) Pixel with a 1:4 ratio. Source [60].

HPGe has the advantage that it does not suffer from charge trapping, and that its electron and hole mobilities are similar (see Table 1.2). Additionally, depending on the electrode configuration, the charge induced in HPGe can be independent of interaction depth [26, 60]. In the case of our DSS HPGe detector, however, induced signals on any electrode are a superposition of both electron and hole migration [71]. This is because the electrode configuration is designed for dual-polarity sensing for both sub-strip positioning and depth of interaction estimation. Full description of the DSS HPGe detector and how the sub-strip positioning is done for this work will be presented in Chapter 2.

1.4.2 Collimators

Collimators are used to either block radiation photons of certain energies and/or constrain photons coming from particular angles. In SPECT imaging, a collimator is always used as constraining the angle of the incoming photons is essential for the image reconstruction. In astrophysics a coded mask or coded aperture (that plays a similar role to a collimator in SPECT) is sometimes used, but the choice lies in the additional weight and cost of the mask to the system. In both fields, the choice of the collimator/coded mask design depends on the signal-to-noise (SNR), or signal to background, of the object to be imaged and on the field of view needed [72].

All coded masks work on the same principle: an intentional or random design of holes on a lead alloy plate is used to cast a shadow on the detector. These masks are defined by the pattern type and their ”open fraction”, f. This is the fraction of the total area of the mask that is transparent. Knowing how the shadow pattern is designed and deconvolving the pattern from the object + mask image gives information about the location of the object [72, 73]. Coded masks can use a variety of different patterns and decoding methods [72, 73, 74].

Some of the more common coded mask families are: Fresnel Zone Plate (FZP) [72, 75], Dicke (named after Dicke, R.H. [74, 76]), Non-Redundant and Uniformly-Redundant Arrays (NRAs and URA’s respectively) [72], and Cyclic Difference Sets (CDS) [72, 73, 74]. Note that CDS’s can be used to build other variants of URA’s as well (see [77] for example).

The coded mask has not been used very frequently in nuclear imaging. The coded mask could be considered to be made up of pinholes, similar to the parallel-, single- and multi- pinhole(s) that are used in SPECT imaging. Coded masks are often limited in image quality. Some drawbacks are noise artifacts and a non-uniform image, this is due to the dependence on the thickness of the coded aperture and the opening angle of the pinhole (see section 1.3.2 and equation 1.10) which affect the diameter of the pinhole as seen by the source. This effect is called the ”collimation” effect [78] and is an effect that can occur in both astrophyics and nuclear imaging applications. The collimation effect is a combination of contrast and an ”effective pinhole diameter”. An effective pinhole diameter is when photons enter the pinhole opening at oblique angles, some will be blocked by the pinhole edges, while others might make it through the collimator to the detector, depending on the Z number and thickness of the coded mask or collimator. An ideal mask would be very thin [78], but in order to stop most of the photons a thickness of some sort is required. Without this, there would be no contrast between the light passing into the holes and the surrounding material. Because the coded aperature is used to cast a shadow on the detector, this effective pinhole diameter will cause the shadow to be displaced a particular distance, d, which is the collimation effect (see Figure 1.17).

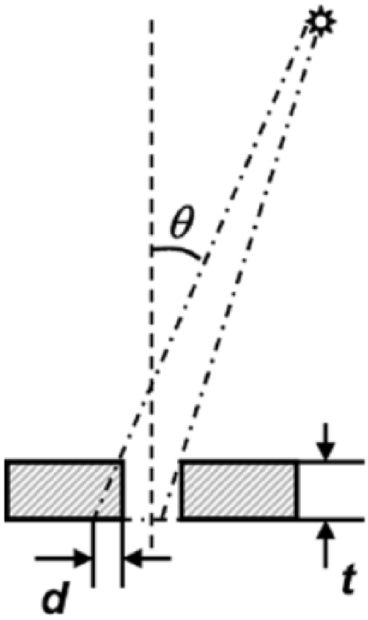

Figure 1.17: Schematic of the Effective pinhole Diameter. Schematic showing the geometry of the effective pinhole diameter cause by photons arriving from an oblique angle. *d* is the displacement of the shadow projection, *t* is the thickness of the mask or collimator. Source [78].

Not only is the shadow displaced, but the contrast within that shadow will be different, however, the thicker the mask is, the larger the displacement of the shadow (the greater the collimation effect).

In SPECT imaging applications, collimation tends to be more prominent because of the nature of the near-field imaging. For astronomy applications, the incident photons are assumed to be parallel to the coding mask since the imaging source is so far away, making the shadow of the mask the same size as the mask, thus in equation 1.10 the diameter of the pinhole is constant at any subtended angle (this is the far-field effect). In near-field imaging, there is a finite distance between the detector and the imaging object which has two effects, 1) At oblique angles, some of the photons from the source will be blocked by the pinhole edges, while others might make it through the collimator to the crystal and 2) The shadow image is magnified as a function of this distance (see equation 1.10).

Despite the complications listed above, there have been some attempts at using different masks for SPECT imaging [72, 75, 79]. Both Barrett H.H., 1972 [75] and Accorsi, R. et al., 2001 [79] showed that a coded mask would allow for a larger SNR compared to a single-pinhole collimator in specific cases. Zhiping, M. and Yi-Hwa L., 2006 [78] showed that a coded mask receives more counts than an parallel-hole collimator in their phantom studies using a combination of deconvolving and maximum likelihood estimation (a reconstruction technique that will be discussed in section 1.4.4). The potential advantage of using coded masks in place of parallel-, single-, and multi-pinhole(s) would be in imaging specific organs in children or in small-animal studies where the coded mask could lower the imaging time or the dose to the patient/small-animal [78, 79]. The limitations of these studies were that they were successful only in: small imaging targets (thyroid, Barrett [75]), in cases where the FOV is only a fraction of the detector plane (Accorsi [79], and only applied to planar projections (no three-dimensional image reconstruction done (Zhiping and Yi-Hwa [78]). Figure 1.18 shows all three collimators (coded mask, parallel- and single-hole(s)).

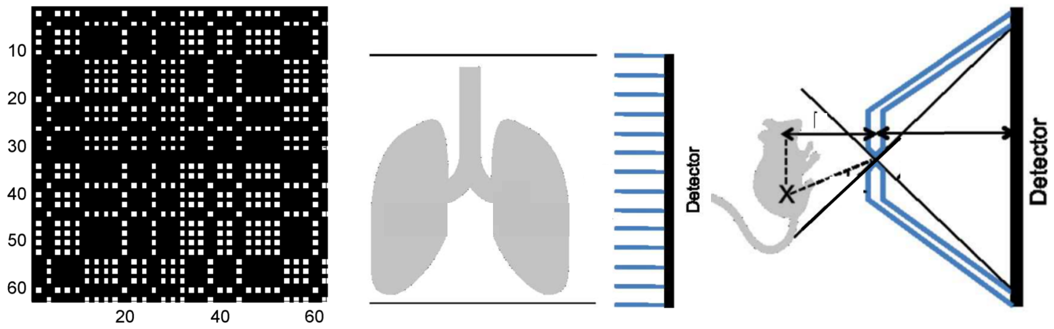

Figure 1.18: Schematic Depicting a Coded Mask (left, source [79]), Parallel-Hole Collimator (center), and a Single pinhole Collimator (right) Source [80].

The single-pinhole camera (see section 1.3.2) is one type of collimator that can be used in SPECT imaging. Other collimators are parallel-hole, converging- and diverging-, and multi-pinhole [80]. Parallel-holes, single- and multi- pinhole(s) are typically used in small-animal SPECT imaging. Parallel-hole collimators are made out of dense material (usually tungsten or lead) containing highly packed parallel hexagonal holes separated by walls, these separations are called ”septa”. Different collimators are defined by their septa thickness, pitch and length, along with the hole diameter and attenuation. Figure 1.19 depicts some of these parameters.

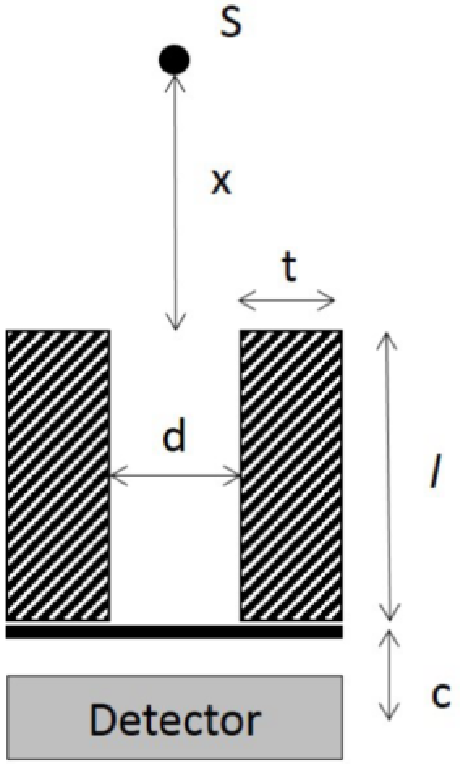

Figure 1.19: Schematic Cross-section for the Geometry of a Parallel-Hole Collimator. **d** is the septa separation, **x** is the distance from the imaging object (S) to the collimator, **t** is the septa thickness, **l** is the septa length, and **c** is the distance from the collimator. Note, schematic depicts the geometry of one pinhole of the mutli-pinhole collimator. Source [81].

Converging and diverging collimators are collimators that converge the image towards or away from a focal line respectively, allowing another way to enlarge the FOV that does not involve changing the radius of rotation of the system. A converging collimator can be used to magnify the image of a region of interest on an object onto a detector (say a single organ in a mouse) while increasing/maintaining spatial resolution [80]. Diverging collimators are used when viewing multiple parts of an object at once (such as the heart and an organ of interest of a mouse in a single bed position) within the same FOV, with the tradeoff of losing some spatial resolution [80].

The single-pinhole collimator was described in sec 1.3.2. Closely related to the single-pinhole is the multi-pinhole collimator. The advantage of having more than one pinhole is the increase in sensitivity, along with multiple images of the object. The trade-off here is in the loss of information in the overlapping views of the pinholes, called multiplexing, which can also cause artifacts in the reconstructed images if there is insufficient sampling [14, 80]. Today however, some multi-pinhole systems are designed in such a way as to avoid this overlap [82, 83].

Lastly, there is another type of collimation that does not involve the use of a physical mask or collimators mentioned above, and that is electronic collimation. This is a method that uses events that coincide across two or more detectors. The traditional ”double Compton” process was first described independently by Schonfelder, V., et al. [84] for an astrophysics application and by Todd, R.W., et al. [85] for medical imaging. Electronic collimation is done using a stack of two or more position-sensitive detectors, when an incident gamma-ray Compton scatters within the first detector and gets absorbed in the second (or one of the subsequent detectors if more than two) the direction of the incident photon can then be calculated from the Compton equation, in the case of two planar detectors [1]:

$$cos(\theta) = 1 + M_o * c^2 * \left[\frac{1}{E_o} - \frac{1}{E_2} \right], \tag{1.15}$$

where $\mathbf{E_o}$ is the sum of the energy across both detectors ($\mathbf{E_1}$ and $\mathbf{E_2}$ in Figure 1.20 and θ is the angle between the incident and scattered gamma-ray. The direction of the incident photon then lies in the cone formed by the line along the direction of the scattered gamma-ray and the angle θ. Figure 1.20 shows an example of this process with two detectors. Many studies and detector systems have been made using this concept with variations on the two (or more) detector types, and configurations: astrophysics [85, 86, 87], bio-medical imaging (SPECT and PET) [84, 88, 89, 90], and nuclear sites/homeland security [91, 92] for example.

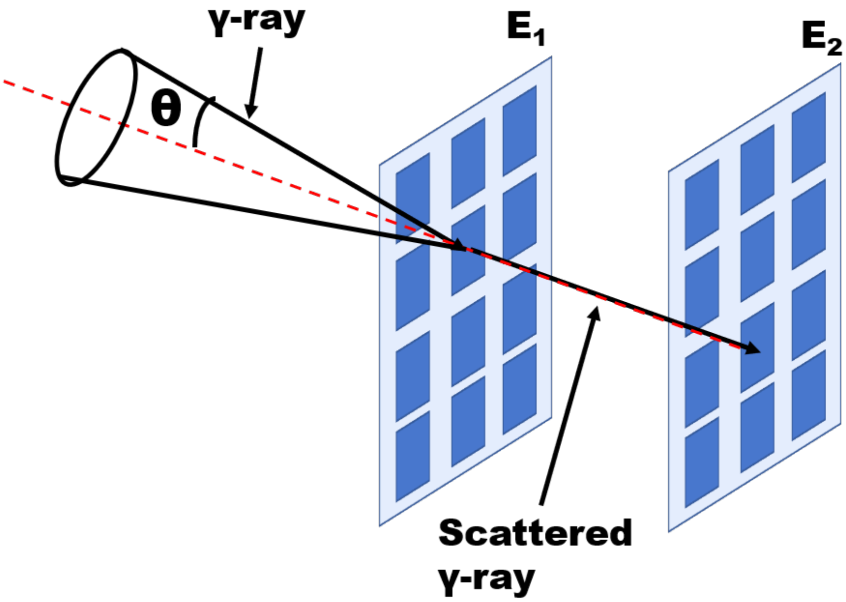

Figure 1.20: Schematic of a Conic Projection from a Compton Scattering Event. $\mathbf{E_1}$ and $\mathbf{E_2}$ are the initial and scattered photon energies deposited into the detector. Adapted from [1].

Compton cameras are most useful when the imaging involves such high energy gamma-rays that using collimators or coded masks are no longer feasible [88, 93]. They also provide a wide FOV [94], and accept a larger fraction of emitted photons [94] (compared to pinhole or parallel hole collimators). Compton cameras are limited by the scatter angle θ if the incoming photon enters in such a way that it does not end up within a subsequent detector. The angular resolution of these detectors are limited to the energy and spatial resolution of the detector system.

The combination of the collimator, system geometry, and intrinsic energy resolution of the detector affects the total spatial resolution of the imaging system. This further leads to effects on the reconstructed image spatial resolution; thus, while the previous parameters seem different, they are not entirely independent. The desired reconstructed image resolution sets a requirement on the intrinsic resolution of the detector which will dictate the collimator design and geometry of the system. How these can affect the image quality is discussed in the next section.

1.4.3 Detector Properties that Affect Image Quality

The key properties that one needs to consider when designing a imaging detector are: efficiency, spatial and energy resolution, uniformity (especially for SPECT imaging), and cost per unit of space-bandwidth product. The following paragraphs will describe each of these properties individually.

Efficiency is defined in two terms, absolute and intrinsic; and then further categorized by two event types, total and peak. Absolute efficiency is:

$$\frac{Number\ of\ counts}{the\ number\ of\ radiation\ photons\ emitted\ by\ the\ source}$$

and is dependant on the system geometry [5]. This includes the geometric resolution with the collimator discussed above, but also the solid angle subtended from the detector to the source. Intrinsic efficiency:

$$\frac{Number\ of\ counts}{Number\ of\ radiation\ photons\ incident\ on\ the\ detector}$$

and is not dependent on the system geometry [5]. Intrinsic efficiencies are easier to calculate, and the majority of detector manufacturers will define a detectors efficiency in terms of its intrinsic efficiency.

The event types, total and peak efficiencies, are what types of counts are chosen from the energy spectrum of the detector. Total efficiency means that all interactions are counted, whereas peak efficiency only includes interactions that fully deposit their energy into the detector [5]. These two efficiencies are related by their ratio, termed, ”peak-to-total ratio”. Generally, it is better to describe the performance in terms of peak efficiency since these are interactions that are not influenced by the surrounding environment (scattering off of materials such as shielding or other material parts) or noise fluctuations caused during long operating times[5]. Thus, one may describe the ”intrinsic peak efficiency” of a detector.

Spatial and energy resolution have been discussed in 1.3.2 in terms of intrinsic energy resolution, geometric spatial resolution, and sensitivity. The influence of these parameters can also translate to the reconstructed image. As mentioned earlier, scatter rejection, and multi-isotope imaging is possible with detectors of high energy resolution; but having the improved scatter rejection ability also improves the contrast of an image. It will also reduce contamination in a multi-isotope image by rejecting the low energy photon scatters of a higher energy isotope [13]. Any affect on the contrast of the image is important as that changes the relationship between the image intensity and activity concentration in the imaging object [95].

The geometric spatial resolution, a function of the intrinsic detector resolution and the geometry between the detector, collimator and imaging object was discussed in 1.3.2. The geometry of the whole imaging system is also important. Alignment of the detector center with the center of rotation (COR) of the system is needed to prevent blurred images [95]. Furthermore, the system needs to allow sufficient angular and axial sampling (depending on the collimator type [80]) to prevent artifacts and aliasing.

Uniformity of a detector describes how much the energy and spatial resolution and efficiency vary with the position of the photon interaction within the detector [13]. Ideally, there should be little variation of these properties with the interaction location. No detector will be 100% uniform, thus corrections such as normalizing with a flood image are typically done [13, 95]. This requires that the nonuniformity be known (via the flood image), but also that the nonuniformity is stable over long lengths of time [13].

Lastly, the number of measurements that the detector can make and its physical size are important to consider. Equations 1.9 and 1.10 showed that one could increase the total resolution of the detector+collimator system by decreasing the pinhole diameter, at the cost of reducing the pinhole sensitivity. However, this can be offset by using detectors with better intrinsic spatial resolution [56, 96]. A detector with poor resolution has to be placed further away so that the magnification (and thus spatial resolution) of the image is increased, and if multiplexing is to be avoided, only a few pinholes can be used. However, with higher spatial resolution, less magnification is needed so the detector can be placed closer to the pinhole. The diameter of the pinholes must be decreased in order to keep the same spatial resolution, which decreases the sensitivity; yet, because the magnification is smaller, this allows for more pinholes to be placed (without overlapping), which increases the sensitivity. [96]

What the above means for an imaging detector is that a large but poor/low resolution detector can obtain the same FOV and spatial resolution at a large magnification as a smaller detector with high resolution at a smaller magnification [56]. What is important between the two (in addition to sensitivity) is the number of measurements that the detector can make, i.e. can the detector area accomodate a large enough FOV to include the whole imaging object (or a target of interest). Using the detector PSF, the number of measurements that a detector can make is quantified by the ”space-bandwidth product” [56]:

$$Sp-BW = \frac{Area\ of\ Detector}{Area\ of\ PSF} = \frac{Area\ of\ Detector}{2D\ Bandwidth} \tag{1.16}$$

In applications where size or weight constraints are a concern, the space-bandwidth product shows that a detector with high intrinsic spatial resolution will fit the imaging object in a smaller area than one with a lower energy resolution, possibly lowering the cost of the system.

Detector properties are not the only thing that can affect the reconstructed image; the reconstruction algorithm itself also has affects on the spatial resolution, image quality, and additionally, the computation time.

1.4.4 Image Reconstruction Algorithms

The main goal in SPECT imaging is to estimate *in vivo*, the bio-distribution of an injected radiotracer based on projections taken by the rotating gamma-camera. The estimate will be the result of the most probable solution from the projections. Generally, the idea is to solve the following linear equation:

$$\mathbf{g} = H\boldsymbol{f} + \mathbf{n} \tag{1.17}$$

This is called the ”imaging equation” or the ”forward” equation. $\mathbf{g}$ is the resulting projection image, H is the ”system matrix”, it can account for the scatter and attenuation within the imaging object, system geometry, collimator, and projection angle [97]. $\boldsymbol{f}$ is the distribution of photons emitted from the imaging object, and $\mathbf{n}$ is the noise. H is the model containing the underlying physics for each projection angle that will result in a matrix that maps the object activity distribution to the detector.

$\boldsymbol{f}$ is voxelized [97] (the imaging object is divided into a number of image pixels) which allows for an approximation of the imaging equation. The solution to the imaging equation is done computationally and is time consuming, however, various algorithms have been developed to solve equation 1.17. These solutions are mostly divided into two types: backprojection and iterative [97].

Backprojection is the first, and most well known algorithm. It is based off of the Radon transform [98] developed in 1917. It was then applied later to computed tomography [99] and astronomy [100]. The Radon transform shows that a two-dimensional imaging object can be reconstructed from multiple (line) integral measurements through that object [97].

Advantages in using FBP is that the backprojection part is done only once and is fast. While other iterative algorithms tend to do both a forward and a backprojection (this will be described in the next method). The main disadvantage of FBP is that it does not allow for reconstruction of complex objects as no information about the imaging system is used. Iterative algorithms on the other hand, allow for more complexities such as detector and collimator blur and Compton scattering through the system matrix. Generally, the iterative algorithm is a method that allows for the first estimate of the image to be updated/improved.

There are multiple iterative reconstruction algorithms such as the Algebraic Reconstruction Technique (ART) [101], Maximum A *Posteriori* (MAP) [102], Maximum A *Posteriori* Expectation Maximization (MAP-EM) [103], and List-Mode Maximum Likelihood (LMML) [104] to name a few. Here I will only talk about two others; Maximum Likelihood Expectation Maximization (ML-EM) [105] and an accelerated EM method, Ordered Subset Expectation Maximization (OSEM) [106].

Returning to the imaging equation 1.17 above, it can be re-written as:

$$\hat{g}_i^k = \sum_l h_{i,l} \hat{f}_l^k \tag{1.18}$$

$\hat{g}_i^k$ is the current estimate of the projection data at the kth iteration [97]. l represents the number of all imaging pixels, i is the detector element, h$_{i,l}$ is the matrix element of h (the probability that a photon emitted from imaging pixel l was detected in detector element i). This is the EM part of ML-EM and it is a sum over all the quantities, i.e., all image pixels and detector elements [10].

The ML portion gives the next iteration [10, 97]:

$$\hat{f}^{(k+1)} = \frac{\hat{f}_j^k}{\sum h_{i,j}} \sum_i h_{i,j} \frac{g_i}{\hat{g}_i^k} \tag{1.19}$$

Here $\hat{f}^{(k+1)}$ is the new estimated image, g_i is the true projection data (the result from the measurement), and $h_{i,j}$ and $\hat{f}_j^k$ are the same as $h_{i,l}$ and $\hat{f}_l^k$ in 1.18. However, l is summed over before j; so $\hat{g}_i^k$ in equation 1.19 is summed over first.

Thus, the k*th* estimate of the projected data, $\hat{g}_i^k$ is determined by projecting the k*th* image estimate, $\hat{f}_l^k$, through *H*. It is then compared to the true projected data, g_i, by division, and lastly, backprojecting that difference through *H* to update the next image estimation, $\hat{f}^{(k+1)}$ [97].

As stated earlier, *H* is a large matrix, and with forward and backward projections to perform in equation 1.19, the ML-EM method is computationally expensive. One method for speeding this up is OSEM, which uses subsets of the projection data to update $\hat{f}$ and then proceeds to use the next subset for the next update. It has been shown that using fewer projection angles in the initial iterations results in the algorithm converging faster as more projections are added [107]. The ordering of the subsets is done so that the projections are spaced in such a way that it adds new information to the algorithm, keeping in mind that each subset should also have equivalent number of counts [106].

The accuracy of these algorithms will depend on the information contained in *H*. This can be done in multiple approaches [10, 14], the first is measuring the system exhaustively, obtaining system data for every voxel at every projection angle. This is computationally expensive in both time and storage space. Another method is to develop a mathematical model with the necessary geometrical figures. Geometrical figures are parameters like COR, rotation angles of each detector, alignment of the detectors with the COR and each other; see Johnson, L., 2013 [14] for a description on geometrical calibration. The last method is similar to the mathematical model, but done with simulation instead; see Campbell, D.L. and Peterson T.E., 2014 [108] as an example.

In order to properly map the position of the incoming photon from object space to detector space, the positioning of the events in the detector itself needs to be accurate. In other words, we need the system matrix for the detector, the response of the detector to an event at each position within the detector. This is explained in more detail in Chapter 2 with respect to our DSS HPGe detector.

In the next chapters that follow I will describe the SPECT system and the DSS HPGe detector used. Current system processing and ML will both be described for the event positioning, as well as a description on how the measurements where done to obtain the system matrix. Chapter 3 will discuss the results from using ML and its implication for further use in other strip detectors for both SPECT and astro-imaging.

Chapter 2

The HPGe Small-Animal SPECT System

2.1 HPGe Detector Description

2.1.1 Description of Detector and Detector System

The DSS HPGe detector used in this study is 90 mm in diameter, 1 cm thick, and has 16 x 16 orthogonal strips. The strip widths are 4.75 mm with 0.25 mm gaps between strips. See Figure 2.1.

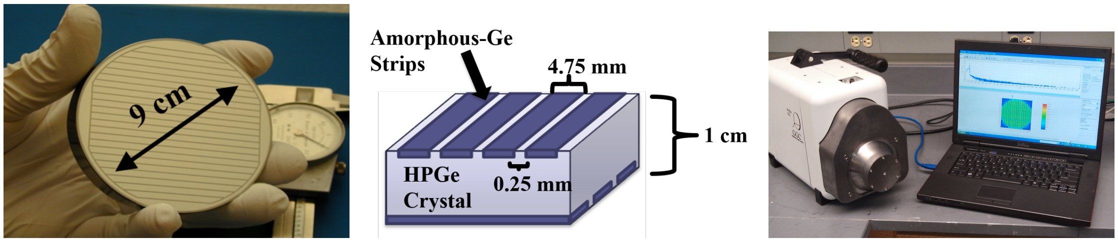

Figure 2.1: HPGe Crystal Geometry. Left: Actual crystal, dark lines are the gaps inbetween the strips. Middle: Schematic representing the dimensions of the electrode strip geometry (shown as a square for convenience). Right: HPGe Detector with pinhole collimator and laptop displaying Imager32 software.

The cross-strip configuration allows for sub-pixel positioning (explained in the next section). The detector operates at -700 V and at a temperature of 83 K. It is mechanically cooled, which makes the system easily portable. The detector system, including the electronics was created by PHDS Co. in Knoxville, TN [109].

The detector output is instrumented by SPECT32 (also designed by PHDS), which is designed to allow for real-time event processing. For this work, we used Imager32 software (also developed by PhDs Co.) to write the data output to a separate file for offline processing. This is a feature provided within the Imager32 software using c-pipe commands, which is paired with MATLAB for organization and storage of the data files. MATLAB is also used for the offline processing.

SPECT32 houses all of the electronics for the digital processing. SPECT32 consists of four electronic boards, each with eight BNC connecters (for a total of 32 input signals), eight 12-bit 50 MHz Analog-to-Digital Converters (ADC's), and a Field Programmable Gate Array (FPGA) for data processing. Lastly, an additional FPGA is used to communicate to the four boards and output data to the computer via a USB connection. Clock timing between the boards is 50 MHz, or about 20 ns per clock tick (every sampled point of the detector signal is taken at a clock tick). [110]

Each FPGA on each of the four electronic boards implements digitally a fast and slow filter. The fast filter is used for the neighboring strips to calculate lateral positioning while the slow filter is used for determining the energy deposited from the event (see section 2.1.2).

Lastly, depth of interaction is calculated from the difference in arrival times of the fast signals (i.e. difference of the clock ticks) between the two sides of the detector. Knowing the velocity of the electron/holes along with the applied voltage and clock speed gives $\approx$1 mm distance between depths.

2.1.2 Signal Creation in the DSS HPGe Detector

HPGe is a semiconductor and therefore signal generation is done by charge induction due to migrating charge carriers as discussed in Chapter 1, sec 1.4.1. Sub-pixel positioning however, can become complicated due to: Charge sharing and charge loss both near the strip and in the gaps between the strips, along with multi-strip events [71, 110, 111]. These event types are depicted in Figure 2.2 for the DSS HPGe used in this study.

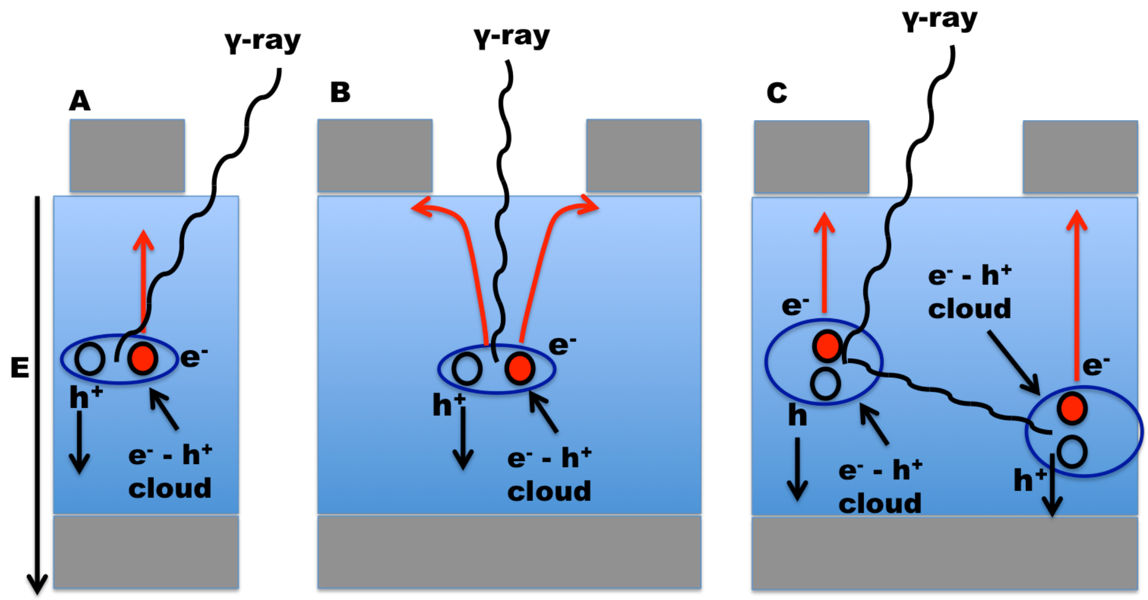

Figure 2.2: Common Events in DDS HPGe Detector. A: Two-strip event, B and C: Two different three-strip events resulting in charge sharing; C is from Compton Scattering.

(A) in Figure 2.2 represents what we call a ”two-strip” event; when one strip on each of the detector’s side collects charge. (B) and (C) both represent ”three-strip” events that result in charge sharing (and potentially, charge loss). (B) is a true charge sharing event, where a gamma-ray interaction does occur between two strips, while (C) is a result of Compton scattering. In the current processing (the processing done in real time by SPECT32), (B) and (C) events are indistinguishable. The reason for this will become clear when the sub-pixel process is explained in detail. Because they are indistinguishable, we choose to not use these events as their origin will not be accurately known. For this reason, only two-strip events are used. This decreases our sensitivity, and also causes gaps in the resulting image (as the three-strip events are not being used to fill them in). The effect that this has on the reconstructed SPECT images will be addressed shortly, after the sub-pixel positioning is explained.

The sub-strip positioning is done using what is termed the ”collecting” strip and the ”transient” strips (also known as the ”spectator” or ”neighboring” strips). In Figure 2.3

(left) the center strip is the collecting strip and the transient strips are the predecessor (Pred) and successor (Succ) strips. The center strip is the strip that collects the charge, and when the signal is integrated over a long time, will result in an amplitude proportional to the energy that was deposited (see Chapter 1 section 1.4.1). The Pred and Succ strips however, if integrated over the same time period will result to zero. This is because the signal induced on these neighboring strips are due to charge carriers only spending a portion of their time in the weighting potential (see 1.4.1) of that neighboring strip before moving off to the charge collecting strip (thus moving out of the weighting potential causes the signal induction to decrease). The bipolar shape of these signals and their dependence on depth and lateral position is illustrated in Hayward, J. and Wehe, D., 2007 [71] for a DSS HPGe detector, shown here in Figure 2.3 (right).

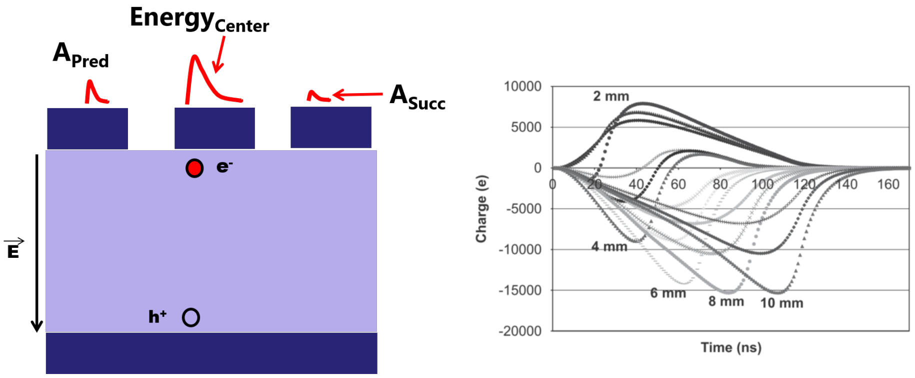

Figure 2.3: Charge Induction in a DSS HPGe Detector. Left: As charges migrate to their respective electrodes, charge is induced on the strips. The strip with the largest charge will be the strip where the event occurred, and sub-pixel positioning is done using the predecessor and successor strips (see text). Right: Simulated induced signals on transient strips at different crystal depths and lateral positions from [71].

When the fast signals are integrated over a short time period, the resulting amplitude will correspond to the portions of the induced charge with the fastest time characteristics [5]. The triggering of the signal, better stated, when the induced signal reaches a chosen threshold, is done using the fast signal. In our detector system, the triggering is done when the signal is above $\approx$ 18 keV. Our system also uses a 50% constant fraction rise-time, the clock tick at which the signal amplitude reaches 50% of its maximum amplitude, to determine the depth of interaction described earlier.

Vetter, K. et al., 2004 [112] showed that sub-strip positing using the fast signal amplitudes could be done by:

$$X_{pos} \propto \frac{A_{Pred} - A_{Succ}}{A_{Pred} + A_{Succ}} \tag{2.1}$$

for the x-position. Where Pred and Succ are the predecessor and successor of the center strip, and C is the center strip. A is the maximum amplitude of the signal. A similar equation is used for y positioning.

Likewise, in the Imager32 software:

$$X_{pos\,ratio} \propto \frac{\int (Pred)^2 - \int (Succ)^2}{E_{center}} \tag{2.2}$$

where $\int (Pred)^2$ and $\int (Succ)^2$ are the squared sums of the Pred and Succ fast signals and E_{center} is the amplitude of the slow signal from the collecting strip. As with equation 2.1, this can be done on the opposite detector side for the Y position. We call the value from equation 2.1.2 ”position ratios” and they are used in determining the boundaries of the sub-pixels.

The process to determine sub-pixel boundaries with the position ratios involves using a flood image of the detector. From this flood image the distribution of position ratios for each strip is histogrammed. This histogram is then divided into 9 bins (the 10^{th} bin corresponds to the gap in between the strips) of equal counts (with the assumption that the whole strip collects charge uniformly). The number of bins is chosen for convenience, as the strip pitch is 5 mm, 4.75 mm for the strip and 0.25 mm for the gap, thus each sub-pixel is ≈0.53 mm. Each digital pixel (a location where the x and y strips cross, alternatively a cross-strip) contains 9 sub-pixels. See Figure 2.4.

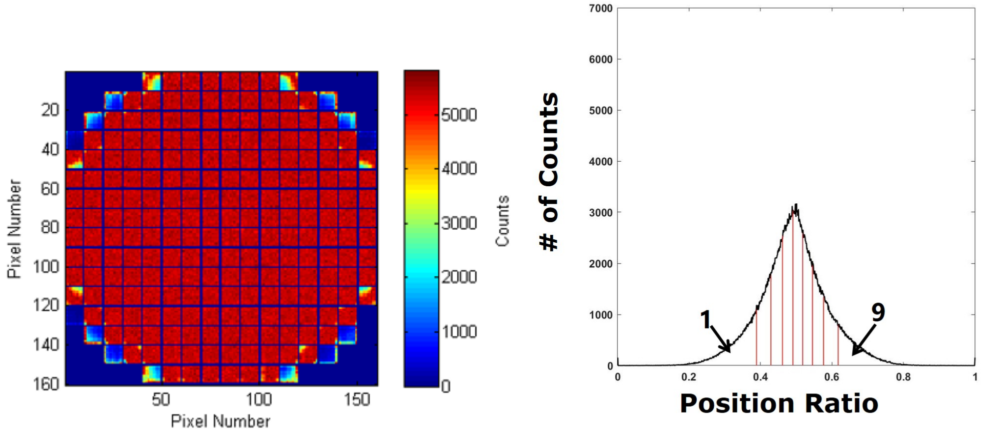

Figure 2.4: Sub-pixel Positioning in DSS HPGe. Left: Flood image of DSS HPGe detector with a ^{57}Co source. Right: Schematic showing the sub-pixel boundaries created from the position ratios.

Look-up tables are then created from this flood image listing the position ratio boundaries for these sub-pixels for each digital pixel, at each depth. When an event occurs, the position ratio is calculated, and a search within the proper table list by depth and cross-strip is done to identify the pixel assignment of the event. The subsection, Image Artifacts, will discuss results from the first prototype of the small-animal SPECT system which used a DSS HPGe detector with the same crystal and electrode geometry.

2.1.3 Imager32 Data Output Options

Two different data types can be obtained separately or simultaneously from Imager32: list mode and raw mode. List mode outputs the 3-D positions and the energy for each event. Raw mode outputs the squared sum of the fast signals and amplitude of the slow signal for the transient strips and the collecting strip, respectively, and the clock time for each. With raw mode, more information is given from the event and this is what is used for the detector response measurement and subsequent data analysis.

2.2 Image Artifacts

Previous work done by Johnson, L. [14] showed that the gaps in between the strips resulted in a ”checkerboard” pattern in reconstructed SPECT images of a NEMA phantom (see Figure 2.5) that could not be resolved using interpolation.

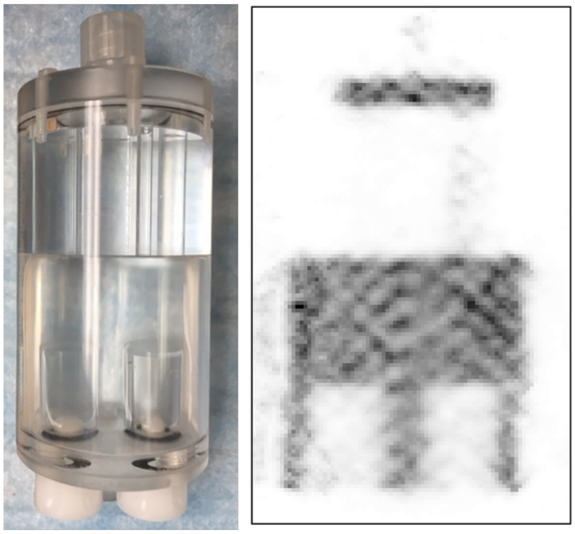

Figure 2.5: SPECT Image Slice of NEMA Phantom. Left: NEMA Phantom used for SPECT Imaging, filled with diluted ^{99m}Tc. Right: Reconstructed SPECT image slice of NEMA Phantom.

Johnson hypothesized that the distortion could be from the positioning method. The difference term in the numerator of the position ratio does not allow for charge sharing, and is instead, a ”winner take all scenario”. This charge sharing is what would occur between the collecting strip and its predecessor or its successor in a two-strip event. Herein lies the motivation for this study, to investigate the spatial response of the detector in detail so that a positioning scheme could be developed to eliminate or reduce these artifacts.

2.3 Geometrical Analysis and Advanced Signal Processing

2.3.1 Geometrical Analysis

To investigate the spatial response of the detector, we scanned a ≈1 mm collimated ^{99m}Tc source across the front surface. The detector used in this measurement is one of PHDS Co. MI4 generation detectors (see [14, 32, 33, 113]).

A capillary with ≈ 1.69 mCi of ^{99m}Tc was inserted into the collimator which was then mounted onto a three-dimensional translational stage system using two Velmex motion control systems. The stages had resolutions of 2,5x10^{-3} mm/step and 6.35x10^{-3} mm/step. The collimator was positioned to irradiate the center of one strip, moved across two strips, and stopped in the center of the next strip in steps of 0.044 mm (300 steps total) in both the horizontal and vertical directions. Figure 2.6 shows the set up and the resulting (summed over all 10 depths and steps) images.

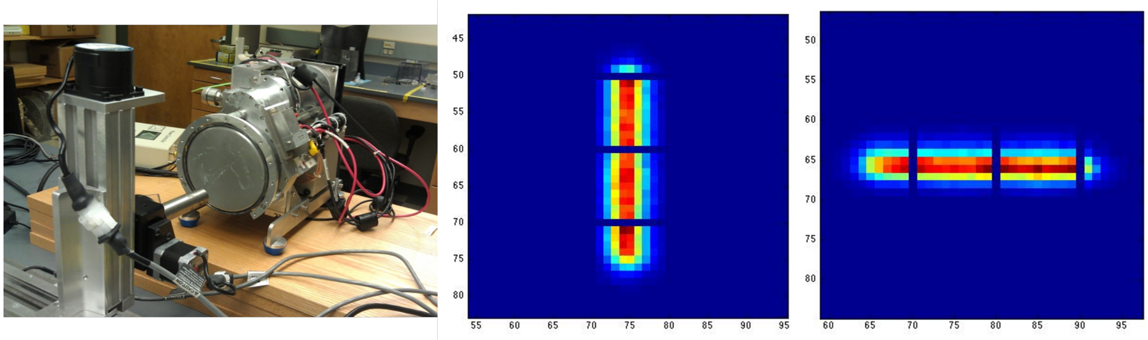

Figure 2.6: DSS HPGe Detector Response Measurement. Left: Detector system and collimator set-up on three-dimensional stage. Middle: Two-dimensional summed image of all 300 acquisitions stepping across the detector vertically (middle) and horizontally (right).

Due to the beam being wider than the gap width, we developed a model to estimate the number of events that would occur in the gap as a function of position. Figure 2.7 shows a schematic where a portion of the beam falls over the gap region.

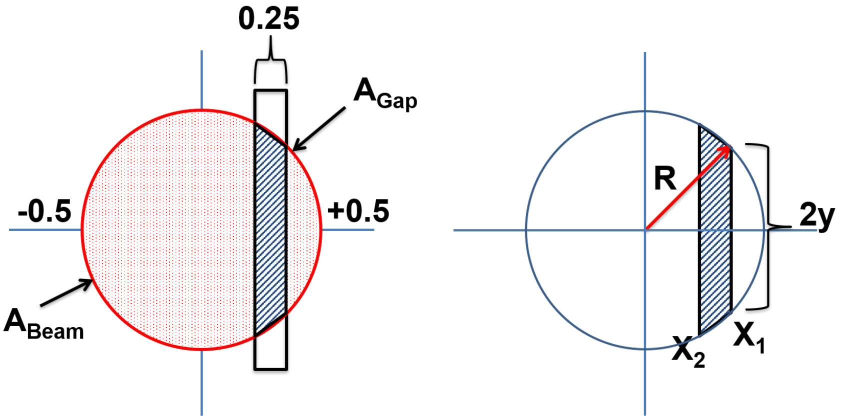

Figure 2.7: Beam Geometry. Left: Schematic showing the fraction of events expected to fall within a strip under a radiation beam. A_{Beam} and A_{Gap} are the areas of the beam and gap. Right: Integration parameters for the area of the gap, related to equations 2.5 and 2.6. R represents the radius where one of the gap edges intersects the circle, X_1 and X_2 are the gap edges, and $2y$ is the length of the gap within the circle.

The fraction of events expected in the strip is just the beam area minus the gap area, divided by the beam area:

$$F_{events} = \frac{A_{Beam} - A_{Gap}}{A_{Beam}} \tag{2.3}$$

Where the area of the gap is calculated via the line integral using the radius (see Figure 2.7:

$$R^2 = x^2 + y^2 \rightarrow y = \sqrt{R^2 - x^2} \tag{2.4}$$

Because the total length of the gap is 2y, the area of the gap becomes:

$$\int_{x_1}^{x_2} 2y\, dx = \int_{x_1}^{x_2} 2\sqrt{R^2 - x^2}\, dx \tag{2.5}$$

Lastly, using the following result from an integration table:

$$\int \sqrt{a^2 - u^2}\, du = \frac{u}{2}\sqrt{a^2 - u^2} - \frac{a^2}{2}\sin^{-1}\left(\frac{u}{a}\right) \tag{2.6}$$

The area of the gap is:

$$A_{Gap} = 2\left[\frac{x}{2}\sqrt{R^2 - x^2} + \frac{R^2}{2}\sin^{-1}\left(\frac{x}{R}\right)\right]_{x_1}^{x_2} \tag{2.7}$$

A$_{Gap}$ is then used in equation 2.3, which is multiplied by the average number of events within the strips taken from the data (with the assumption that the strip collects charge uniformly over the whole strip width). This was done for different gap widths (from 0.25 mm to 0.75 mm), see Figure 2.8.

Figure 2.9 shows the results for the full data set (both vertical and horizontal scans) for the physical gap width (left) and the effective gap width (right).

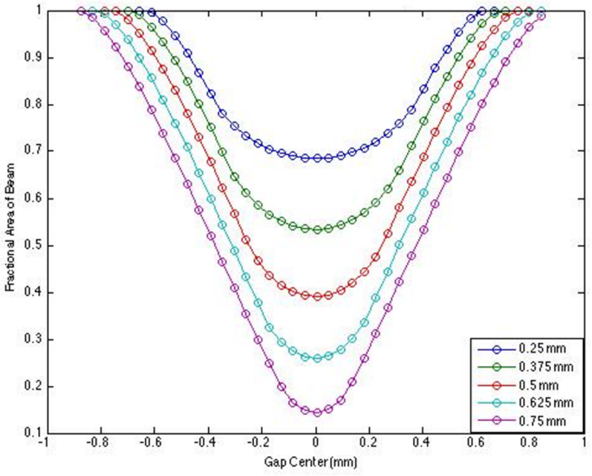

Figure 2.8: Geometric Model Results with Different Gap Widths. Fractional area of beam as a function of gap width for widths of 0.25 mm (physical gap width) to 0.75 mm.

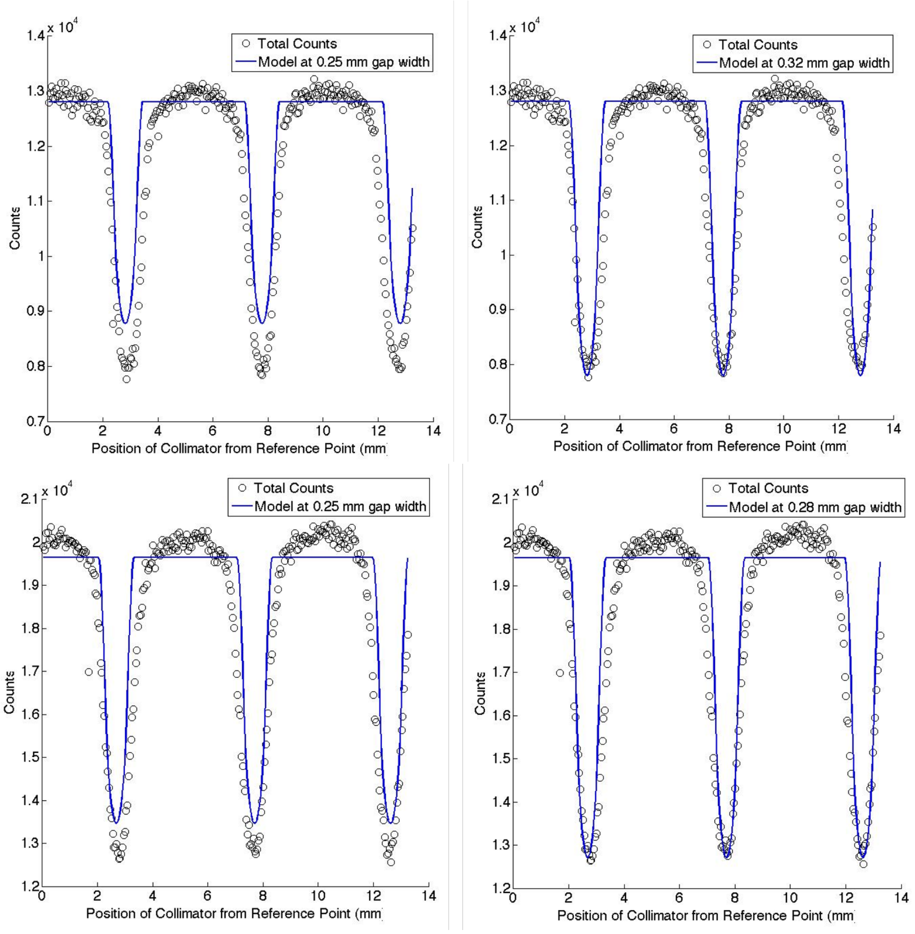

Figure 2.9: Geometrical Model vs. Data. Plots compare data to the model at the physical gap width (left) of 0.25mm and the best fit gap width (right) for the horizontal (top) and vertical (bottom) data points.

The best fit to the model was a gap width of 0.32 mm for the x-direction and 0.28 mm for the y-direction, This shows that as the beam nears the edge of a strip, the response of the strip is affected by an ”effective” gap width that extends beyond the physical gap width, see Figure 2.8 right plot. This could be due to the size and diffusion of the charge cloud as it travels from the site of interaction to the electrode causing charge loss or charge sharing between the strips [111].

The model does over estimate the data, and does not match the ”roll off” of the strip edge, for both the physical and effective gap widths. Some reasons for this could be that the effective width changes with the depth of interaction of the event and divergence of the radiation beam.

To see if charge loss was a factor in our measurements, we looked at the energy distribution of a 3-strip event, between the charge sharing strips and the single strip on the opposite side. Figure 2.10 depicts this when the beam falls across two strips. The left plot shows the shared strip energies plotted against one another, while the right shows the histogram of the energies of the (summed) shared strips (blue), for 3-strip and the 2-strip events (red). Plots include events within a 140-keV +/- 3 keV window for a single strip, and a +/- 6 keV window for the 2-strip event. Both plots show a slight energy loss, the right specifically of a few keV; however no events are lost outside of our windows. The left plot also shows that there are no events that fall below the ≈ 18 keV trigger threshold.

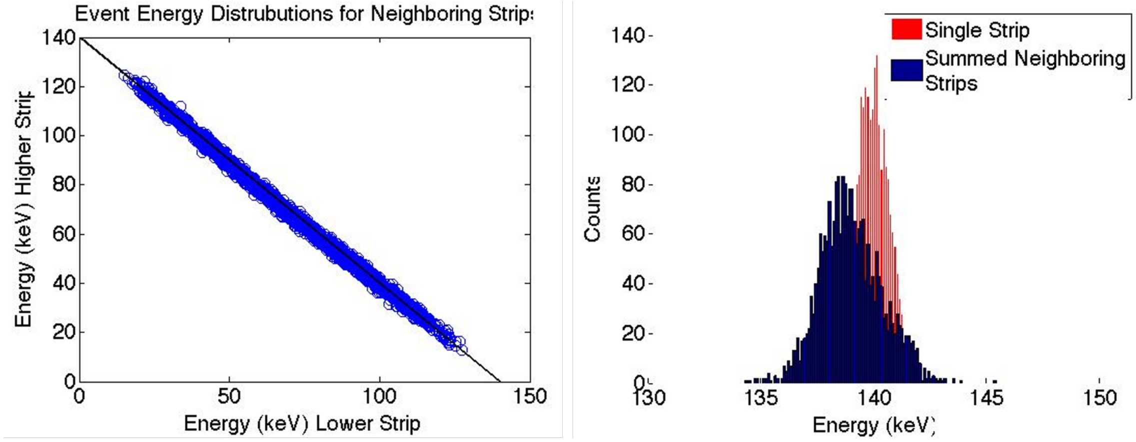

Figure 2.10: Energy Distribution of Gap Events. Left: Energy distribution for events between two neighboring strips. Right: the energies of both strips summed (dark blue histogram) vs. the energy of the single strip (red).

Figure 2.11 shows the total summed counts (over all depths) vs. distance travelled across two strips including a gap region. The black circles represent the 2-strip events, while the blue squares represent the 3-strip events. As the beam approaches the strip edge, the 2-strip counts begin to decrease (as shown in Figures 2.8 and 2.9) before the physical gap width (represented by the two red lines) is reached. The decrease in 2-strip events is not compensated by the increase in 3-strip events, nor do the 2-strip events decrease to zero in the gap. These differences in the 2-strip and 3-strip events are due to charge sharing events in which one of the strips does not collect enough charge to trigger (below the 18 keV threshold). It is also important to note that while the beam is located in the center of the strip, 3-strip events still occur, meaning that Compton events are possible even when in the center of a strip. Both of these could result in a mis-positioning or loss of an event using the positioning ratio method discussed earlier. While we typically exclude 3-strip events it is possible for a Compton scatter that ends up underneath one of the strips could be counted for a 2-strip event.

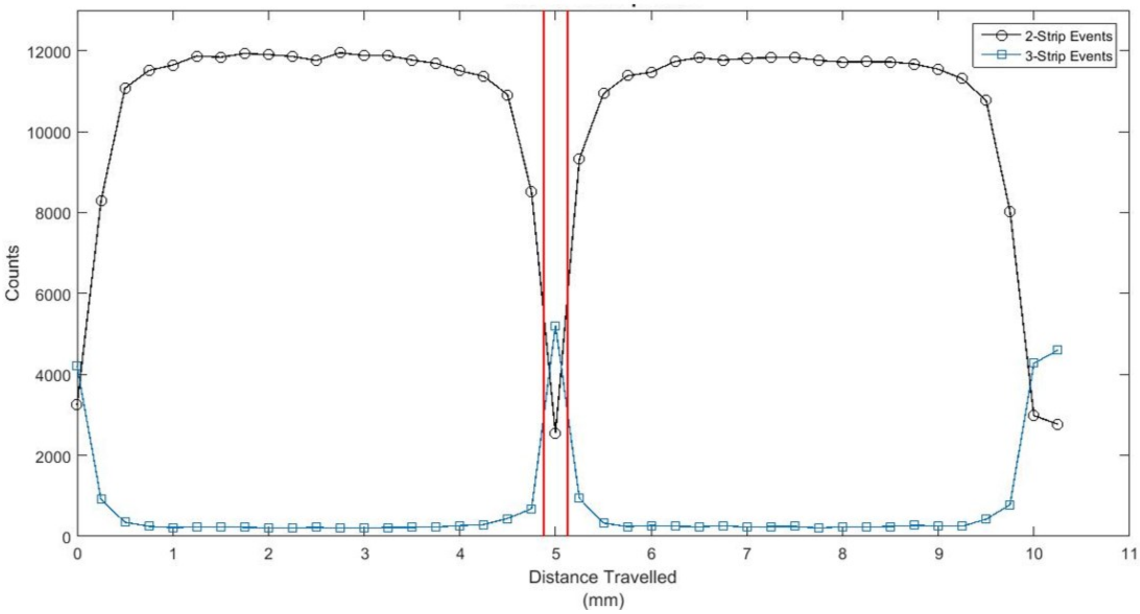

Figure 2.11: Summed Counts (Over all Depths) vs. Distance. Total counts (summed over all depths) vs. distanced travelled across two strips including the gap region. Black circles represent the 2-strip events and blue squares represent the 3-strip events. The red lines represent the physical gap width.

The result of an effective gap width greater than the physical gap width shows that the assumption of the strip electrodes collecting charge uniformly out to the strip edge is incorrect. It is possible that this could be causing the distortions seen in Figure 2.5. However, the diameter of the beam in this measurement was much larger than the gap width, so a more thorough investigation of the gap region was needed with a beam of a smaller diameter, which was the motivation for using the x-ray beam at the Advanced Photon Source (APS) located at the Argonne National Laboratory.

2.3.2 Advanced Signal Processing: Maximum Likelihood

In chapter one, section 1.4.4, it was stated that in order to obtain a correct system matrix for image reconstruction, the position estimation needs to be accurate. In a similar fashion to solving the imaging equation, the position estimation can be solved via the linear equation:

$$\overrightarrow{g} = \mathbf{A} \circledast \overrightarrow{\theta} \tag{2.8}$$

Where $\overrightarrow{g}$ is a vector containing the fast signals of the detector, $\mathbf{A}$ is the system matrix of the detector (the response of the detector at the position of the event interaction), $\overrightarrow{\theta}$ represents the vector of parameters to be estimated (in this work, the two-dimensional positions). $\circledast$ is the symbol for convolution.

Referring to Figure 2.3, the fast signals labeled Fast_{Pred} and Fast_{Succ} for both the AC-Coupled (back of the detector) and DC-Coupled (front of the detector) sides are what makes up the $\overrightarrow{g}$ vector. The objective is to obtain a system matrix that will map the estimated two-dimensional event positions to the detector signal, and in doing so gives the positions with the highest likelihood (probability) of having produced those signals.

The likelihood is the probability distribution of the events within the detector. For scintillators and semiconductors, these probability distributions are typically represented by a multivariate normal (Gaussian) due to the multiple Poisson distributions of the events, decay method, noise, and signal generation [37, 56, 114]:

$$pr\left(\vec{g}|\overrightarrow{\theta_{x\,pos}}\right) = \frac{1}{\sqrt{(2\pi)^M}}\,\frac{1}{\sqrt{det|\mathbf{K_g}|}}\,exp\left\{-\frac{1}{2}\left[\left(\vec{g}-\bar{\mathbf{g}}\right)^T\ \mathbf{K_g}^{-1}\ \left(\vec{g}-\bar{\mathbf{g}}\right)\right]\right\} \tag{2.9}$$

where

$$\vec{g} = \begin{pmatrix} \mathbf{g_{Pred}} \\ \mathbf{g_{Succ}} \end{pmatrix};$$

M represents the number of dimensions (2 for this work), $\bar{\mathbf{g}}$ is the vector of the mean values at position ”x”; which is called the ”Mean Detector Response Function (MDRF)”. $\mathbf{K_g}$ is the covariance matrix of the Pred and Succ signals. A similar equation can be written for the ”y” position. Alternatively, equation 2.9 can be used to estimated both ”x” and ”y” positions simultaneously; this just adds extra dimensions to the $\mathbf{g}$ and $\bar{\mathbf{g}}$ vectors and $\mathbf{K_g}$. Taking the natural log of the equation, we get:

$$ln\left[pr\left(\vec{g}|\overrightarrow{\theta_{x\,pos}}\right)\right] = ln\left[\frac{1}{(2\pi)\sqrt{det|\mathbf{K_g}|}}\right] - \frac{1}{2}\left[\left(\vec{g}-\bar{\mathbf{g}}\right)^T\ \mathbf{K_g}^{-1}\ \left(\vec{g}-\bar{\mathbf{g}}\right)\right];$$

$$ln\left[pr\left(\vec{g}|\overrightarrow{\theta_{x\,pos}}\right)\right] = ln(2\pi) + \left(-\frac{1}{2}\right)ln\left(det|\mathbf{K_g}|\right) - \frac{1}{2}\left[\left(\vec{g}-\bar{\mathbf{g}}\right)^T\ \mathbf{K_g}^{-1}\ \left(\vec{g}-\bar{\mathbf{g}}\right)\right];$$

Getting rid of the ln(2π) and the $\frac{1}{2}$’s we get:

$$ln\left[pr\left(\vec{g}|\overrightarrow{\theta_{x\,pos}}\right)\right] = -ln\left(det|\mathbf{K_g}|\right) - \left[\left(\vec{g}-\bar{\mathbf{g}}\right)^T\ \mathbf{K_g}^{-1}\ \left(\vec{g}-\bar{\mathbf{g}}\right)\right] \tag{2.10}$$

And then the maximum value of the natural logarithm of the likelihood is written as:

$$\hat{\theta}_{ML} = \texttt{arg\_max}_{\vec{\theta}}\left\{ln\left[pr\left(\vec{g}|\vec{\theta}\right)\right]\right\} \tag{2.11}$$

where $\hat{\theta}_{ML}$ is the estimated position(s).

However, the accuracy of equation 2.11 depends on how well the model (equation 2.10) describes the event distribution. A figure of merit (FOM) that can be used to quantify how well the MLE does is called the Cramér-Rao Lower Bound (CR). The CR lower bound is the lower limit on the variance of a parameter (or parameters) based on the input data. In this work, the input data is the MDRF's and the CR lower bound represents the best spatial resolution that can be achieved [37, 114] . Thus, comparing the Full Width Half Max (FWHM) obtained from fitting a Gaussian to the resulting ML estimated images to the CR lower bound will show how precise the model is.

The CR lower bound is obtained from the Fisher Information Matrix (FIM) [37, 114]:

$$F_{ij} = \left\langle \left\{ \frac{\delta}{\delta\theta_i} \, ln\left[pr\left(\vec{g}|\vec{\theta}\right)\right] \right\} \left\{ \frac{\delta}{\delta\theta_j} \, ln\left[pr\left(\vec{g}|\vec{\theta}\right)\right] \right\} \right\rangle_{\left(\vec{g}|\vec{\theta}\right)} \tag{2.12}$$

where F_{ij} is a FIM matrix element. The FIM shows which direction the likelihood has the fastest change, i.e. which direction the MDRF's are more sensitive too. The CR lower bound is then the square root of the inverse of the trace of the FIM.

$$CR\ Lower\ Bound = \sqrt{\frac{1}{TR\left(F_{ij}\right)^{-1}}} \tag{2.13}$$

where $TR()$ represents the trace of a matrix

How the ML estimation, FIM and CR lower bound is applied to the actual detector signals is shown in the next section, after the acquisition of the system matrix is discussed.

2.4 Methods: Acquisition of System Matrix and Application of ML Estimation

2.4.1 The Advanced Photon Source (APS)

The Advanced Photon Source (APS) is located at the Argonne National Laboratory in Chicago, IL. It consists of five main components [115]: the linear accelerator, the booster synchrotron, the electron storage ring, insertion devices, and the experiment hall. It is 1,104 m in circumference, and contains 35 sectors with two beam lines each for experiments. The beamline used for this experiment was the 6D-ID beamline [116] with an energy range of 70-131 keV, and a photon flux of $\approx 10^{11}$ photons/s at a beam diameter of 1 mm^2; this was chosen as it was the beamline closest to the 140 keV emission of ^{99m}Tc.

The production of the x-rays at APS begins at the linear accelerator, where electrons are boiled off of a heated cathode and accelerated by alternating electric fields to 450 MeV. Next, the electrons enter the synchrotron, which is a circular structure of electromagnetics. Radio frequency electric fields accelerate the electrons further to 7 GeV while the magnets bend and focus their path.

From there, the electrons are injected into the large (1,104 m) storage ring, kept in their path by (1000+) electromagnets. Insertion devices help further tweak the beam into different energies and intensities as needed. These devices are ”wigglers”, wavelength shifters, and ”undulators” [117]. Lastly, the electrons are able to be inserted into 1 of the 40 straight line components (5 for beam injection). Further information on the five components discussed above can be found at [116] and links within.

At each beamline, an undulator and a monochromatic crystal is used to further adjust the photon flux and the energy desired [117, 118]. We also used vertical and horizontal slits to adjust the beam size to $\approx 25\,\mu \times 25\,\mu$. This resulted in a photon flux of $\approx 10^4$ photons/s and an energy of $\approx$ 131 keV. Beamline 6ID-D has an energy resolution of $\Delta E/E = 1.4 \times 10^{-3}$, much higher than our HPGe detector energy resolution.

2.4.2 Acquiring the System Matrix at APS

The measurement set-up and methodology for the DSS HPGe detector follows the experimental work done in Salcin, et al. [37]. The DSS HPGe detector was placed on an x-y translational stage, in front of the beam output.

Figure 2.12 shows a schematic of the measurement set-up at APS. The detector is placed on an x-y stage consisting of lifting columns, Movocat [119] from Thomson. The columns use an LA-10 actuator [120] and Imac motion control [121]. Resolution for these motors are 0.0127 mm/step. Motor control and data acquisition was accomplished by using the Experimental Physics and Industrial Control System (EPICS, [122]), MATLAB, and Imager32. Motion control was done within MATLAB via DOS commands to the EPICS software. Data acquisition is done using command pipes (C-pipes) within MATLAB to the Imager32 software.

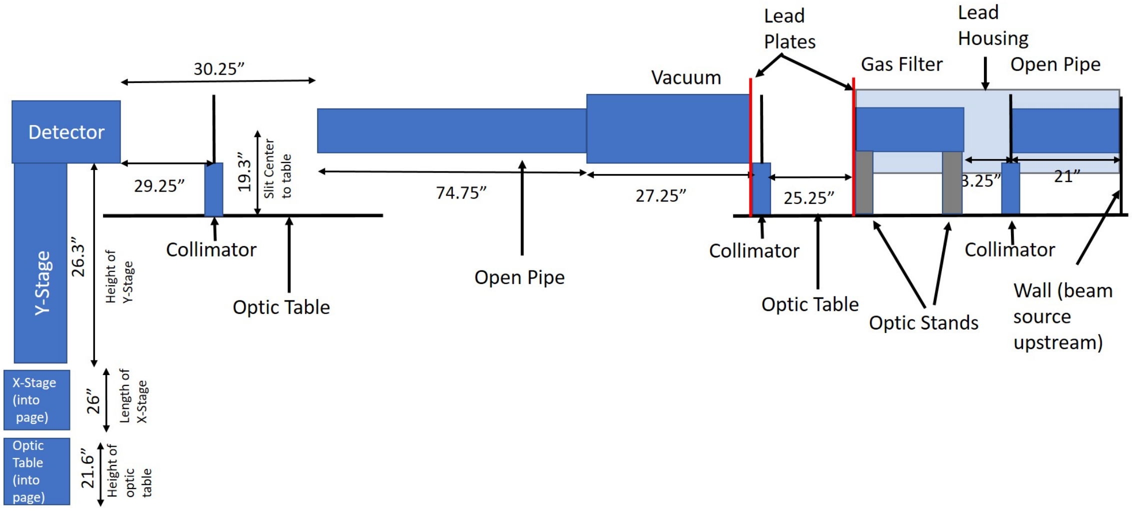

Figure 2.12: DSS HPGe Measurement Set-Up. Set-up consists of the x-y translational stages and detector on the left, with the aligning optics, vacuum tubes, etc. to the right of the detector. No significant beam diffusion was noticed with this set-up.

To find the appropriate photon flux for the DSS HPGe detector, we did various count rate measurements with different avaliable attenuation filters in order to decrease the photon flux. Figure 2.13 shows the detected counts in the HPGe detector vs. the photon flux (a.k.a. the transmission) of the beam. The count rate at the ”knee” of the saturation curve, is what we choose to go with, giving a us a count rate of $\approx 10^4$ photons/s. This knee represents the turning point right before the response of the detector system becomes saturated, i.e. the number of detected events will plateau after this point, no matter how high the photon flux is (see [5]).

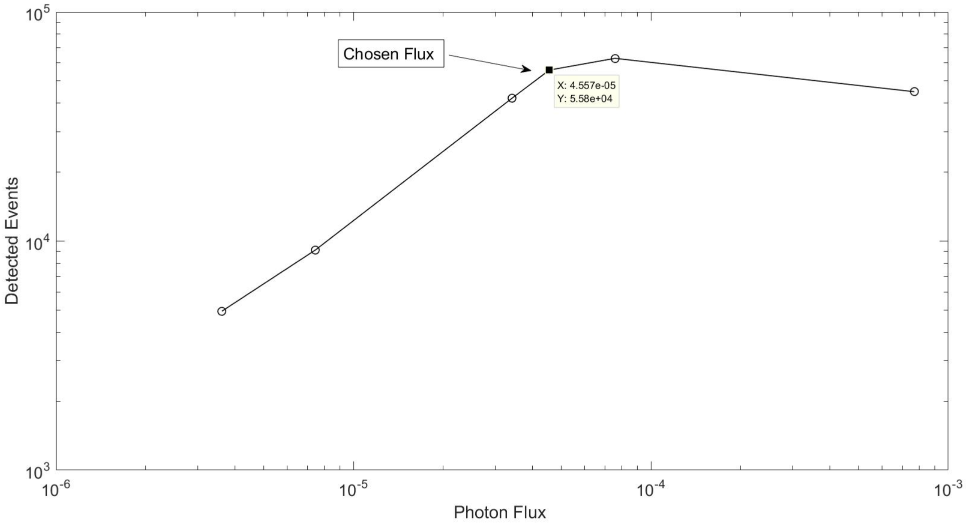

Figure 2.13: Counts vs. Photon Flux. Number of detected events vs. the photon flux for our DSS HPGe detector at APS.

The detector was moved across the beam, covering a 2x2 strip area in the center of the detector (10 x 10 mm^2) in steps of 0.25 mm and 0.5 mm for 30 second acquisitions. The different sampling of the data sets (the former with finer sampling than the latter) allows for the development of the ML model and for testing of that model. Additionally, a data set consisting of a single line acquisition from strip center to strip center (including the gap) in 0.1 mm steps provides information on charge sharing and possible charge loss mechanisms. Figure 2.14 (not to scale) shows how those acquisitions would look like as points across the strips.

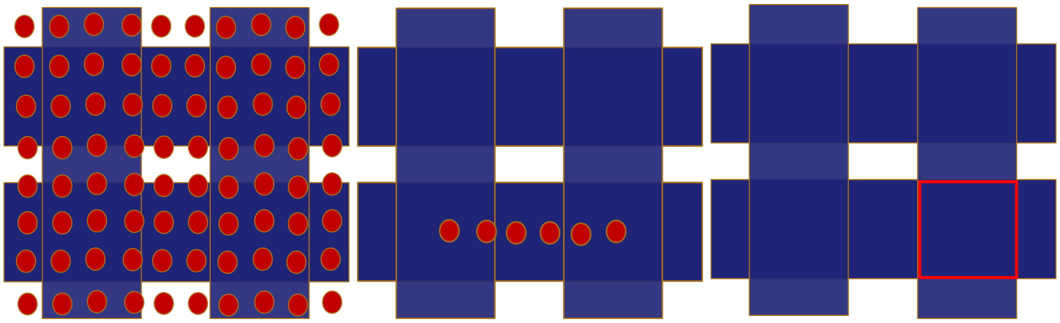

Figure 2.14: Schematic of Acquisition Patterns (not to scale). Left: Raster acquisition, Middle: Single linear acquisition, and Right: Example of a digital pixel (red square).

2.4.3 Application of ML Estimation

With the system matrix obtained, the first step is to calculate the MDRF functions for each position. Note that this step and the following are done to a single digital pixel (see Figure 2.14, right schematic) as preliminary data, with the full data results to be shown in Chapter 3. Data examples in this chapter will either be from the full digital pixel and/or select locations within that digital pixel (see Figure 2.15). Figures 2.16 and 2.17 show the fast signal distributions for beam locations at the left edge, center, right edge, and corner for each depth.

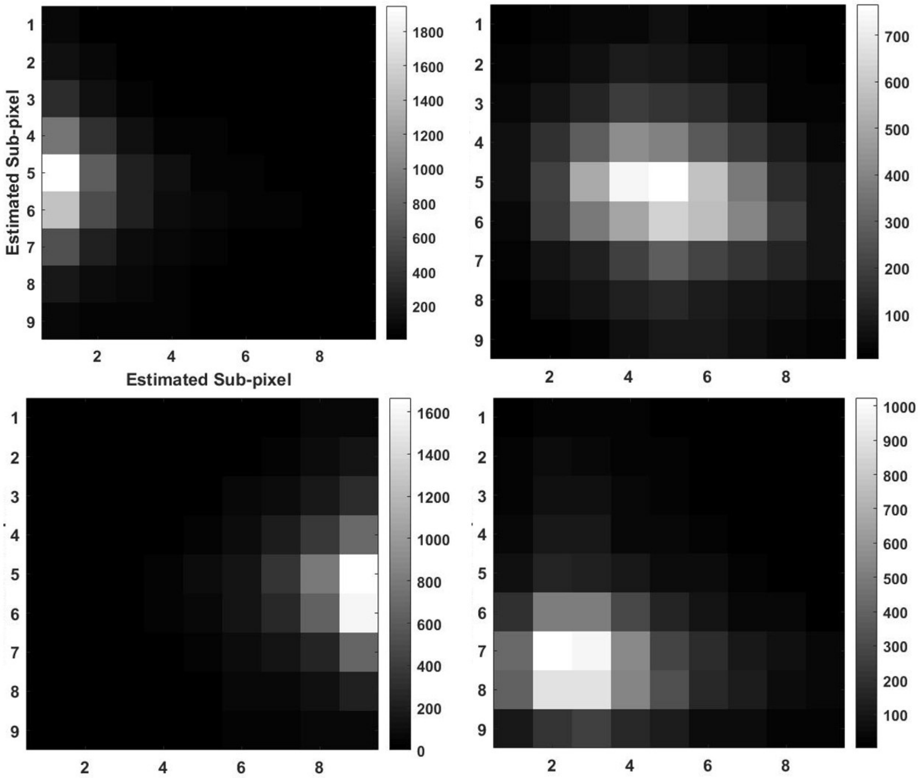

Figure 2.15: Example Locations within a Digital Pixel of the DSS HPGe Detector. Four example beam spots within a digital pixel: From top left to bottom right: left edge, center, right edge, and corner of the pixel. Positioning of events for these images was done using the position-ratio method.

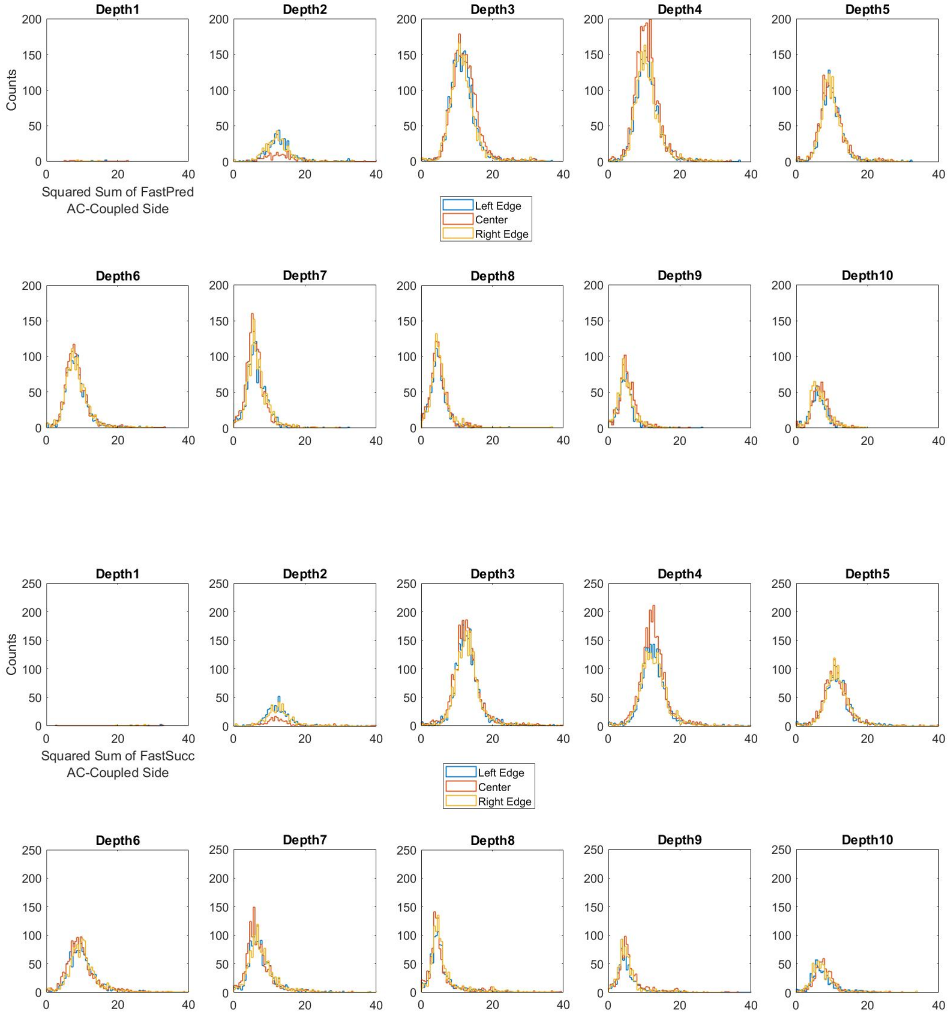

Figure 2.16: Fast Signal Distributions for Three Beam Locations on a Digital Pixel (I). Direction of beam travel is parallel to the AC-Strips. Top: Squared summed of the FastPred signal distributions, AC-coupled side of the detector. Bottom: Same as Top but for the FastSucc signal. Blue histogram represents the left edge location, orange-red the center, and yellow the right edge.

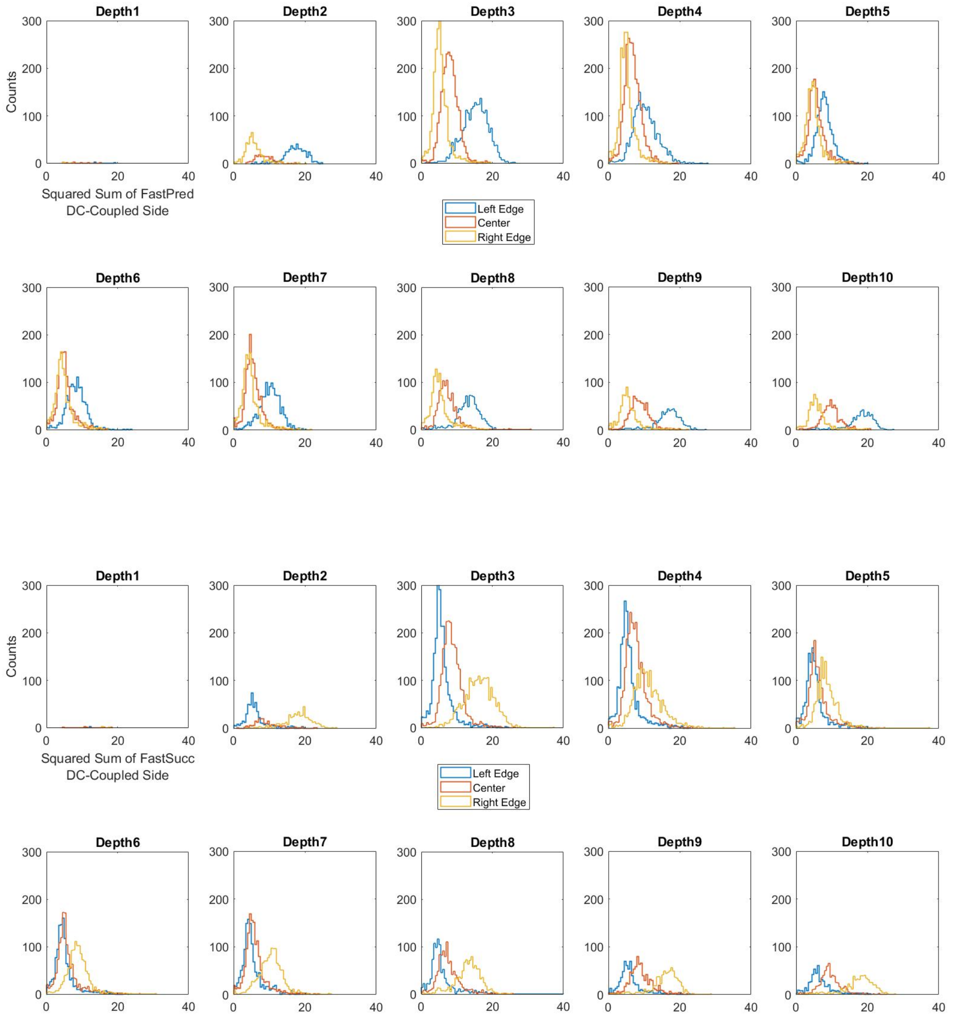

Figure 2.17: Fast Signal Distributions for Three Beam Locations on a Digital Pixel (II). Same description as Figure 2.16 but for the DC-coupled side of the detector, where the direction of beam travel is perpendicular to the DC-strips.

For the beam moving in the other direction (parallel to DC-strips and perpendicular to AC-strips), the fast signal distributions will look similar, only reversed. DC-strips will change very little between locations and AC-strip distributions will shift. The more overlap there is between the fast signals at different locations, the harder it is to to differentiate them for event sub-strip positioning.

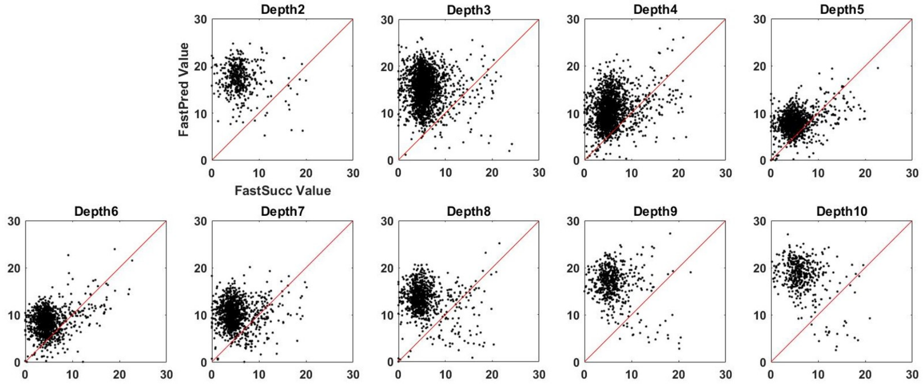

Figure 2.18: Fast Signal Correlation Plot, Left Edge of Pixel. FastPred vs. FastSucc for each depth. Each black dot represents an event, red-line represents complete correlation. At the left edge of the pixel, the FastPred strip has more charge induced on it.

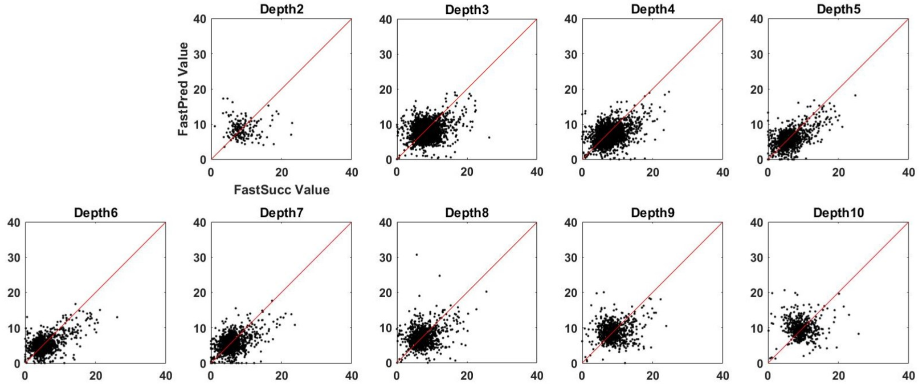

Figure 2.19: Fast Signal Correlation Plot, Center of Pixel. Same description as 2.18. Both FastPred and FastSucc roughly share the same amount of charge induction.

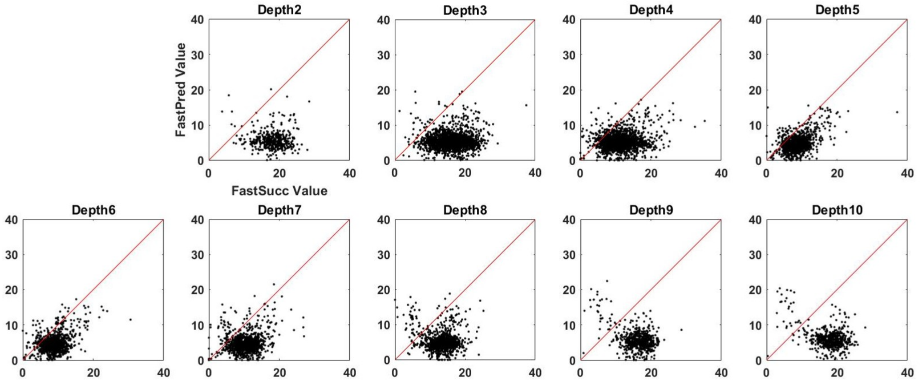

Figure 2.20: Fast Signal Correlation Plot, Right Edge of Pixel. Same description as 2.18. At the right edge of the pixel, the FastSucc strip has more charge induced on it.

Figures 2.18, 2.19, and 2.20 show the correlation between the FastPred and FastSucc signals as the beam moves across the strip. As stated above, the beam is moving parallel to the horizontal AC-coupled strips, so it is the fast signals from DC-coupled strips that will experience change in the amount of induced charge. This is seen in the correlation plots as the distribution shifts from the FastPred side, to the ”middle” and then to the FastSucc side. This is also seen in the opposite direction (plots not shown).

Figures 2.21 and 2.22 show the MDRFs at each beam location for the AC- and DC-Coupled sides, respectively. Since the MDRF’s for the AC-Coupled side are roughly constant in the horizontal direction, these fast signals are used for estimating the vertical/y position of the event. Similarly for the DC-Coupled side, which are constant along the vertical direction and are used for estimation in the horizontal/x direction. Depth 1 in both cases is noisy due to the small number of events that occurs there.

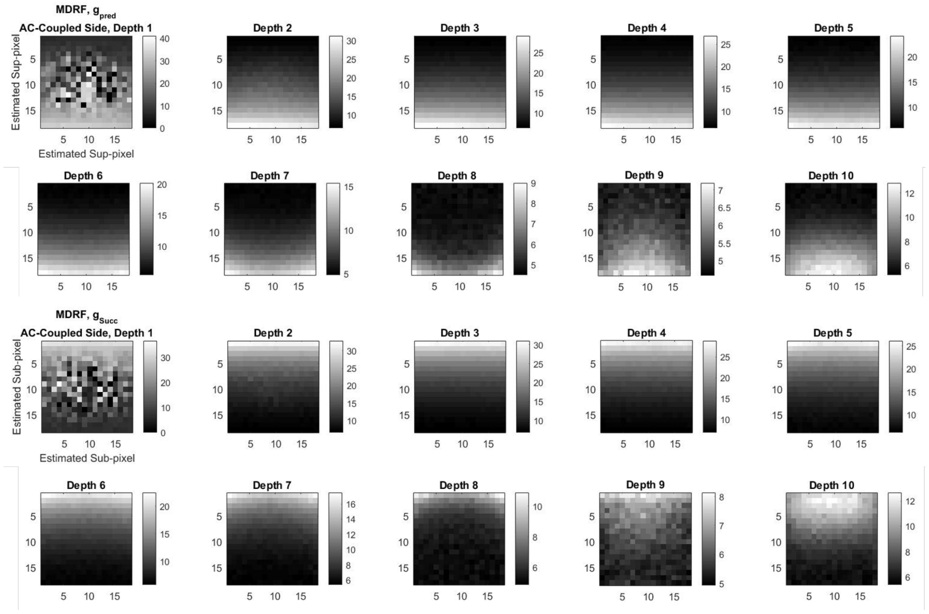

Figure 2.21: MDRFs, AC-Coupled Side. MDRFs for $\overline{\mathbf{g}}_{Pred}$ (top) and $\overline{\mathbf{g}}_{Succ}$ (bottom) for all 10 depths.The x and y axis are the estimated sub-pixel positions and the colorbar represents the mean of the fast signals from all of the events that occurred in that location.

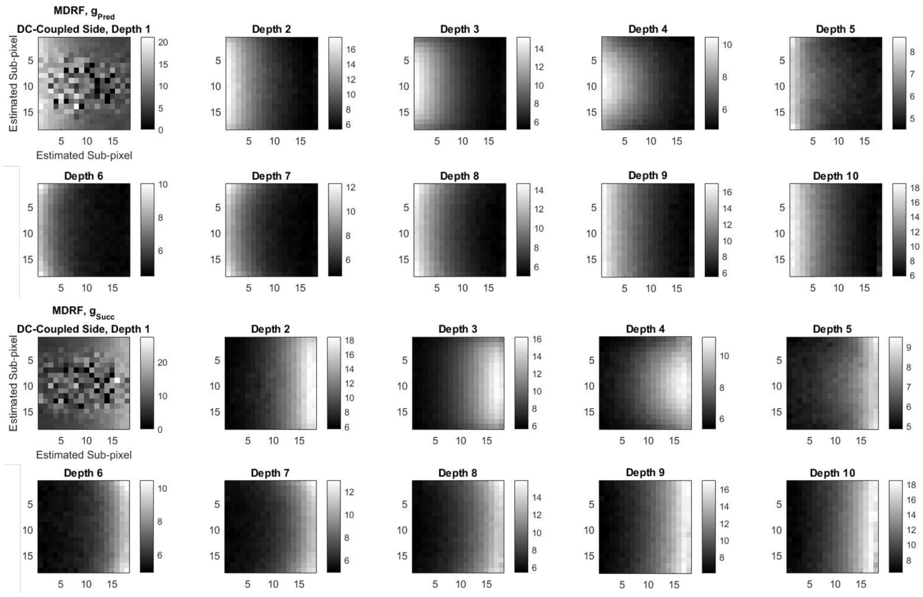

Figure 2.22: MDRFs, DC-Coupled Side. Same as Figure 2.21 but for the DC-Coupled side.

Next, the covariance matrix, the inverse, and its determinant are needed to obtain information about the noise from the detector. This is done using the fast signals as well. For a one-dimensional estimation (say either the AC- or the DC-coupled side), only two fast signals are used for the covariance calculation. For a two-dimensional estimation, both the AC- and DC-coupled signals (four in total) are used. Equation 2.9 then uses the determinant and the inverse covariance, from the resultant covariance matrix. The covariance itself provides information about the data; the diagonals of the covariance matrix represent the variance of the FastPred and FastSucc while the off-diagonals are the covariances between them. A covariance map then shows how the variance of the fast signals changes with position (for diagonal elements) and how the covariances of the signals vary together with position. Figure 2.23 shows the inverse covariance for each sub-pixel as a function of depth.

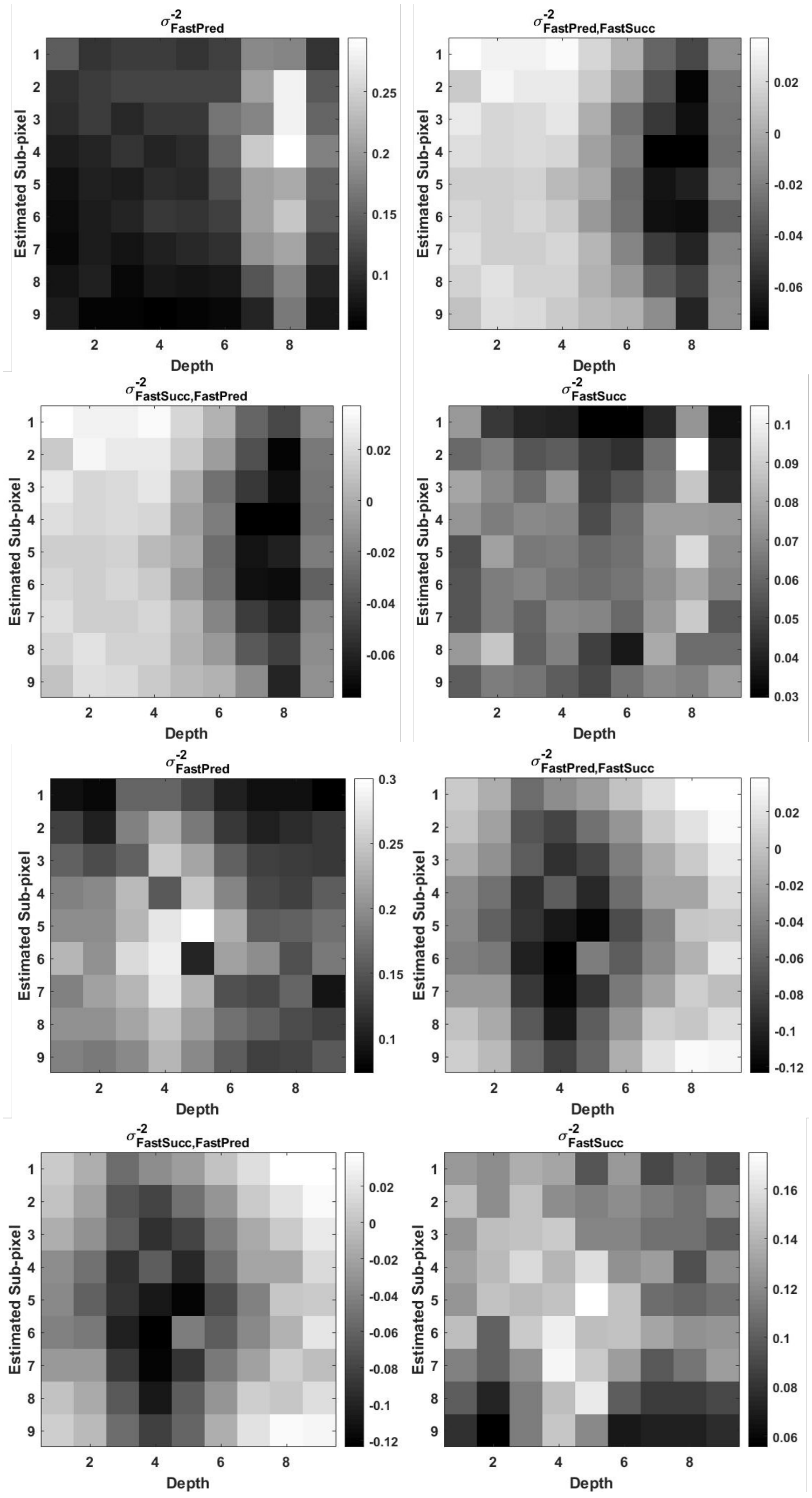

Figure 2.23: Inverse Covariance Values by Depth. Top four: AC-coupled side, Bottom four: DC-Coupled side. $\sigma^{-2}_{FastPred}$, $\sigma^{-2}_{FastPred,FastSucc}$, $\sigma^{-2}_{FastSucc,FastPred}$, $\sigma^{-2}_{FastPred}$ are the corresponding inverse varience/covariance values for the corresponding fast signals.

The last value obtained from the covarience matrix is the determinant. The determinant in equation 2.9 acts as a scaling factor, and in our case, is a function of both the variances and covariances so it is not expected to be constant. Figure 2.24 shows the determinant values as a function of depth for each sub-pixel. For the AC-coupled side, the determinant value does seem to depend on the position on the digital pixel, while it does not on the DC-coupled side for most locations (except for the first and last depths).

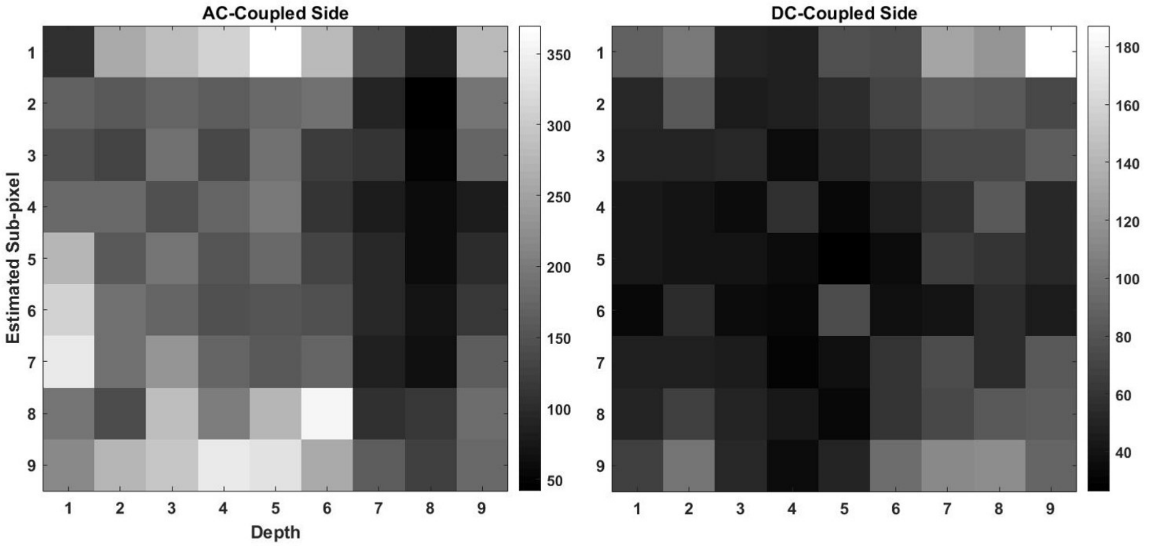

Figure 2.24: Determinant Matrix Values. Left: Determinant of the covariance matrix for the AC-Coupled side, Right: Same as left, but for the DC-Coupled side. Both are for depth 5.

With the MDRF's, inverse covariance values, and determinants all pre-calculated, we then performed the MLE:

- For both 1-D and 2-D ML estimations:
  - MDRF's are smoothed over with a MATLAB function, imgaussfilt(), (with the "FilterSize" option, or the kernal size, set to 3x3 pixels [123]).

- In the 1-D MLE, the central row and column values of the smoothed MDRF's are used for the likelihood calculation. In the 2-D MLE an exhaustive search, i.e. each MDRF value for every possible position is used.
- Once the maximum likelihood value is calculated, it's corresponding x and y index position and depth is recorded. These indices are then used in a 9x9x10 matrix to form the estimated image.
- The resulting image is then summed into an x and y projection and fit to a Gaussian to obtain the spatial resolution and width. These parameters are used to quantitatively compare the performance of the positioning methods. The width times the sub-pixel size of 0.53 mm is compared to the CR Lower Bound to judge the system performance.
- Lastly, sample means between the methods is calculated to quantify weather the MLE methods are able to remove the distortion that is seen with the position-ratio method of preferentially placing more counts at the edge of the pixel.

Chapter 3 will show and discuss these results.

Chapter 3

MLE Results: Spatial Resolution, Bias, and Implications

For both the 1-D and the 2-D MLEs, representative images and fits are shown for the left edge, center, and corner of the pixel. Estimations and fits are done for two cases: (1) summed over all depths and (2) each depth individually. In the case of (2), only the image of the beam positioned at the pixel center is shown (for brevity). Lastly, results for the CR Lower Bound will be shown, but not the FIM values (the CR Lower Bound is just the inverse of the FIM).

3.1 MLE 1-D Results

Figures 3.1, 3.2, and 3.3 show the results from the position-ratio and MLE 1-D methods (summed over all depths) for the beam positioned at the left edge, center, and corner of the pixel (right edge is not shown as that is similar to the left edge). Note: for brevity the position-ratio method is labelled ”RM” (for ”raw mode”) in the plots that follow.

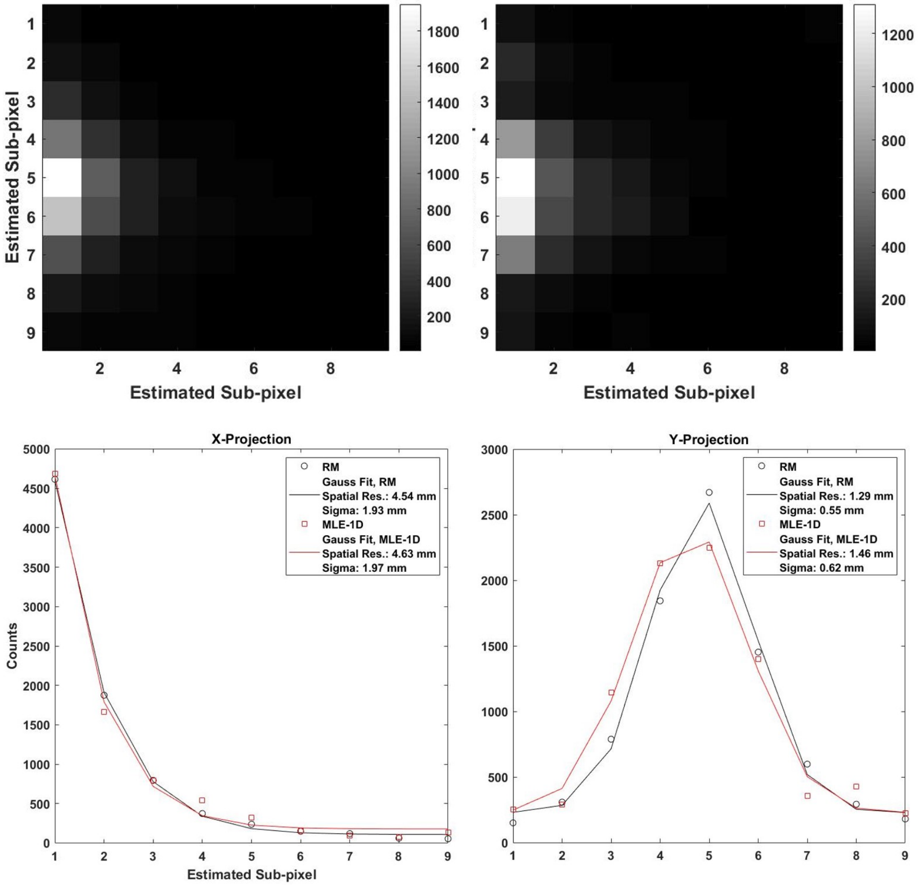

Figure 3.1: position-ratio Method vs. MLE 1-D Method, Left Edge of Pixel. Top: Images resulting from summing the events over all depths for: Left - position-ratio Method and Right - MLE 1-D Method. Bottom: Gaussian fits to the x- and y- projections of the same images. Black circles and line represent the data from the position-ratio method, red squares and line represent the MLE 1-D data.

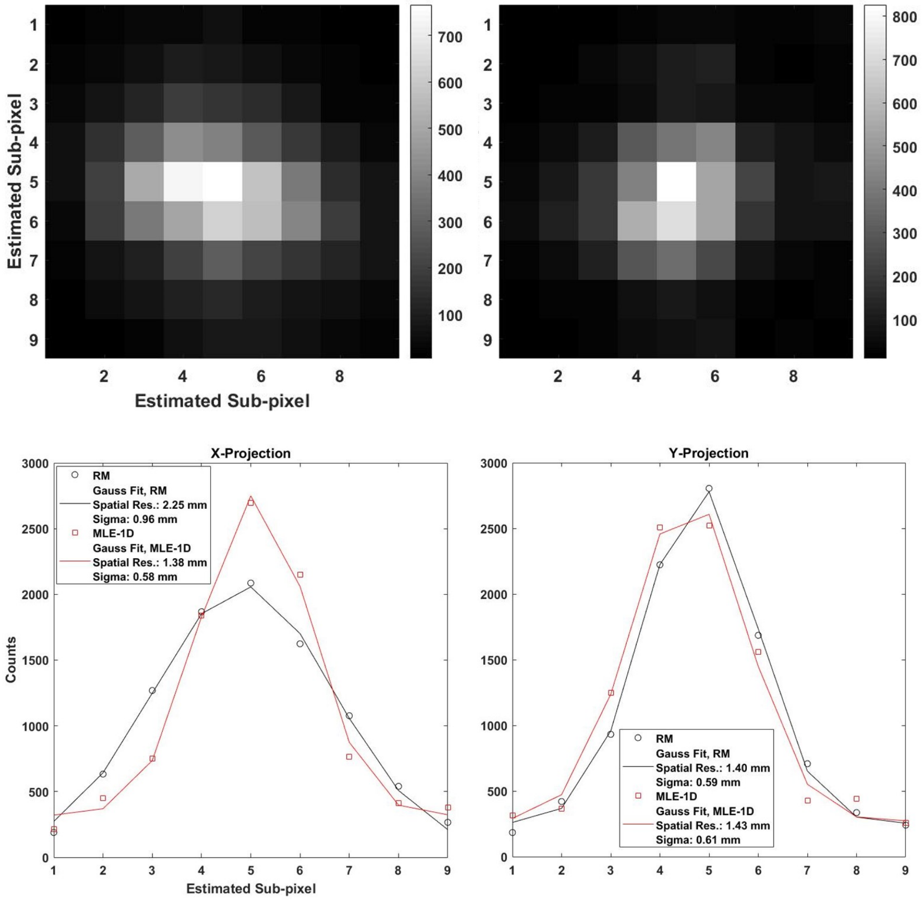

Figure 3.2: position-ratio Method vs. MLE 1-D Method, Center of Pixel. Same description as 3.1, but for the beam positioned at the center of the pixel.

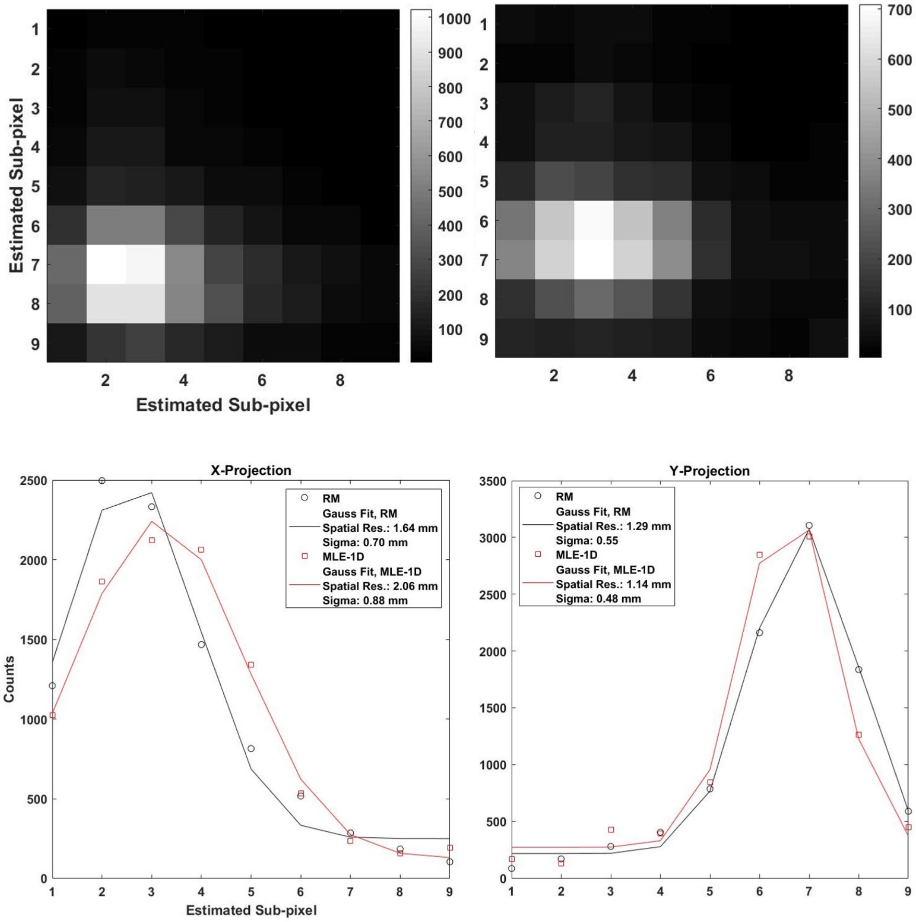

Figure 3.3: position-ratio Method vs. MLE 1-D Method, Corner of Pixel. Same description as 3.1, but for the beam positioned at the corner of the pixel.

3.1.1 MLE 1-D Results by Depth

Figures 3.4, 3.5, and 3.6 along with Table 3.1 show results of the position-ratio method vs. the MLE 1-D method for the beam at the center of the pixel and depths 2-10. Figure 3.6 shows the result of the Gaussian fitting for both methods for the x-projection only.

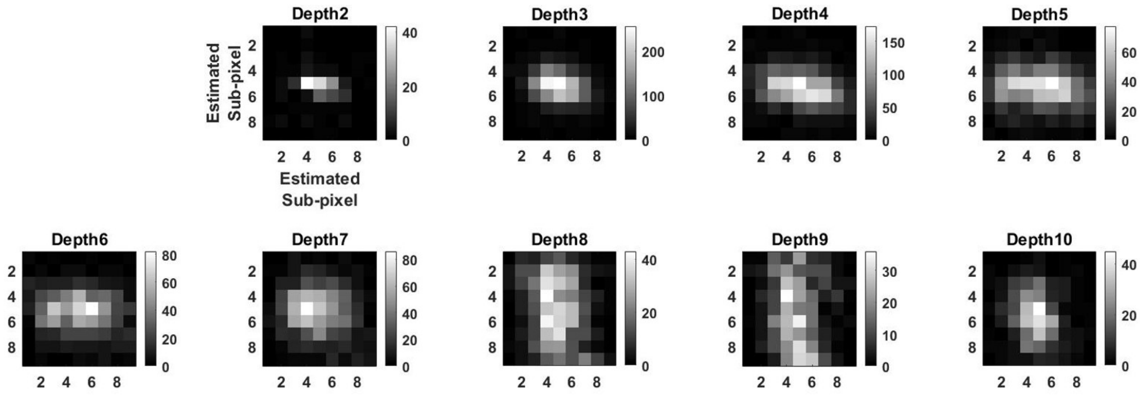

Figure 3.4: Image of Beam at Pixel Center via position-ratio Method at Depths 2-10. Depths 2-10 are shown, depth 1 is excluded due to the low number of counts.

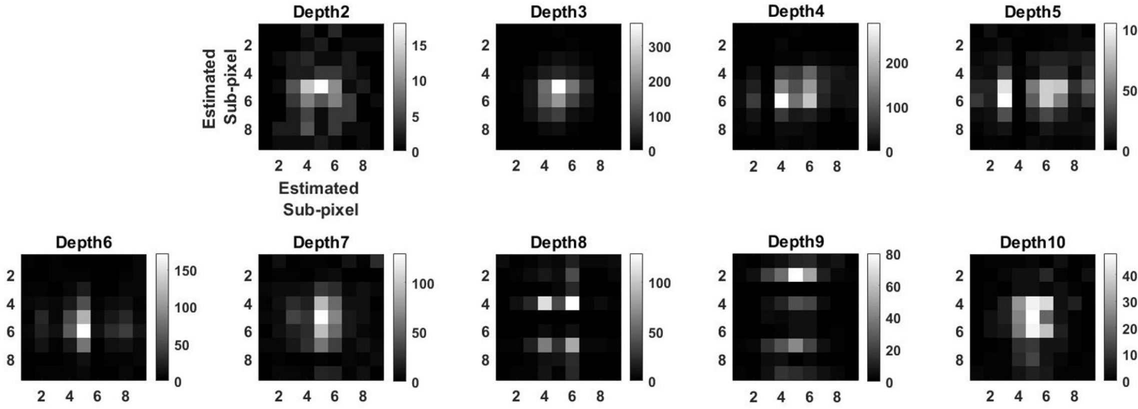

Figure 3.5: Image of Beam at Pixel Center via MLE 1-D at Depths 2-10. Same description as Figure 3.5

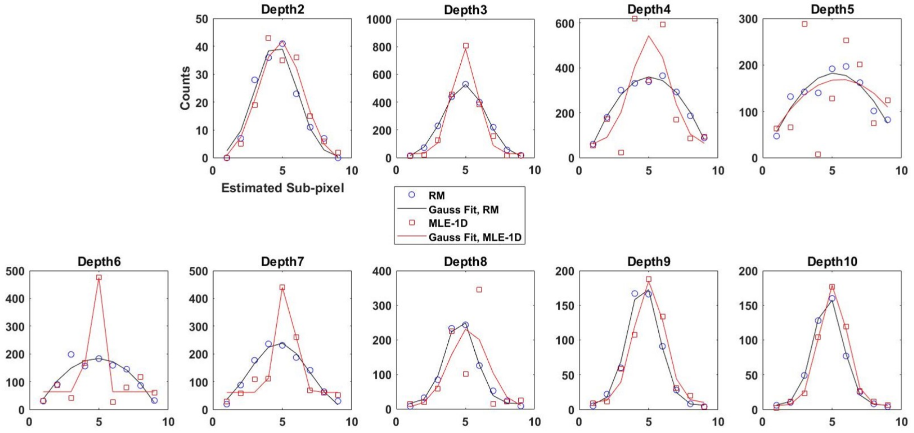

Figure 3.6: Gaussian Fits, position-ratio vs. MLE 1-D Method for Beam at Center of Pixel for Depths 2-10. Circles represent the position-ratio data while squares represent the MLE 1-D data. Spatial resolution (FWHM) and sigma of the fits are listed in Table 3.1.

Table 3.1: position-ratio and MLE 1-D Gaussian fits to Beam at Center of Pixel at Depths 2-10.

	position-ratio Method		MLE 1-D	
Depth	Spatial Resolution (mm)	σ (mm)	Spatial Resolution (mm)	σ (mm)
2	1.86	0.79	2.00	0.85
3	1.88	0.80	1.14	0.48
4	11.35	4.83	1.67	0.71
5	9.56	4.06	163.30	69.49
6	97.35	41.42	0.30	0.13
7	2.70	1.15	0.76	0.32
8	1.35	0.57	1.70	0.72
9	1.39	0.59	1.34	0.57
10	1.30	0.55	1.22	0.52

3.2 MLE 2-D Results

The figures that follow will be in the same order as the MLE 1-D: Summed results, results by depth and fits for the left edge, center and corner.

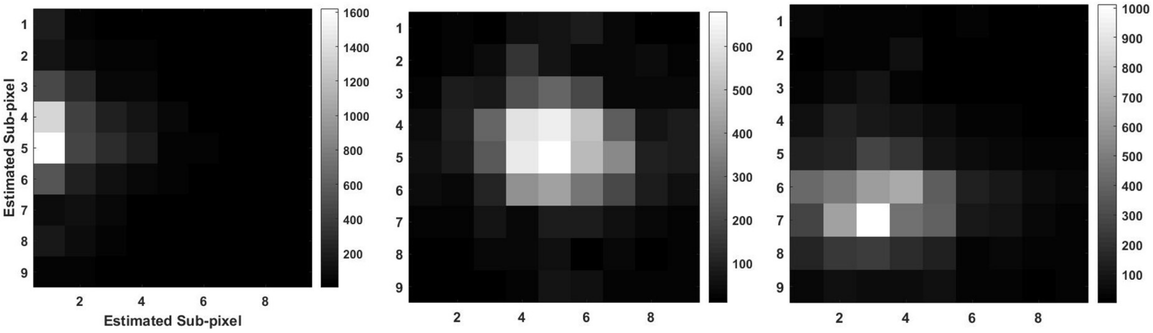

Figure 3.7: MLE 2-D Images for the left edge (left image), center (center image), and corner of the pixel (right image.

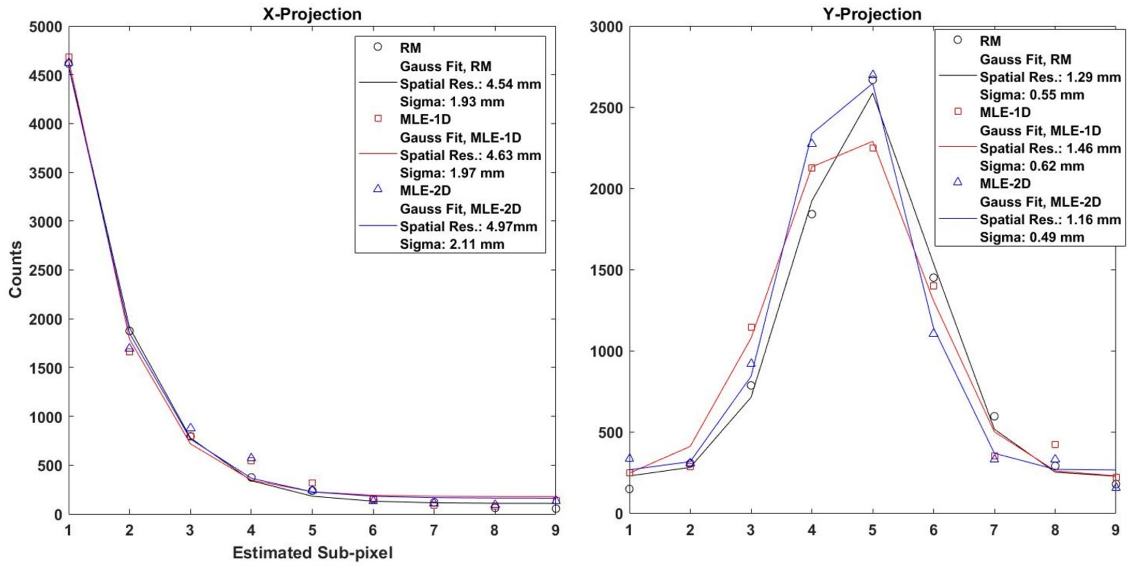

Figure 3.8: Gaussian Fits to Left Edge of Pixel for All Estimation Methods. Circles are the RM method, squares are the MLE 1-D method, and triangles are the MLE 2-D method. Left: Fit to the x-projection of the image. Right: Fit to the y-projection of the image.

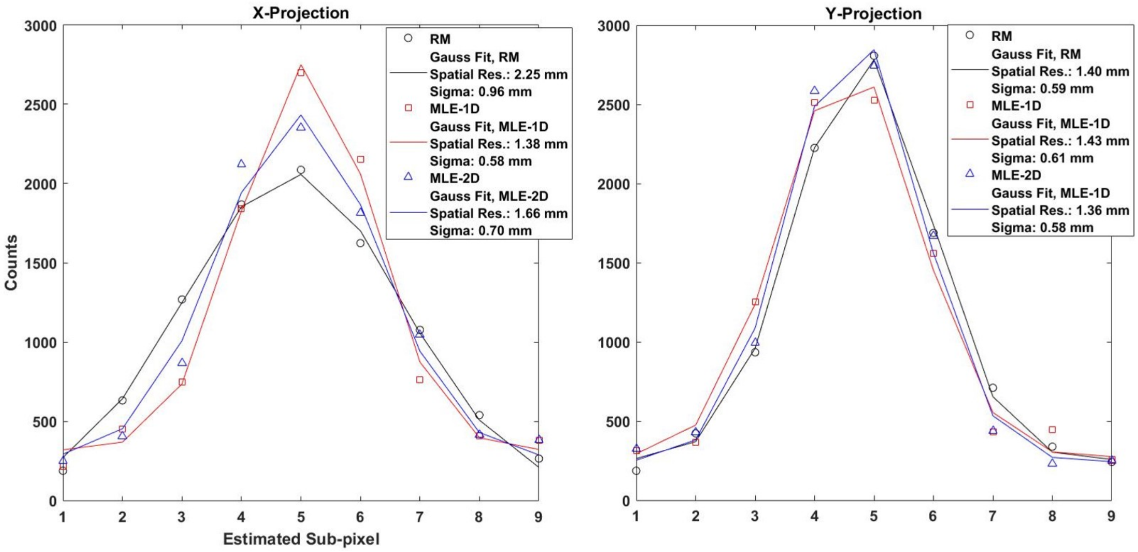

Figure 3.9: Gaussian Fits to Center of Pixel for All Estimation Methods. Description is the same as Figure 3.8.

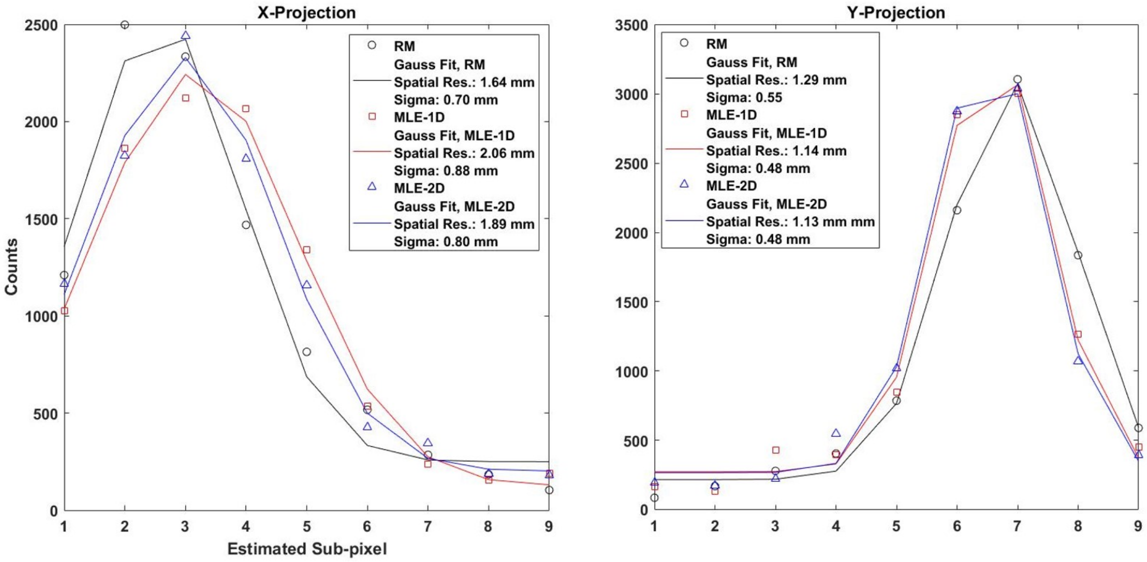

Figure 3.10: Gaussian Fits to Corner of Pixel for All Estimation Methods. Description is the same as Figure 3.8.

3.2.1 MLE 2-D Results by Depth

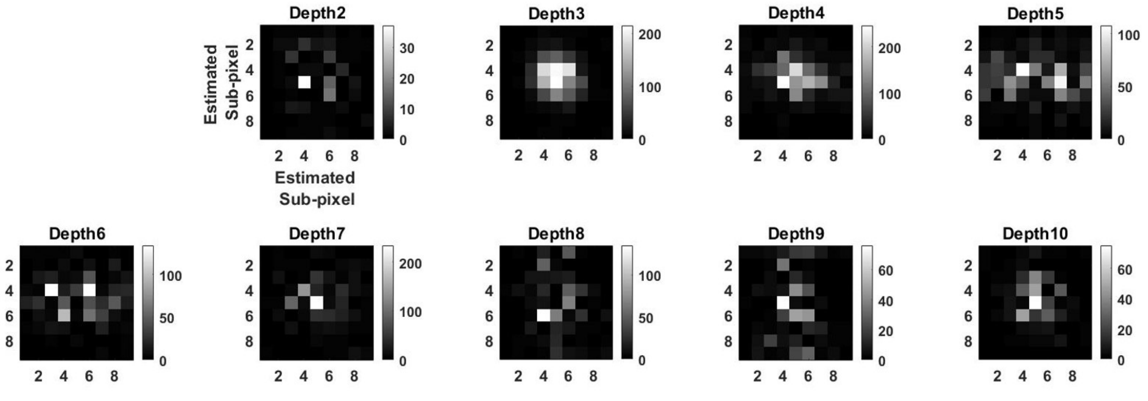

Figure 3.11: Image of Beam at Pixel Center via Position MLE 2-D at Depths 2-10. Depths 2-10 are shown, depth 1 is excluded due to the low number of counts.

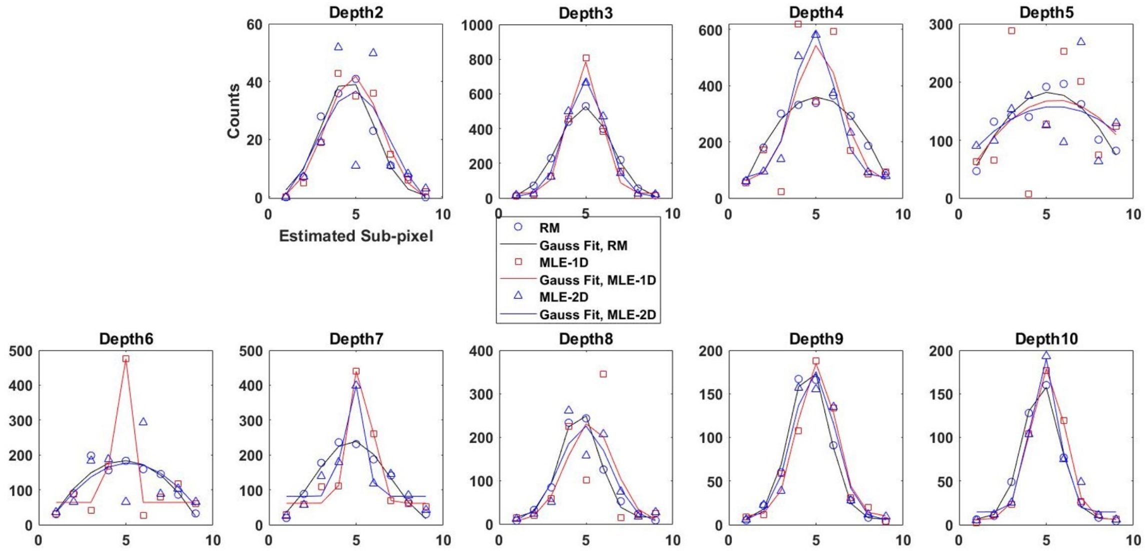

Figure 3.12: Gaussian Fits, position-ratio, and MLE 1-D and 2-D Methods for Beam at Center of Pixel for Depths 2-10. Circles represent the position-ratio data, squares represent the MLE 1-D data, and triangles represent the MLE 2-D data. Spatial resolution (FWHM) and sigma of the position-ratio and MLE 1-D are listed in Table 3.1 while MLE 2-D is in Table 3.2 below.

Table 3.2: position-ratio and MLE 1-D and 2-D Gaussian fits to Beam at Center of Pixel at Depths 2-10.

	Position Ratio Method	MLE 1-D	MLE 2-D
Depth	Spatial Resolution +/- σ (mm)	Spatial Resolution +/- σ (mm)	Spatial Resolution +/- σ (mm)
2	1.86 +/- 0.79	2.00 +/- 0.85	2.60 +/- 1.10
3	1.88 +/- 0.80	1.14 +/- 0.48	1.40 +/- 0.59
4	11.35 +/- 4.83	1.67 +/- 0.71	1.42 +/- 0.60
5	9.56 +/- 4.06	163.30 +/- 69.49	145.78 +/- 62.03
6	97.35 +/- 41.42	0.30 +/- 0.13	9.31 +/- 3.96
7	2.70 +/- 1.15	0.76 +/- 0.32	0.69 +/- 0.29
8	1.35 +/- 0.57	1.70 +/- 0.72	1.77 +/- 0.75
9	1.39 +/- 0.59	1.34 +/- 0.57	1.50 +/- 0.64
10	1.30 +/- 0.55	1.22 +/- 0.52	0.98 +/- 0.41

3.3 Quantifying the Results

The following results show how we quantified and comparted the performance of the MLE methods to the position-ratio method. This was done using:

- The CR lower bound and comparing that to the width of the fitted Gaussian for the X- and Y- projections of each test spot.
- Comparing the sample means and standard deviations from the event distributions at each beam position for the position-ratio and MLE 2-D method.
- Comparing the spatial response and average spatial resolution from pseudo-flood images of the digital pixel.
- Comparing how the MLE method performs on a center test spot from the other (three) digital pixels using the MDRFs of the analyized digital pixel.

3.3.1 MLE 1-D CR Lower Bound, and MLE 2-D Sample Mean

Figures 3.13 and 3.14 show the resulting values for the CR for the MLE 1-D case, MLE 2-D not shown (the CR for MLE 2-D is a 2-D image instead of a plot,thus, only MLE 1-D is shown for simplicity). The sample mean, Figure 3.15 is shown for both the position estimation ratio and MLE 2-D.

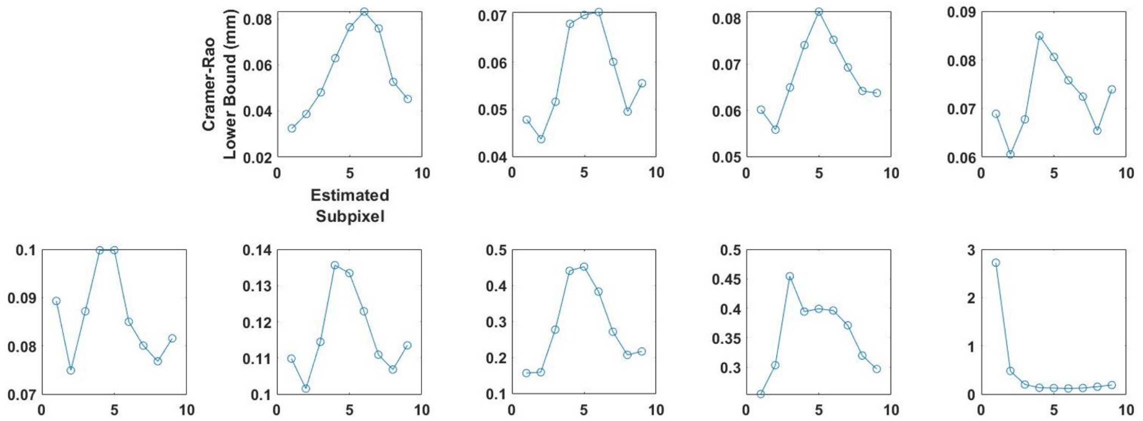

Figure 3.13: CR Lower Bound for the AC-Coupled Side of the Detector for Depths 2-10.

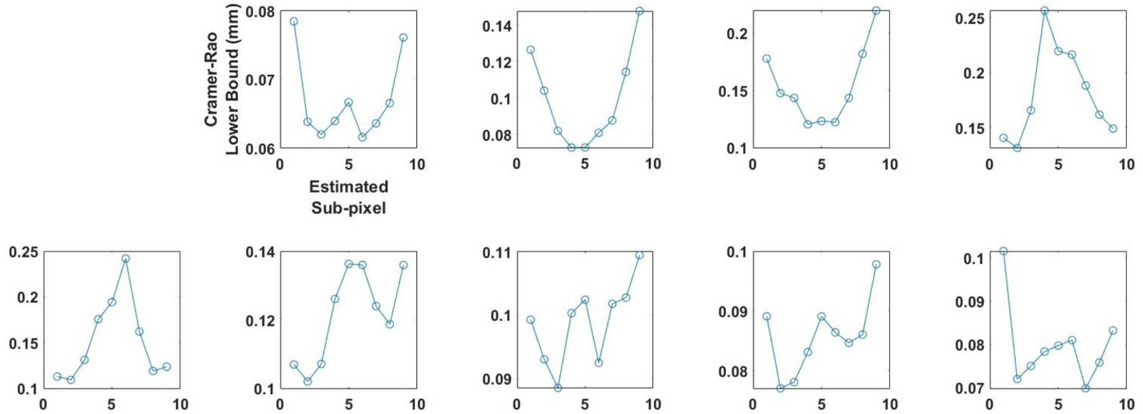

Figure 3.14: CR Lower Bound for the DC-Coupled Side of the Detector for Depths 2-10.

In addition to the raster scan, another data set was taken from the center of a strip to the center of the next strip in steps of 0.05 mm. This data set is used in Figure 3.15 to see if the MLE method places events differently than the position-ratio method.

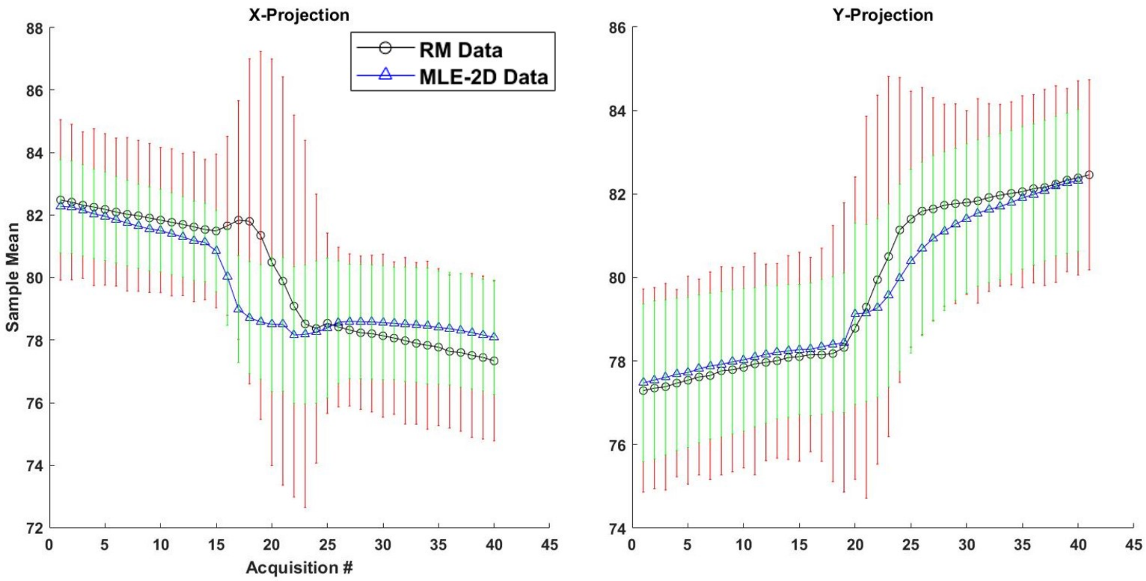

Figure 3.15: Sample Mean of Estimated Positions for position-ratio and MLE 2-D Methods. Sample means are plotted for position estimation methods for the X-projection (left plot) and Y-projection (right plot). Red lines are the standard deviation to the sample mean for the position-ratio method while the green lines are for the MLE 2-D method.

3.3.2 Pseudo-Floods and Average Spatial Resolution

Using the images from all of the beam positions of the digital pixel, a pseudo-flood image was made for each method to see how the spatial response changes across the digital pixel. These images are shown in Figure 3.16. Table 3.3 lists the average resolution across the pixel for each method.

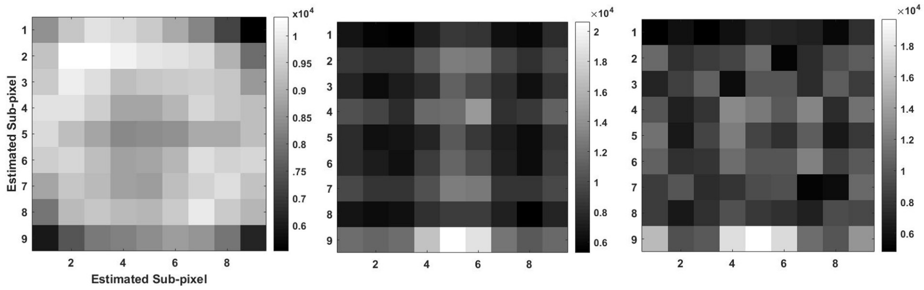

Figure 3.16: Pseudo-floods Using position-ratio Method, MLE 1-D, and MLE 2-D. Left: position-ratio Method, Middle: MLE 1-D, and Right: MLE 2-D.

Table 3.3: Average Spatial Resolution. Spatial resolution in mm.

Position Ratio Method	MLE 1-D	MLE 2-D
X: 2.69 +/- 1.14 Y: 1.82 +/- 0.77	X: 2.81 +/- 1.19 Y: 1.28 +/- 0.54	X: 2.67 +/- 1.13 Y: 1.19 +/- 0.50

3.3.3 Spot Tests: Other Digital Pixels

Since the raster data collected spans a 2x2 strip area, we can see how well the MLE method works at other detector locations using the calibration (i.e. the MDRFs) of the analyzed digital pixel. These spots should be compared to the center spot in Figure 3.7 and the Gaussian fit in Figure 3.9.

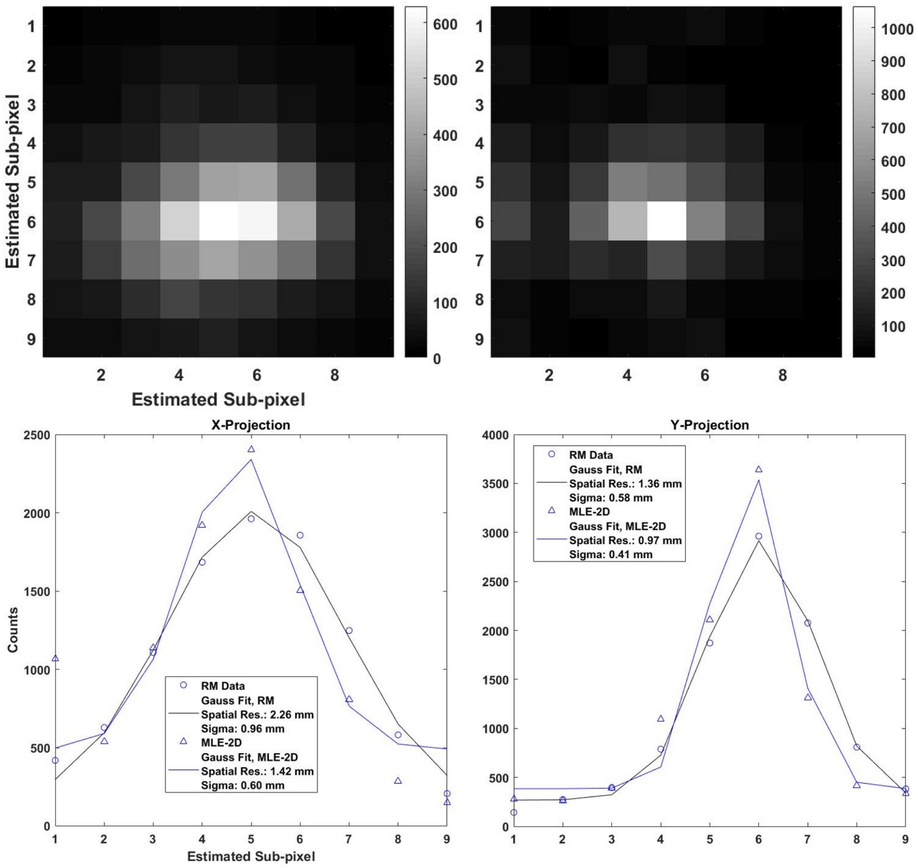

Figure 3.17: Beam Position in Lower Left Digital Pixel. Beam spot located near the center in the lower left digital pixel of the 2x2 strip scan. Top Left: image via position-ratio method, Top Right: image via MLE 2-D method. Bottom Left: Gauss fits to the x-projection of the image for both methods, Bottom Right: Gauss fits to the y-projection for both methods.

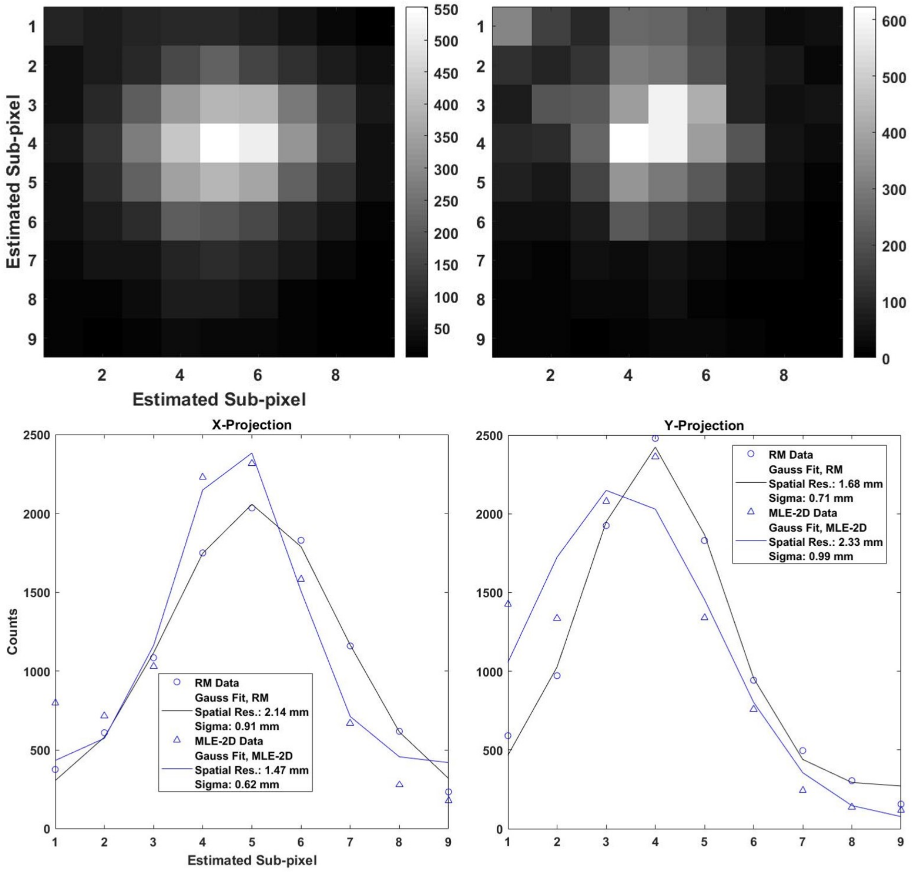

Figure 3.18: Beam Spot in Upper Left Digital Pixel. Same description as 3.17, but for the upper left digital pixel.

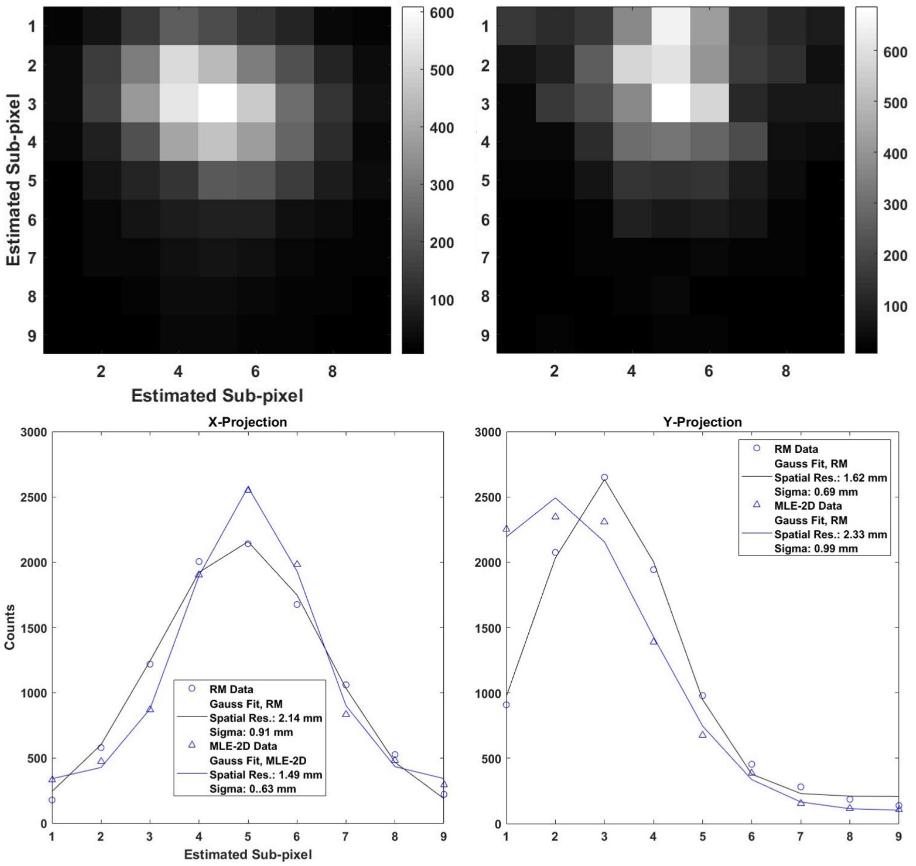

Figure 3.19: Beam Spot in Upper Right Digital Pixel. Same description as 3.17, but for the upper right digital pixel.

3.4 Discussion

MLE 1-D Results: Section 3.1.1 contains the results from the MLE 1-D. While there is improvement to the spatial resolution for the center of the pixel, MLE 1-D is only comparable to the position-ratio estimation method at the edge and the corner (x-projection) of the pixel. Gaussian fits are poor for both methods at the edge due to the fact that some of the counts are lost to the gap, or are collected by the next strip over, making the projection in the x-direction asymmetric.

MLE 1-D By Depth Results: Both the position-ratio and MLE 1-D methods have asymmetries in the spatial resolution that is dependent on the depth of interaction. Depths 2-4 are symmetrical, depths 5-7 have better spatial resolution along the x-axis, and depths 8 and 9 (and 10 to an extent) have better spatial resolution along the y-axis. Since the detector is reverse-biased, the AC-coupled side collects the electrons and the DC-coupled side collects the holes, one reason for this behavior is that the electrodes are more sensitive as their respective charge carriers get closer. Also, the distance that the electrons and holes have to travel from the point of interaction also plays into this. An interaction in the upper half of the detector means that the holes will have a shorter distance to travel than the electrons. This could affect the size of the charge clouds as the charge carriers reach their respective electrodes, making the electron charge cloud larger. Modeling the signal generation of the detector can determine the initial size and growth due to diffusion of the charge clouds to see if this causes the asymmetry.

One difference between the two methods is that the MLE 1-D images experience ”missing” counts. For example, depth 5 in Figure 3.5 contains no counts in column 4, even with adjacent columns containing counts. This occurs for each beam position and is also seen with other columns or rows at other depths. This could be due to the selection of a particular row and column from the MDRFs to be used in the ML estimation. It is also possible that there are small differences in the likelihood values such that some sub-pixels are never chosen.

The spatial resolution by depth is essentially similar between the two methods (when a good fit is possible). Depth 5 in the x-projection will always be poor (and vice-versa for the y-projection (not shown) at depths 8 and 9). Generally, the Gaussian fitting by depth does not perform well (although for the counts summed over all depths the fit does work well).

MLE 2-D Results: Figure 3.7 shows the summed MLE 2-D images, while Figures 3.8, 3.9, and 3.10 show the Gaussian fits. MLE 2-D performs better, with a better spatial resolution in most cases compared to both the position-ratio method and the MLE 1-D method with the exception of being comparable to MLE 1-D at the center.

MLE 2-D By Depth Results: The same pattern of spatial resolution dependence on depth that is seen in the position-ratio method and the MLE 1-D method is also present in the MLE 2-D method. However, the MLE 2-D method does not have the ”missing” counts issue that is seen in MLE 1-D. In this method, all possible values of the likelihood are calculated from the full MDRFs (rather than a single row or column). The spatial resolution by depth is similar to Figure 3.6.

FIM and CR Lower Bound: FIM is based on the MDRFs from the data and not on the estimation method, thus, using the CR Lower Bound that is obtained from the FIM is one way to examine the performance of our detector. If we compare some of the sigma values from the fits that are summed over all depths (or even the sigma values at the fits by depth), the CR Lower Bound is, at minimum, an order of magnitude smaller than any of the sigma values from the fits. There are a few reasons why we do not reach this lower resolution limit: the photoelectron-range, the size of the charge cloud, and Compton scatters.

Both the photoelectron -range and the size of the charge cloud depend on the energy of the gamma-ray and of the imparted energy to the photoelectron in the interaction [37, 111]. In Hayward and Wehe, 2008 [111], simulated GEANT results showed that cloud size increased nearly linearly with gamma-ray energy (on average); thus if we assume based on these simulation results that at $\approx$155 keV the cloud size would roughly be $\approx 28\,\mu$m, then the CR Lower Bound is much smaller. Thus, it is possible for our system to be ”photoelectron-range limited” [37].

Compton scatters could also be a limiting factor in obtaining the CR Lower Bound. Since the CR Lower Bound is a function of the MDRF’s, Compton scatters would likely cause the MDRF’s to vary. This would result in more errors for the MLE as the ML tends to be biased to larger values (even if variations in the MDRF’s are small). While we typically exclude Compton events based on the number of strips involved in an interaction, we could still have Compton scatters that are mistaken for single strip interactions. In Figure 2.11, even when the beam is positioned under a strip we were still able to obtain multi-strip events. Because the beam was at the center of a strip and not at the edge, we know that these events are not charge-shared.

While the sigma values from the Gaussian fits are too large compared to the CR Lower Bound values, the behavior of the spatial response with depth is similar. For the DC-Coupled side (which predicts the x-position, and are the vertical front strips), spatial resolution is poor at depth 5 (see Figures 3.5 and 3.2. Likewise, the CR Lower Bound for depth 5 on the DC-Coupled side is larger than the other depths. This also occurs on the AC-Coupled side for depths 8 and 9 (which corresponds to the y-positioning).

Sample Mean Results: Figure 3.15 shows the calculated sample means from the estimated event distributions for the position-ratio and MLE 2-D methods. This data is difficult to represent near the gap, as both methods will contain sub-pixel values that pertain to the next strip and those affect the sample mean. For example, in the x-projection, moving from the edge of strip 7 (70 with the 10 sub-pixels) onto strip 8 (80) means that the sub-pixel estimations of 7 - 9 would pertain to strip 7 while those from 1 - 2 would pertain to strip 8. However, we did not account for these sub-pixels to belong to either strip in the estimation, thus the sample mean for positions close to the gap is lowered (or raised) when containing these sub-pixels that actually belong to the other strip. To try to account for this, we assigned these sub-pixels to each strip, i.e. 7-9 belong to strip 7, 1-2 belong to strip 8 which results in Figure 3.15. The curvature of the points over the gap area are a result of forcing this hard cut-off with the strip assignment instead of verifying what the strip assignment was for that particular event. Future work should keep track of strip assignments for each MLE of each event to obtain a better representation of the sample mean near the gap.

Despite the curvature near the gap, it is interesting to note that the sample mean of both methods are similar, even though the individual spots discussed earlier in this chapter seemed promising for the MLE 2-D results for fixing the distortion. However, since the distribution of events on either side of the strip contain a mix of events from both strips, allowing for those in the sample mean (via the recommendation above) would represent the behavior better and to verify if there is a difference between the two methods at the strip edge.

Spot Tests with Other Digital Pixels: Using the same MDRF's, inverse covariance, and determinant for the analyzed digital pixel (bottom right digital pixel of the 2x2 strip area), we looked at spots near the centers of the other three digital pixels. In clockwise order from the bottom right digital pixel: bottom left, upper left, and upper right digital pixels. The resulting MLE 2-D image is shown with the position-ratio image and their Gaussian fits in Figures 3.17 - 3.19. Table 3.4 lists the spatial resolution for all four beam locations.

Table 3.4: Spatial Resolutions of Each Digital Pixel. Spatial resolution (mm) of a beam location near the center of each digital pixel. Each result in shown in the earlier sections (see figure numbers in table).

Method	Lower Right Pixel (Figure 3.9)	Lower Left Pixel (Figure 3.17)
Position-ratio	X: 2.25 +/- 0.96 Y: 1.40 +/- 0.59	X: 2.26 +/- 0.96 Y: 1.36 +/- 0.58
MLE 2-D	X: 1.66 +/- 0.70 Y: 1.36 +/- 0.58	X: 1.42 +/- 0.60 Y: 0.97 +/- 0.41

Method	Upper Left Pixel (Figure 3.18)	Upper Right Pixel (Figure 3.19)
Position-ratio	X: 2.14 +/- 0.91 Y: 1.68 +/- 0.71	X: 2.14 +/- 0.63 Y: 1.62 +/- 0.69
MLE 2-D	X: 1.47 +/- 0.62 Y:2.33 +/- 0.99	X: 1.49 +/- 0.63 Y: 2.33 +/- 0.99

Starting with the lower right pixel, the spatial resolutions for the position-ratio method are similar when moving in the horizontal direction (left to right for example) but differ when moving vertically, especially in the resolution for the Y-projection. MLE 2-D shows this trend for the upper digital pixels but not for the lower ones. Additionally, when moving horizontally, MLE 2-D has better spatial resolution along the Y-projection compared to the position-ratio method; however when moving vertically it is the X-projection that has the better spatial resolution. Thus, both methods indicate that our detector is more sensitive in the Y-direction. Overall, a MLE based on MDRFs from a calibration from one location in the detector does not perform well due to this.

Implications: Astro-imaging and SPECT: Referring back to the COSI instrument mentioned in Chapter 1 which also had DSS HPGe detectors, our average spatial resolution is comparable in the x-direction and better in the y-direction. Event positioning on COSI is simply just the x- and y-strip that the event occurred in or near to (there are 37 strips with 2 mm strip pitch, the gap size is the same as ours, 0.25 mm) a strip. Using MLE however, could allow for a DSS HPGe detector with wider strips giving the instrument more detection area (depending on the shape of the crystal) and less output electronics.

Currently the electronics on COSI do not allow for waveform digitization as is done in our electronics [124], however, pulse-height might be possible and sub-strip positioning may be done by using the fast signals as a type of threshold discriminator. In this case, either the position-ratio or the MLE method that we investigated could be used for the position estimation. More research would be needed on what information is lost when (1) a waveform is digitized and reduced to a single value as in our case and (2) how does that differ when only a pulse height of the waveform is used.

In nuclear imaging and small-animal applications, spatial resolution of an imaging system ideally should be the sub-mm range [55]. SmartPET, a system for PET imaging using DSS HPGe detectors has around 1 mm [125]. With both position methods currently, neither give sub-mm resolution. As stated above, some of the reasons for not achieving our ideal resolution (which would be the CR Lower Bound) are the Compton Scatters, photoelectron-range limited, and the size of the charge cloud. In using the MLE method in the way that we did (using the squared integrated fast signal values), our limitations are due to not being able to properly fit the response at the edge of the strip and at different depths. With a response that changes with both position and depth, a more complex fit is required that can appropriately fit the tails of the responses as the beam moves near and away from the gap. Lastly, not using the full waveform in itself is a limitation, this is discussed more in the next section.

3.4.1 Future Work

The purpose of this study was to see if the MLE method would remove the effect from the position-ratio method of preferentially placing counts at the edge and also seeing if better spatial resolution could be obtained. While the MLE 2-D results showed some promise in that area, both with better spatial resolution and in the result of the beam at the corner of the pixel (with the centroid being less shifted to the edge of the pixel compared to the position-ratio method; the sample mean did not show a difference between either method.

While the depth fits were poor, it would be of interest to see if performing a MLE by depth, and then subsequently adding the depths for a 2D image result is still more beneficial than just perfoming an MLE on 2D event information (collapse the depth information first and then do the estimation).

With the level of information obtained from using the fast and slow signal values, we are still limited in the fact that we can not differentiate between charge-shared events and Compton scatters. However, more information could be obtained from waveform data, which was also collected at APS in a similar raster pattern. The waveforms could then be investigated as a function of position. For example, if there was some sort of difference in the waveforms at a beam position in the center of a strip vs. the waveforms in the center of the gap then it may be possible to differentiate a charge-shared event from a Compton scatter. Additionally, the information that might be obtained from how the waveforms differ when approaching and leaving a strip edge would improve the positioning done with just the 2-strip events. This study would require modeling of signal generation in the detector, waveform analysis, and a more complicated MLE, one that would include a method of classifying different waveforms for different events.

3.5 Conclusion

In this work, we aimed to improve the our imaging system by attempting to remove the image distortions seem in our previous prototype. We did this by collecting calibration data that would allow us to define the response of our detector as a function of position and depth using a well collimated x-ray beam source at APS. This data was then used to develop a likelihood model that would then be used to perform the position estimation at each event. The model used was a multivariate Gaussian and estimation was performed using both a 1-D and a 2-D variation, with the estimation applied at each depth.

What we found was that a MLE 2-D estimation shows (when looking at individual beam locations) the most promise as far as improved spatial resolution, and also seemingly a tendency to not preferentially place positions at the edge. Quantitatively, however, a sample mean calculation done on data collected from strip center to strip center showed little difference between the position-ratio method and the MLE method; with the behavior near the gap being difficult to quantify for both methods. Further work should be done to verify that the MLE methods are indeed as biased as the original position estimation method, one way that this could be improved is by incorporating which strip the event triggered into the sample mean. Also, using a Gaussian mean and sigma value may not be appropriate for the shape of these resulting pdfs. Another way to improve the MLE method is to use the full waveform instead of the single value of the fast-signals obtained from the digitization. This, along with modeling the signal generation of the detector would provide a more accurate estimation of the spatial response.

Lastly, the calculated CR Lower Bound values where shown to be much smaller than the sigma values obtained with any of the position methods. Various explanations were discussed as to why our detector system does not reach this lower bound including being photoelectron-range limited and incorrectly identified Compton scatters.

BIBLIOGRAPHY

[1] Gary W. Phillips. Gamma-ray imaging with Compton cameras, 5 1995. ISSN 0168583X. URL http://www.sciencedirect.com/science/article/pii/0168583X95800859.

[2] Lawrence Berkeley National Laboratory. Radioactivity, 2000. URL http://www2.lbl.gov/abc/wallchart/chapters/03/0.html.

[3] D. J. Thompson. Highlights of GeV gamma-ray astronomy. *Astrophysics and Space Sciences Transactions*, 6(1):59–64, 12 2010. ISSN 1810-6536. doi: 10.5194/astra-6-59-2010. URL http://www.astrophys-space-sci-trans.net/6/59/2010/astra-6-59-2010.html.

[4] Perry Sprawls. *The Physical Principles of Medical Imaging: Interaction of Radiation with Matter*. Aspen Publishers, 2 edition, 1993. ISBN 0-944838-54-5. URL http://www.sprawls.org/ppmi2/INTERACT/#CHAPTERCONTENTS.

[5] Glenn F Knoll. *Radiation Detection and Measurement*. John Wiley & Sons, Inc., Hoboken, 4th edition, 2010. ISBN 978-0-470-13148-0.

[6] M.J. Berger, J.H. Hubbell, S.M. Seltzer, J. Chang, J.S. Coursey, R. Sukumar, D.S. Zucker, K. Olsen, J. Change, J.S. Coursey, R. Sukumar, D.S. Zucker, and K. Olsen. XCOM: Photon Cross Sections Database — NIST, 1998. URL https://www.nist.gov/pml/xcom-photon-cross-sections-database.

[7] BEER and A. Bestimmung der Absorption des rothen Lichts in farbigen Flussigkeiten. *Ann. Physik*, 162:78–88, 1852. URL https://ci.nii.ac.jp/naid/10027937899/.

[8] Heinz G Pfeiffer. THE ORIGINS OF BEER'S LAW. Technical report.

[9] W W Moses, S A Payne, W S Choong, G Hull, and B W Reutter. Scintillator non-proportionality: Present understanding and future challenges. *Ieee Transactions on Nuclear Science*, 55(3):1049–1053, 2008. doi: 10.1109/tns.2008.922802.

[10] Simon R. Cherry, James A. Sorenson, and Michael E. Phelps. *Physics in Nuclear Medicine*. Elsevier Saunders, Philadelphia, fourth edition, 2012. ISBN 978-1-4160-5198-5.

[11] Matthew George. Main Page/PHYS 4210/Gamma Ray Spectroscopy - Physics Wiki, 2018. URL http://physwiki.apps01.yorku.ca/index.php?title=Main_Page/PHYS_4210/Gamma_Ray_Spectroscopy.

[12] Mark. Fox. *Optical Properties of Solids*. Oxford University Press, Oxford, 2 edition, 2010.

[13] Todd E Peterson and Lars R Furenlid. SPECT detectors: the Anger Camera and beyond. *Physics in medicine and biology*, 56(17):R145–R182, 2011. ISSN 0031-9155. doi: 10.1088/0031-9155/56/17/R01.

[14] Lindsay Johnson. *Development of a SmallAnimal SPECT System with a HighPurity Germanium Detector*. PhD thesis, Vanderbilt University, 2013.

[15] H.H. Barrett. Detectors for Small-Animal SPECT II: Statistical Limitations and Estimation Methods. In H.H. Barrett and M.A. Kupinski, editors, *Small-Animal SPECT Imaging*, chapter 3, pages 49–85. Springer Science+Business Media, Inc., New York, 2005. ISBN 978-0387-25143-1.

[16] H.C. Boston, A.J. Boston, R.J. Cooper, J. Cresswell, A.N. Grint, A.R. Mather, P.J. Nolan, D.P. Scraggs, G. Turk, C.J. Hall, I. Lazarus, A. Berry, T. Beveridge, J. Gillam, and R. Lewis. Characterisation of the SmartPET planar Germanium detectors. *Nuclear Instruments and Methods in Physics Research Section A: Accelerators, Spectrometers, Detectors and Associated Equipment*, 579(1):104–107, 8 2007. ISSN

01689002. doi: 10.1016/j.nima.2007.04.017. URL http://www.sciencedirect.com/science/article/pii/S0168900207005864.

[17] M.D. Wilson, L. Dummott, D.D. Duarte, F.H. Green, S. Pani, A. Schneider, J.W. Scuffham, P. Seller, and M.C. Veale. A 10 cm 10 cm CdTe Spectroscopic Imaging Detector based on the HEXITEC ASIC. *Journal of Instrumentation*, 10(10):P10011, 2015. ISSN 1748-0221. doi: 10.1088/1748-0221/10/10/P10011. URL http://stacks.iop.org/1748-0221/10/i=10/a=P10011?key=crossref.06f25f7540dd5b48941a3e0bf6fd1f5d.

[18] D.J. Wagenaar, J. Zhang, T. Kazules, T. Vandehei, E. Bolle, S. Chowdhury, K. Parnham, and B.E. Patt. In Vivo Dual-Isotope SPECT Imaging with Improved Energy Resolution. *2006 IEEE Nuclear Science Symposium Conference Record*, 6: 3821–3826, 2006. ISSN 1082-3654. doi: 10.1109/NSSMIC.2006.353824. URL http://ieeexplore.ieee.org/document/4179866/.

[19] Todd E Peterson and Sepideh Shokouhi. Advances in preclinical SPECT instrumentation. *Journal of nuclear medicine : official publication, Society of Nuclear Medicine*, 53(6):841–4, 6 2012. ISSN 1535-5667. doi: 10.2967/jnumed.111.099853. URL http://www.pubmedcentral.nih.gov/articlerender.fcgi?artid=3422073&tool=pmcentrez&rendertype=abstract.

[20] Andrew M Polemi, Justin Niestroy, Alexander Stolin, Gangadhar Jaliparthi, Randy Wojcik, Stan Majewski, and Mark B Williams. Design and characterization of a low profile NaI(Tl) gamma camera for dedicated molecular breast tomosynthesis. *Proceedings of SPIE–the International Society for Optical Engineering*, 9969, 8 2016. ISSN 0277-786X. doi: 10.1117/12.2246561. URL http://www.ncbi.nlm.nih.gov/pubmed/28835730.

[21] N. Giokaris, G. Loudos, D. Maintas, A. Karabarbounis, M. Lembesi, V. Spanoudaki,

E. Stiliaris, S. Boukis, N. Sakellios, N. Karakatsanis, A. Gektin, A. Boyarintsev, V. Pedash, and V. Gayshan. Comparison of CsI(Tl) and CsI(Na) partially slotted crystals for high-resolution SPECT imaging. *Nuclear Instruments and Methods in Physics Research, Section A: Accelerators, Spectrometers, Detectors and Associated Equipment*, 569(2 SPEC. ISS.):185–187, 12 2006. ISSN 01689002. doi: 10.1016/j.nima.2006.08.014. URL https://www.sciencedirect.com/science/article/pii/S0168900206014276.

[22] Edgar V. van Loef and Kanai S. Shah. Advances in scintillators for medical imaging applications. In H. Bradford Barber, Lars R. Furenlid, and Hans N. Roehrig, editors, *Medical Applications of Radiation Detectors IV*, volume 9214, page 92140A. International Society for Optics and Photonics, 9 2014. ISBN 9781628412413. doi: 10.1117/12.2065795. URL http://proceedings.spiedigitallibrary.org/proceeding.aspx?doi=10.1117/12.2065795.

[23] The Royal, Marsden Nhs, Foundation Trust, and Surrey Sm. Investigation of LaBr 3 :Ce and LaCl 3 :Ce scintillators for SPECT imaging. In *2008 5th IEEE International Symposium on Biomedical Imaging: From Nano to Macro*, pages 1243–1246. IEEE, 5 2008. ISBN 9781424420032. doi: 10.1109/ISBI.2008.4541228. URL http://ieeexplore.ieee.org/document/4541228/.

[24] Ivanovic M Weber D. Ultra high resolution imaging of small animals: Implications for preclinical and research studies. *J Nuclear Cardiol*, 6(3):332– 44., 5 1999. ISSN 10713581. doi: 10.1016/S1071-3581(99)90046-6. URL http://link.springer.com/10.1016/S1071-3581(99)90046-6.

[25] W. Shockley. Currents to Conductors Induced by a Moving Point Charge. *Journal of Applied Physics*, 9(10):635, 4 1938. ISSN 00218979. doi: 10.1063/1.1710367. URL http://scitation.aip.org/content/aip/journal/jap/9/10/10.1063/1.1710367.

[26] Zhong He. Review of the ShockleyRamo theorem and its application in semiconductor gamma-ray detectors. *Nuclear Instruments and Methods in Physics Research Section A: Accelerators, Spectrometers, Detectors and Associated Equipment*, 463 (1-2):250–267, 5 2001. ISSN 01689002. doi: 10.1016/S0168-9002(01)00223-6. URL http://www.sciencedirect.com/science/article/pii/S0168900201002236.

[27] Todd E Peterson, Sepideh Shokouhi, Lars R Furenlid, and Donald W Wilson. Multi-pinhole SPECT imaging with silicon strip detectors. *IEEE Transactions on Nuclear Science*, 56(3):646–652, 6 2009. ISSN 00189499. doi: 10.1109/TNS.2009.2012514. URL http://www.ncbi.nlm.nih.gov/pubmed/20953300http://www.pubmedcentral.nih.gov/articlerender.fcgi?artid=PMC2953820.

[28] DOUGLAS J. DJ Wagenaar. CdTe and CdZnTe semiconductor detectors for nuclear medicine imaging. *Emission Tomography, The Fundamentals of PET and . . .*, pages 269–291, 2004. doi: 10.1016/B978-012744482-6.50018-1. URL http://linkinghub.elsevier.com/retrieve/pii/B9780127444826500181http://scholar.google.com/scholar?hl=en&btnG=Search&q=intitle:CdTe+and+CdZnTe+semiconductor+detectors+for+nuclear+medicine+imaging#7.

[29] Jerome J Griesmer, Barry Kline, Joe Grosholz, Kevin Parnham, and Daniel Gagnon. Performance Evaluation of a New CZT Detector for Nuclear Medicine: SOLSTICE. In *2001 IEEE Nuclear Science Symposium Conference Record (Cat. No.01CH37310)*, San Diego, 2001. IEEE-INST ELECTRICAL ELECTRONICS ENGINEERS INC, 345 E 47TH ST, NEW YORK, NY 10017-2394. URL https://ieeexplore.ieee.org/document/1009733/.

[30] C Scheiber. CdTe and CdZnTe detectors in nuclear medicine. *Nuclear Instruments and Methods in Physics Research Section A: Accelerators, Spectrometers, Detectors and Associated Equipment*, 448(3):513–524, 7 2000. ISSN 01689002. doi:

10.1016/S0168-9002(00)00282-5. URL http://linkinghub.elsevier.com/retrieve/pii/S0168900200002825.

[31] Katsutoshi Tsuchiya, Isao Takahashi, Tsuneaki Kawaguchi, Kazuma Yokoi, Yuuichi Morimoto, Takafumi Ishitsu, Atsurou Suzuki, Yuuichirou Ueno, and Keiji Kobashi. Basic performance and stability of a CdTe solid-state detector panel. *Annals of Nuclear Medicine*, 24(4):301–311, 5 2010. ISSN 09147187. doi: 10.1007/s12149-010-0354-1. URL http://link.springer.com/10.1007/s12149-010-0354-1.

[32] Lindsay C Johnson, Desmond L Campbell, Ethan L Hull, and Todd E Peterson. Characterization of a high-purity germanium detector for small-animal SPECT. *Physics in Medicine and Biology*, 56(18):5877–5888, 2011. doi: 10.1088/0031-9155/56/18/007.

[33] Lindsay C. Johnson, Oleg S. Ovchinnikov, Sepideh Shokouhi, and Todd E. Peterson. Characterization of a small-animal high-purity germanium SPECT system. *IEEE Nuclear Science Symposium Conference Record*, 37232:2185–2190, 2012. ISSN 10957863. doi: 10.1109/NSSMIC.2012.6551498. URL http://ieeexplore.ieee.org/document/6551498/.

[34] G Bizarri, W W Moses, J Singh, A N Vasil'ev, and R T Williams. An analytical model of nonproportional scintillator light yield in terms of recombination rates. *Journal of Applied Physics*, 105(4), 2009. doi: 04450710.1063/1.3081651.

[35] Zhong He, Glenn F Knoll, David K Wehe, Ronald Rojeski, Carlos H Mastrangelo, Mark Hammig, Carla Barrett, and Akira Uritani. 1-D position sensitive single carrier semiconductor detectors. *Nuclear Instruments and Methods in Physics Research, Section A: Accelerators, Spectrometers, Detectors and Associated Equipment*, 380 (1-2):228–231, 10 1996. ISSN 01689002. doi: 10.1016/S0168-9002(96)00352-X. URL https://www.sciencedirect.com/science/article/pii/S016890029600352X.

[36] Z He, G. F. Knoll, D. K. Wehe, and J Miyamoto. Position-sensitive single carrier CdZnTe detectors. *Nuclear Instruments and Methods in Physics Research, Section A: Accelerators, Spectrometers, Detectors and Associated Equipment*, 388(1-2):180–185, 3 1997. ISSN 01689002. doi: 10.1016/S0168-9002(97)00318-5. URL https://www.sciencedirect.com/science/article/pii/S0168900297003185.

[37] Esen Salcin, Harrison H. Barrett, H. Bradford Barber, Shinrichiro Takeda, Shin Watanabe, Tadayuki Takahashi, and Lars R. Furenlid. Fisher information analysis of depth-of-interaction estimation in double-sided strip detectors. *IEEE Transactions on Nuclear Science*, 61(3):1243–1251, 6 2014. ISSN 0018-9499. doi: 10.1109/TNS.2014.2317454. URL http://ieeexplore.ieee.org/document/6819048/http://apps.webofknowledge.com.proxy.library.vanderbilt.edu/full_record.do?product=UA&search_mode=GeneralSearch&qid=3&SID=3C6Q6HEsuGZI85dIdJZ&page=1&doc=1.

[38] Jrgen Knödlseder. The future of gamma-ray astronomy. *Comptes Rendus Physique*, 17(6):663–678, 6 2016. ISSN 1631-0705. doi: 10.1016/J.CRHY.2016.04.008. URL https://www.sciencedirect.com/science/article/pii/S1631070516300287.

[39] Orvosi Kepalkotas. Position sensitive and energy selective gamma ray detection. In Bela Kari, Kinga Karlinge, David Legrady, Berczi Viktor, and Szaboles Czifrus, editors, *Medical Imaging*, chapter 3.3, pages 1–2. Budapest, 2017. URL http://oftankonyv.reak.bme.hu/tiki-index.php?page=Position+sensitive+and+energy+selective+gamma+ray+detection&structure=Book+for+Physicists.

[40] Javier Rico. Gamma-ray Astronomy: Implications for Fundamental Physics. In *XXXI Physics in Collision*, page 8, Vancouver, 11 2011. URL http://arxiv.org/abs/1111.6393.

[41] David Paneque. Experimental Gamma-Ray Astronomy. *Journal of Physics: Con-*

ference Series, 375(5):052020, 7 2012. ISSN 1742-6596. doi: 10.1088/1742-6596/375/1/052020. URL http://iopscience.iop.org/1742-6596/375/5/052020.

[42] Ryley Hill, Kiyoshi W. Masui, and Douglas Scott. The Spectrum of the Universe. *Applied Spectroscopy*, 72(5):663–688, 5 2018. ISSN 0003-7028. doi: 10.1177/0003702818767133. URL http://journals.sagepub.com/doi/10.1177/0003702818767133.

[43] Nasa Goddard Spaceflight Center) Gehrels, Neil (Astrophysics Science Division, Peter (Department of Astronomy Meszaros, and Pennsylvania State University) Astrophysics. Gamma Ray Bursts. *Science (New York, N.Y.)*, 337(932):16, 2012. ISSN ¡null¿.

[44] S. Abdollahi, M. Ackermann, M. Ajello, A. Albert, L. Baldini, J. Ballet, G. Barbiellini, D. Bastieri, J. Becerra Gonzalez, R. Bellazzini, E. Bissaldi, R. D. Blandford, E. D. Bloom, R. Bonino, E. Bottacini, J. Bregeon, P. Bruel, R. Buehler, S. Buson, R. A. Cameron, M. Caragiulo, P. A. Caraveo, E. Cavazzuti, C. Cecchi, A. Chekhtman, C. C. Cheung, G. Chiaro, S. Ciprini, J. Conrad, D. Costantin, F. Costanza, S. Cutini, F. D'Ammando, F. de Palma, A. Desai, R. Desiante, S. W. Digel, N. Di Lalla, M. Di Mauro, L. Di Venere, B. Donaggio, P. S. Drell, C. Favuzzi, S. J. Fegan, E. C. Ferrara, W. B. Focke, A. Franckowiak, Y. Fukazawa, S. Funk, P. Fusco, F. Gargano, D. Gasparrini, N. Giglietto, M. Giomi, F. Giordano, M. Giroletti, T. Glanzman, D. Green, I. A. Grenier, J. E. Grove, L. Guillemot, S. Guiriec, E. Hays, D. Horan, T. Jogler, G. Jóhannesson, A. S. Johnson, D. Kocevski, M. Kuss, G. La Mura, S. Larsson, L. Latronico, J. Li, F. Longo, F. Loparco, M. N. Lovellette, P. Lubrano, J. D. Magill, S. Maldera, A. Manfreda, M. Mayer, M. N. Mazziotta, P. F. Michelson, W. Mitthumsiri, T. Mizuno, M. E. Monzani, A. Morselli, I. V. Moskalenko, M. Negro, E. Nuss, T. Ohsugi, N. Omodei, M. Orienti, E. Orlando, V. S. Paliya, D. Paneque, J. S. Perkins, M. Persic, M. Pesce-Rollins, V. Petrosian,

F. Piron, T. A. Porter, G. Principe, S. Rainò, R. Rando, M. Razzano, S. Razzaque, A. Reimer, O. Reimer, C. Sgrò, D. Simone, E. J. Siskind, F. Spada, G. Spandre, P. Spinelli, L. Stawarz, D. J. Suson, M. Takahashi, K. Tanaka, J. B. Thayer, D. J. Thompson, D. F. Torres, E. Torresi, G. Tosti, E. Troja, G. Vianello, and K. S. Wood. The second catalog of flaring gamma-ray sources from the Fermi All-sky Variability Analysis. *The Astrophysical Journal*, 846(1):34, 8 2016. ISSN 1538-4357. doi: 10.3847/1538-4357/aa8092. URL http://arxiv.org/abs/1612.03165%0Ahttp://dx.doi.org/10.3847/1538-4357/aa8092.

[45] NASA/DOE/Fermi LAT Collaboration. GMS: NASA's Fermi Mission Sharpens its High-energy View, 2013. URL https://svs.gsfc.nasa.gov/12019.

[46] R Diehl. Gamma-Rays from Nucleosynthesis Ejecta. *Journal of Physics: Conference Series*, 665(1):012011, 1 2016. ISSN 1742-6588. doi: 10.1088/1742-6596/665/1/012011. URL http://stacks.iop.org/1742-6596/665/i=1/a=012011?key=crossref.c5ff7c614b876e9228fed0007fb9675a.

[47] Roland Diehl. Cosmic Gamma-Ray Spectroscopy. *Astronomical Reciew*, 8(4):4–52, 7 2013. URL http://arxiv.org/abs/1307.4198.

[48] R Bühler and R Blandford. The surprising Crab pulsar and its nebula: a review. *Reports on Progress in Physics*, 77(6):066901, 6 2014. ISSN 0034-4885. doi: 10.1088/0034-4885/77/6/066901. URL http://stacks.iop.org/0034-4885/77/i=6/a=066901?key=crossref.fb64a7f462c4e2c6ee8f23d7cf130f89.

[49] Bryan M. Gaensler and Patrick O. Slane. The Evolution and Structure of Pulsar Wind Nebulae. *Annual Review of Astronomy and Astrophysics*, 44(1):17–47, 9 2006. ISSN 0066-4146. doi: 10.1146/annurev.astro.44.051905.092528. URL http://www.annualreviews.org/doi/10.1146/annurev.astro.44.051905.092528.

[50] D. Bernard. Polarimetry of cosmic gamma-ray sources above e+e pair creation

threshold. *Nuclear Instruments and Methods in Physics Research Section A: Accelerators, Spectrometers, Detectors and Associated Equipment*, 729:765–780, 11 2013. ISSN 0168-9002. doi: 10.1016/J.NIMA.2013.07.047. URL https://www.sciencedirect.com/science/article/pii/S0168900213010565.

[51] Cosmin Ilie. Gamma Ray polarimetry; a new window for the non-thermal Universe. Technical report, 2019. URL https://arxiv.org/pdf/1906.02824.pdf.

[52] Andre A. M. Muñoz, Anna Vella, Matthew J. F. Healy, David W. Lane, Ian Jupp, and David Lockley. Rapid prototyping-coded masks for x-ray backscatter imaging. *Optical Engineering*, 57(08):1, 8 2018. ISSN 0091-3286. doi: 10.1117/1.OE.57.8.085104. URL https://www.spiedigitallibrary.org/journals/optical-engineering/volume-57/issue-08/085104/Rapid-prototyping-coded-masks-for-x-ray-backscatter-imaging/10.1117/1.OE.57.8.085104.full.

[53] E. Jourdain, J. P. Roques, M. Chauvin, and D. J. Clark. Separation of two contributions to the high energy emission of Cygnus X-1: Polarization measurements with integral SPI. *Astrophysical Journal*, 761(1):27, 12 2012. ISSN 15384357. doi: 10.1088/0004-637X/761/1/27. URL http://stacks.iop.org/0004-637X/761/i=1/a=27?key=crossref.434faec1efc55fc21ec7d821e49e16ed.

[54] Benjamin L Franc, Paul D Acton, Carina Mari, and Bruce H Hasegawa. Small-animal SPECT and SPECT/CT: important tools for preclinical investigation. *Journal of nuclear medicine : official publication, Society of Nuclear Medicine*, 49(10): 1651–63, 10 2008. ISSN 0161-5505. doi: 10.2967/jnumed.108.055442. URL http://jnm.snmjournals.org/content/49/10/1651.abstract.

[55] Steven R Meikle, Peter Kench, Michael Kassiou, and Richard B Banati. Small animal SPECT and its place in the matrix of molecular imaging technologies. *Physics*

in medicine and biology, 50(22):R45–R61, 11 2005. ISSN 0031-9155. doi: 10.1088/0031-9155/50/22/R01. URL http://www.ncbi.nlm.nih.gov/pubmed/16264248.

[56] H.H. Barrett and William C J Hunter. Detectors for Small-Animal SPECT I: Overview of Technologies. In H.H. Barrett and M.A. Kupinski, editors, *Small-Animal SPECT Imaging*, chapter 2, pages 9–43. Springer Science+Business Media, Inc., New York, 2005. ISBN 978-0387-25143-1.

[57] Hal O. Anger. Scintillation camera. *Review of Scientific Instruments*, 29(1):27–33, 1 1958. ISSN 00346748. doi: 10.1063/1.1715998. URL http://aip.scitation.org/doi/10.1063/1.1715998.

[58] A Gearhart, T Peterson, and L Johnson. SU-C-201-02: Quantitative Small-Animal SPECT Without Scatter Correction Using High-Purity Germanium Detectors. *Medical physics*, 42(6):3202, 6 2015. ISSN 0094-2405. doi: 10.1118/1.4923840. URL http://scitation.aip.org/content/aapm/journal/medphys/42/6/10.1118/1.4923840.

[59] Simon Ramo. Currents Induced by Electron Motion. *Proceedings of the IRE*, 27(9):584–585, 9 1939. ISSN 00968390. doi: 10.1109/JRPROC.1939.228757. URL http://ieeexplore.ieee.org/document/1686997/https://lartpc-docdb.fnal.gov/0005/000532/001/ramo_pire_27_584_39.pdf.

[60] J. D. Eskin, H. H. Barrett, and H. B. Barber. Signals induced in semiconductor gamma-ray imaging detectors. *Journal of Applied Physics*, 85(2):647, 1 1999. ISSN 00218979. doi: 10.1063/1.369198. URL http://link.aip.org/link/JAPIAU/v85/i2/p647/s1&Agg=doihttp://scitation.aip.org.proxy.library.vanderbilt.edu/content/aip/journal/jap/85/2/10.1063/1.369198.

[61] Marios E. Myronakis and Dimitra G. Darambara. Monte Carlo investigation of charge-transport effects on energy resolution and detection efficiency of pixelated CZT detectors for SPECT/PET applications. *Medical Physics*, 38(1):455–467, 12

2011. ISSN 00942405. doi: 10.1118/1.3532825. URL http://doi.wiley.com/10.1118/1.3532825.

[62] T.H. Prettyman. Theoretical framework for mapping pulse shapes in semiconductor radiation detectors. *Nuclear Instruments and Methods in Physics Research Section A: Accelerators, Spectrometers, Detectors and Associated Equipment*, 428(1):72–80, 6 1999. ISSN 0168-9002. doi: 10.1016/S0168-9002(98)01582-4. URL https://www.sciencedirect.com/science/article/pii/S0168900298015824.

[63] P.N. Luke. Unipolar charge sensing with coplanar electrodes-application to semiconductor detectors. *IEEE Transactions on Nuclear Science*, 42(4):207–213, 1995. ISSN 00189499. doi: 10.1109/23.467848. URL http://ieeexplore.ieee.org/document/467848/.

[64] D.S. McGregor and R.A. Rojeski. High-resolution ionization detector and array of such detectors, 5 1998. URL https://patents.google.com/patent/US6175120B1/en.

[65] A.E. E. Bolotnikov, G.S. S. Camarda, Y. Cui, G. De Geronimo, J. Fried, R. Gul, A. Hossain, K. Kim, G. Yang, E. Vernon, and R.B. B. James. Rejecting incomplete charge-collection events in CdZnTe and other semiconductor detectors. *Nuclear Instruments and Methods in Physics Research Section A: Accelerators, Spectrometers, Detectors and Associated Equipment*, 664(1):317–323, 2 2012. ISSN 01689002. doi: 10.1016/j.nima.2011.10.066. URL http://www.sciencedirect.com/science/article/pii/S0168900211020328http://dx.doi.org/10.1016/j.nima.2011.10.066.

[66] G. Montémont, M. Arques, L. Verger, and J. Rustique. A capacitive Frisch grid structure for CdZnTe detectors. *IEEE Transactions on Nuclear Science*, 48(3 I):278–281, 2001. ISSN 00189499. doi: 10.1109/23.940065.

[67] J. K. Polack, M. Hirt, J. Sturgess, N. D. Sferrazza, A. E. Bolotnikov, S. Babalola, G. S. Camarda, Y. Cui, S. U. Egarievwe, P. M. Fochuk, R. Gul, A. Hossain,

K. Kim, O. V. Kopach, L. Marchini, G. Yang, L. Xu, and R. B. James. Variation of electric shielding on virtual Frisch-grid detectors. *Nuclear Instruments and Methods in Physics Research, Section A: Accelerators, Spectrometers, Detectors and Associated Equipment*, 621(1-3):424–430, 9 2010. ISSN 01689002. doi: 10.1016/j.nima.2010.05.035. URL https://www.sciencedirect.com/science/article/pii/S0168900210011368.

[68] Benjamin W Sturm, Zhong He, Edgar A. Rhodes, Thomas H Zurbuchen, and Patrick L Koehn. Coplanar grid CdZnTe detectors for space science applications. In *Hard X-Ray and Gamma-Ray Detector Physics VI*, volume 5540, page 14, 2004. ISBN 7347631157. doi: 10.1117/12.564260. URL https://cztlab.engin.umich.edu/wp-content/uploads/sites/187/2015/03/Coplanar-grid-CdZnTe-detectors-for-space-science-applications_B.W.Sturm_SPIE2004.pdf.

[69] H. Barrett, J. Eskin, and H. Barber. Charge Transport in Arrays of Semiconductor Gamma-Ray Detectors. *Physical Review Letters*, 75(1):156–159, 7 1995. ISSN 0031-9007. doi: 10.1103/PhysRevLett.75.156. URL http://link.aps.org/doi/10.1103/PhysRevLett.75.156.

[70] Jae Cheon Kim, William R. Kaye, and Zhong He. Signal modeling of charge sharing effect in simple pixelated CdZnTe detector. *Journal of the Korean Physical Society*, 64(9):1336–1345, 5 2014. ISSN 0374-4884. doi: 10.3938/jkps.64.1336. URL http://apps.webofknowledge.com.proxy.library.vanderbilt.edu/full_record.do?product=WOS&search_mode=GeneralSearch&qid=2&SID=3BMWTIdru3cxnwbOCmB&page=1&doc=2&cacheurlFromRightClick=no.

[71] J Hayward and D Wehe. Observation of charge-sharing in an HPGe double-sided strip detector. *Nuclear Instruments & Methods in Physics Research Section a-*

Accelerators Spectrometers Detectors and Associated Equipment, 579(1):99–103, 2007. doi: 10.1016/j.nima.2007.04.130.

[72] G.K. Skinner. Imaging with coded-aperture masks. *Nuclear Instruments and Methods in Physics Research*, 221:33–40, 1984.

[73] Paul M.E. Shutler, Alireza Talebitaher, and Stuart V. Springham. Signal-to-noise ratio in coded aperture imaging. *Nuclear Instruments and Methods in Physics Research Section A: Accelerators, Spectrometers, Detectors and Associated Equipment*, 669:22–31, 2012. ISSN 01689002. doi: 10.1016/j.nima.2011.12.023.

[74] R.J. Proctor, G.K. Skinner, and A.P. Willmore. The design of optimum coded mask for X-ray telescopes. *Mon. Not. R. astr. Soc.*, 187:633–643, 1979. URL https://docs.google.com/viewer?url=http%3A%2F%2Fmnras.oxfordjournals.org%2Fcontent%2F187%2F3%2F633.full.pdf.

[75] Harrison H Barrett. FRESNEL ZONE PLATE IMAGING IN NUCLEAR MEDICINE, 1972. URL http://jnm.snmjournals.org/content/13/6/382.full.pdf.

[76] R H Dicke. Scatter-Hole Cameras for X-Rays and Gamma Rays. *The Astrophysical Journal*, 153:L101, 1968. ISSN 0004-637X. doi: 10.1086/180230. URL http://articles.adsabs.harvard.edu/cgi-bin/nph-iarticle_query?1968ApJ...153L.101D&data_type=PDF_HIGH&whole_paper=YES&type=PRINTER&filetype=.pdf.

[77] M H Finger and T A Prince. Hexagonal uniformly redundant arrays for coded-aperture imaging. In *International Cosmic Ray Conference*, volume 3, pages 295–298, 1985. URL https://ntrs.nasa.gov/search.jsp?R=19850026627http://adsabs.harvard.edu/full/1985ICRC....3..295F.

[78] Zhiping Mu and Yi-Hwa Liu. Aperture collimation correction and maximum-likelihood image reconstruction for near-field coded aperture imaging of single pho-

ton emission computerized tomography. *IEEE Transactions on Medical Imaging*, 25(6):701–711, 6 2006. ISSN 0278-0062. doi: 10.1109/TMI.2006.873298. URL http://ieeexplore.ieee.org/document/1637528/.

[79] Roberto Accorsi, Francesca Gasparini, and Richard C. Lanza. Optimal coded aperture patterns for improved SNR in nuclear medicine imaging. *Nuclear Instruments and Methods in Physics Research Section A: Accelerators, Spectrometers, Detectors and Associated Equipment*, 474(3):273–284, 12 2001. ISSN 01689002. doi: 10.1016/S0168-9002(01)01326-2. URL http://linkinghub.elsevier.com/retrieve/pii/S0168900201013262.

[80] Karen Van Audenhaege, Roel Van Holen, Stefaan Vandenberghe, Christian Vanhove, Scott D. Metzler, and Stephen C. Moore. Review of SPECT collimator selection, optimization, and fabrication for clinical and preclinical imaging. *Medical Physics*, 42(8):4796–4813, 7 2015. ISSN 00942405. doi: 10.1118/1.4927061. URL http://doi.wiley.com/10.1118/1.4927061.

[81] Desmond L Campbell. *A High-Purity Germanium Imaging System for Limited-Angle Nuclear Breast Tomography*. PhD thesis, Vanderbilt University, 2015.

[82] G T Gullberg, G L Zeng, F L Datz, P E Christian, C H Tung, and H T Morgan. Review of convergent beam tomography in single photon emission computed tomography. *Physics in Medicine and Biology*, 37(3):507–534, 3 1992. ISSN 0031-9155. doi: 10.1088/0031-9155/37/3/002. URL http://stacks.iop.org/0031-9155/37/i=3/a=002?key=crossref.670632425e65e0fa490c4510e770eed9.

[83] Stephan Walrand, Franois Jamar, Marion de Jong, and Stanislas Pauwels. Evaluation of novel whole-body high-resolution rodent SPECT (Linoview) based on direct acquisition of linogram projections. *Journal of nuclear medicine : official publi-*

cation, Society of Nuclear Medicine, 46(11):1872–80, 11 2005. ISSN 0161-5505. URL http://www.ncbi.nlm.nih.gov/pubmed/16269602.

[84] V. Schönfelder, A. Hirner, and K. Schneider. A telescope for soft gamma ray astronomy. *Nuclear Instruments and Methods*, 107(2):385–394, 3 1973. ISSN 0029-554X. doi: 10.1016/0029-554X(73)90257-7. URL https://www.sciencedirect.com/science/article/pii/0029554X73902577.

[85] R. W. TODD, J. M. NIGHTINGALE, and D. B. EVERETT. A proposed γ camera. *Nature*, 251(5471):132–134, 9 1974. ISSN 0028-0836. doi: 10.1038/251132a0. URL http://www.nature.com/articles/251132a0.

[86] S Moon, B Q Arnés, A J Boston, H C Boston, J R Cresswell, T Davinson, A Gadea, L J Harkness, D S Judson, I Lazarus, P J Nolan, R D Page, A H Prieto, and J Simpson. Compton imaging with AGATA and SmartPET for DESPEC. *Journal of Instrumentation*, 6(12):C12048–C12048, 12 2011. ISSN 1748-0221. doi: 10.1088/1748-0221/6/12/C12048. URL http://stacks.iop.org/1748-0221/6/i=12/a=C12048.

[87] Kouichi Hagino, Hirokazu Odaka, Goro Sato, Shin Watanabe, Motohide Kokubun, Taro Fukuyama, Shinya Saito, Tamotsu Sato, Yuto Ichinohe, Tadayuki Takahashi, Toshio Nakano, Kazuhiro Nakazawa, Kazuo Makishima, Shin'ichiro Takeda, Motohide Kokubun, Taro Fukuyama, Shinya Saito, Tamotsu Sato, Yuto Ichinohe, Tadayuki Takahashi, Toshio Nakano, Kazuhiro Nakazawa, Kazuo Makishima, Hiroyasu Tajima, Takaaki Tanaka, Kazunori Ishibashi, Takuya Miyazawa, Michito Sakai, Karin Sakanobe, Hiroyoshi Kato, Shunya Takizawa, and Kentaro Uesugi. Imaging and spectral performance of CdTe double-sided strip detectors for the hard x-ray imager onboard ASTRO-H. In Tadayuki Takahashi, Stephen S. Murray, and Jan-Willem A. den Herder, editors, *SPIE Astronomical Telescopes + Instrumentation*, volume 8443, pages 1–11. International Society for Optics and Pho-

tonics, 9 2012. ISBN 9780819491442. doi: 10.1117/12.926052. URL http://proceedings.spiedigitallibrary.org/proceeding.aspx?articleid=1361138.

[88] B. F. Phlips, S. E. Inderhees, R. A. Kroeger, W. N. Johnson, R. L. Kinzer, J. D. Kurfess, B. L. Graham, and N. Gehrels. Performance of a compton telescope using Position-sensitive germanium detectors. *IEEE Transactions on Nuclear Science*, 43 (3 PART 2):1472–1475, 1996. ISSN 00189499. doi: 10.1109/23.507086.

[89] Paolo Rossi, Giuseppe Baldazzi, Andrea Battistella, Michele Bello, Dante Bollini, Valter Bonvicini, Cristiano Lino Fontana, Gisella Gennaro, Giuliano Moschini, Francesco Navarria, Alexander Rashevsky, Nikolay Uzunov, Gianluigi Zampa, Nicola Zampa, Andrea Vacchi, Floyd D. McDaniel, and Barney L. Doyle. X-Rays Compton Detectors For Biomedical Application. In *APPLICATION OF ACCELERATORS IN RESEARCH AND INDUSTRY: TwentyFirst International Conference*, volume 1336, pages 356–360. AIP Publishing, 6 2011. doi: 10.1063/1.3586119. URL http://scitation.aip.org/content/aip/proceeding/aipcp/10.1063/1.3586119.

[90] M. Kolstein and M. Chmeissani. Using triple gamma coincidences with a pixelated semiconductor Compton-PET scanner: a simulation study. *Journal of Instrumentation*, 11(01):C01039–C01039, 2016. ISSN 1748-0221. doi: 10.1088/1748-0221/11/01/C01039. URL http://stacks.iop.org/1748-0221/11/i=01/a=C01039?key=crossref.8e9c9db58dfb21f9805bfea8bf107702.

[91] J.B. B. Martin, N. Dogan, J.E. E. Gormley, G.F. F. Knoll, M. O'Donnell, and D.K. K. Wehe. Imaging multi-energy gamma-ray fields with a Compton scatter camera. *IEEE Transactions on Nuclear Science*, 41(4 pt 1):1019–1025, 1994. ISSN 00189499. doi: 10.1109/23.322851. URL http://ieeexplore.ieee.org/lpdocs/epic03/wrapper.htm?arnumber=322851.

[92] Lucian Mihailescu, Kai Vetter, and Daniel Chivers. Standoff 3D gamma-ray imag-

ing. *IEEE Transactions on Nuclear Science*, 56(2):479–486, 4 2009. ISSN 00189499. doi: 10.1109/TNS.2009.2015304. URL http://ieeexplore.ieee.org/document/4812296/.

[93] Manbir Singh and David Doria. Single Photon Imaging with Electronic Collimation. *IEEE Transactions on Nuclear Science*, 32(1):843–847, 1985. ISSN 0018-9499. doi: 10.1109/TNS.1985.4336953. URL http://ieeexplore.ieee.org/document/4336953/.

[94] Gary W Phillips, David J Nagel, and Timothy Coffey. A Primer on the Detection of Nuclear and Radiological Weapons. Technical Report July, National Defense University Center for Technology and National Security Policy, 2005.

[95] Pat Zanzonico. An Overview of Nuclear Imaging. In *Radiopharmaceutical Chemistry*, pages 101–117. Springer International Publishing, Cham, 2019. doi: 10.1007/978-3-319-98947-1{_}6. URL http://link.springer.com/10.1007/978-3-319-98947-1_6.

[96] M. M. Rogulski, H. B. Barber, H. H. Barrett, R. L. Shoemaker, and J. M. Woolfenden. Ultra-high-resolution brain spect imaging: Simulation results. *IEEE Transactions on Nuclear Science*, 40(4):1123–1129, 8 1993. ISSN 15581578. doi: 10.1109/23.256722. URL https://ieeexplore.ieee.org/document/256722/.

[97] D.W. Wilson. Computational Algorithms in Small-Animal Imaging. In H. H. Barrett and Matthew A Kupinski, editors, *Small-Animal SPECT Imaging*, chapter 3, pages 139–162. Springer Science+Business Media, Inc., New York, 2005. ISBN 978-0387-25143-1.

[98] Johann Radon. On the determination of functions from their integral values along certain manifolds. *IEEE Transactions on Medical Imaging*, 5(4):170–176, 12 1986. ISSN 0278-0062. doi: 10.1109/TMI.1986.4307775. URL http://ieeexplore.ieee.org/document/4307775/.

[99] A. M. Cormack. Representation of a Function by Its Line Integrals, with Some Radiological Applications. *Journal of Applied Physics*, 34(9):2722–2727, 9 1963. ISSN 0021-8979. doi: 10.1063/1.1729798. URL http://aip.scitation.org/doi/10.1063/1.1729798.

[100] RN Bracewell. Strip Integration in Radio Astronomy. *Australian Journal of Physics*, 9(2):198, 2011. ISSN 0004-9506. doi: 10.1071/ph560198. URL http://www.publish.csiro.au/PH/pdf/PH560198.

[101] Richard Gordon, Robert Bender, and Gabor T. Herman. Algebraic Reconstruction Techniques (ART) for three-dimensional electron microscopy and X-ray photography. *Journal of Theoretical Biology*, 29(3):471–481, 12 1970. ISSN 10958541. doi: 10.1016/0022-5193(70)90109-8. URL https://www.sciencedirect.com/science/article/pii/0022519370901098.

[102] H. Hurwitz. Entropy reduction in Bayesian analysis of measurements. *Physical Review A*, 12(2):698–706, 8 1975. ISSN 0556-2791. doi: 10.1103/PhysRevA.12.698. URL https://link.aps.org/doi/10.1103/PhysRevA.12.698.

[103] Emanuel Levitan and Gabor T. Herman. A Maximum A Posteriori Probability Expectation Maximization Algorithm for Image Reconstruction in Emission Tomography. *IEEE Transactions on Medical Imaging*, 6(3):185–192, 9 1987. ISSN 1558254X. doi: 10.1109/TMI.1987.4307826. URL http://ieeexplore.ieee.org/document/4307826/.

[104] S.J. Wilderman, N.H. Clinthorne, J.A. Fessler, and W.L. Rogers. List-mode maximum likelihood reconstruction of Compton scatter camera images in nuclear medicine. In *1998 IEEE Nuclear Science Symposium Conference Record. 1998 IEEE Nuclear Science Symposium and Medical Imaging Conference (Cat. No.98CH36255)*, volume 3, pages 1716–1720. IEEE, 2002. ISBN 0-7803-5021-

9. doi: 10.1109/nssmic.1998.773871. URL http://ieeexplore.ieee.org/document/773871/.

[105] A P Dempster, N M Laird, and D B Rubin. Maximum Likelihood from Incomplete Data Via the EM Algorithm. *Journal of the Royal Statistical Society: Series B (Methodological)*, 39(1):1–22, 1977. doi: 10.1111/j.2517-6161.1977.tb01600.x. URL https://www.jstor.org/stable/pdf/2984875.pdf?refreqid=excelsior%3A33e18036aa4fe9fec41a3dfb0fdd2cc6.

[106] H. Malcolm Hudson and Richard S. Larkin. Accelerated Image Reconstruction Using Ordered Subsets of Projection Data. *IEEE Transactions on Medical Imaging*, 13(4):601–609, 1994. ISSN 1558254X. doi: 10.1109/42.363108. URL http://ieeexplore.ieee.org/document/363108/.

[107] Brian F. Hutton, H. Malcolm Hudson, and Freek J. Beekman. A clinical perspective of accelerated statistical reconstruction. *European Journal of Nuclear Medicine*, 24 (7):797–808, 7 1997. ISSN 0340-6997. doi: 10.1007/BF00879671. URL http://link.springer.com/10.1007/BF00879671.

[108] Desmond L. Campbell and Todd E. Peterson. Simulation study comparing high-purity germanium and cadmium zinc telluride detectors for breast imaging. *Phys Med Biol*, 49(22):7059–7079, 2014. ISSN 15378276. doi: 10.1038/jid.2014.371.

[109] PHDs Co. PHDs: Gamma Ray Imaging Detectors, 2015. URL http://www.phdsco.com/.

[110] J P Hayward and D K Wehe. Charge Loss Correction in a High-Purity Germanium Double-Sided Strip Detector. *Ieee Transactions on Nuclear Science*, 55(5):2789–2797, 2008. doi: 10.1109/tns.2008.2003130. URL http://ieeexplore.ieee.org/document/4696599/.

[111] J Hayward and D Wehe. Incomplete charge collection in an HPGe double-sided strip detector. *Nuclear Instruments & Methods in Physics Research Section a-Accelerators Spectrometers Detectors and Associated Equipment*, 586(2):215–223, 2008. doi: http://www.sciencedirect.com/science/article/pii/S0168900207024655.

[112] K Vetter, M Burks, and L Mihailescu. Gamma-ray imaging with position-sensitive HPGe detectors. *Nuclear Instruments and Methods in Physics Research Section A: Accelerators, Spectrometers, Detectors and Associated Equipment*, 525(1Äì2):322–327, 2004. doi: http://dx.doi.org/10.1016/j.nima.2004.03.087. URL http://www.sciencedirect.com/science/article/pii/S0168900204004553.

[113] Desmond Campbell, Ieee Student Member, Lindsay Johnson, and Andrew Gearhart. A Dual-head Germanium SPECT System. In *IEEE Nuclear Science Symposuim & Medical Imaging Conference*, pages 2–3. IEEE-INST ELECTRICAL ELECTRONICS ENGINEERS INC, 345 E 47TH ST, NEW YORK, NY 10017-2394, 2008.

[114] Harrison H. Barrett, William C J Hunter, Brian William Miller, Stephen K. Moore, Yichun Chen, and Lars R. Furenlid. Maximum-likelihood methods for processing signals from gamma-ray detectors. *IEEE Transactions on Nuclear Science*, 56(3): 725–735, 2009. ISSN 00189499. doi: 10.1109/TNS.2009.2015308.

[115] Argonne National Laboratory and U.S. Department of Energy. Overview — Advanced Photon Source, 2018. URL https://www.aps.anl.gov/About/Overview.

[116] Argonne National Laboratory and U.S. Department of Energy. APS Systems Map — Advanced Photon Source, 2018. URL https://www.aps.anl.gov/About/Overview/APS-Systems-Map.

[117] Doctor O F Philosophy and Esen Salcin. FISHER INFORMATION IN X-RAY / GAMMA-RAY IMAGING In the Graduate College. 2015.

[118] U.S. Department of Energy Office, Argonne National Laboratory, and U.S. Department of Energy. Beamlines Information — Advanced Photon Source, 2018. URL https://www.aps.anl.gov/Beamlines/Directory/Details?beamline_id=104.

[119] Movocat Thompson. Installation Manual for, . URL http://www.thomsonlinear.com/downloads/actuators/DMx_Lifting_Column_Installation_mnuk.pdf.

[120] La10 Thompson. Installation manual for LA1, . URL http://www.thomsonlinear.com/downloads/actuators/Electrak_LA_FA_IA_Installation_mnuk.pdf.

[121] Imac. IMAC Motion Control, 2019. URL http://www.imac-mcc.com/.

[122] APS. EPICS About, 1993. URL http://www.aps.anl.gov/epics/about.php.

[123] Inc. The MathWorks. 2-D Gaussian filtering of images - MATLAB imgaussfilt. URL https://www.mathworks.com/help/images/ref/imgaussfilt.html.

[124] A. Lowell, S. Boggs, J. L. Chiu, C. Kierans, S. McBride, C. H. Tseng, A. Zoglauer, M. Amman, H. K. Chang, P. Jean, C. H. Lin, C. Sleator, J. Tomsick, P. von Ballmoos, and C. Y. Yang. Positional calibrations of the germanium double sided strip detectors for the Compton spectrometer and imager. In Andrew D. Holland and James Beletic, editors, *Proceedings of SPIE*, volume 9915, page 99152H. International Society for Optics and Photonics, 8 2016. doi: 10.1117/12.2233145. URL http://proceedings.spiedigitallibrary.org/proceeding.aspx?doi=10.1117/12.2233145.

[125] R.J. Cooper, A.J. Boston, H.C. Boston, J.R. Cresswell, A.N. Grint, L.J. Harkness, P.J. Nolan, D.C. Oxley, D.P. Scraggs, A.R. Mather, I. Lazarus, and J. Simpson. Positron Emission Tomography imaging with the SmartPET system. *Nuclear Instruments and Methods in Physics Research Section A: Accelerators, Spectrometers, Detectors and Associated Equipment*, 606(3):523–532, 7 2009. ISSN 0168-9002. doi: 10.1016/J.NIMA.2009.04.015. URL https://www.sciencedirect.com/science/article/pii/S0168900209007943.